

**HIDDEN HIGGSES AND DARK MATTER AT  
CURRENT AND FUTURE COLLIDERS**

by

Adarsh Pyarelal

---

Copyright © Adarsh Pyarelal 2017



A Dissertation Submitted to the Faculty of the  
DEPARTMENT OF PHYSICS  
In Partial Fulfillment of the Requirements  
For the Degree of  
DOCTOR OF PHILOSOPHY  
In the Graduate College  
University of Arizona

2017



THE UNIVERSITY OF ARIZONA  
GRADUATE COLLEGE

As members of the Dissertation Committee, we certify that we have read the dissertation prepared by Adarsh Pyarelal entitled *Hidden Higgses and Dark Matter at Current and Future Colliders*, and recommend that it be accepted as fulfilling the dissertation requirement for the Degree of Doctor of Philosophy.

---

Shufang Su

Date: 12 April, 2017

---

William D. Toussaint

Date: 12 April, 2017

---

Kenneth A. Johns

Date: 12 April, 2017

---

Sean P. Fleming

Date: 12 April, 2017

---

Weigang Wang

Date: 12 April, 2017

Final approval and acceptance of this dissertation is contingent upon the candidate's submission of the final copies of the dissertation to the Graduate College.

I hereby certify that I have read this dissertation prepared under my direction and recommend that it be accepted as fulfilling the dissertation requirement.

---

Dissertation Director: Shufang Su

Date: 12 April, 2017



**STATEMENT BY AUTHOR**

---

This dissertation has been submitted in partial fulfillment of the requirements for an advanced degree at the University of Arizona and is deposited in the University Library to be made available to borrowers under rules of the Library.

Brief quotations from this dissertation are allowable without special permission, provided that an accurate acknowledgement of the source is made. Requests for permission for extended quotation from or reproduction of this manuscript in whole or in part may be granted by the head of the major department or the Dean of the Graduate College when in his or her judgment the proposed use of the material is in the interests of scholarship. In all other instances, however, permission must be obtained from the author.

---

SIGNED: Adarsh Pyarelal



## ACKNOWLEDGMENTS

---

I would like to thank my advisor, Shufang Su, for her patient guidance and support throughout my graduate studies. Under her mentorship, I learned to critically examine scientific claims and to hold my own research to the highest standards. I would also like to thank the following:

- Ken Johns, for letting me get a taste of experimental particle physics, career advice, and a fun semester teaching Scientific Computing.
- Doug Toussaint, Sean Fleming, and Weigang Wang for being on my committee.
- Abhay Shastry, Dheeraj Golla, and Rebekah Cross for their steady friendship these past six years.
- Jessie Erikson, for being the most wonderful partner anyone could ask for.

Finally, I would like to thank my family, and especially my parents for their unconditional love and encouragement during this process. It is a huge privilege to be able to pursue a doctorate, and I could not have done it without their support.



## ABSTRACT

---

Despite its indisputable successes, the Standard Model of particle physics (SM) is widely considered to be an effective low-energy approximation to an underlying theory that describes physics at higher energy scales. While there are many candidates for such a theory, nearly all of them predict the existence of additional particles beyond those of the Standard Model. In this work, we present three analyses aimed at discovering new particles at current and future particle colliders.

The first two analyses are designed to probe extended scalar sectors, which often arise in theories beyond the Standard Model (BSM). The structure of these extended scalar sectors can be described by a physically well-motivated class of models, known collectively as Two-Higgs Doublet Models (2HDMs). The scalar mass spectrum of 2HDMs is comprised of two CP-even states  $h$  and  $H$ , a CP-odd state  $A$ , and a pair of charged states  $H^\pm$ . Traditional searches for these states at particle colliders focus on finding them via their decays to SM particles. However, there are compelling scenarios in which these heavy scalars decay through exotic modes to non-SM final states. In certain regions of parameter space, these exotic modes can even dominate the conventional decay modes to SM final states, and thus provide a complementary avenue for discovering new Higgs bosons.

The first analysis presented aims to discover charged Higgs bosons  $H^\pm$  via top decay at the LHC. We find that the exotic decay modes outperform the conventional decay modes for regions of parameter space with low values of the 2HDM parameter  $\tan\beta$ .

The second analysis aims to systematically cover all the exotic decay scenarios that are consistent with theoretical and experimental constraints, at both the 14 TeV LHC and a future 100 TeV hadron collider. We find that the preliminary results are promising - we are able to exclude a large swathe of 2HDM parameter space, up to scalar masses of 3.5 TeV, for a wide range of values of  $\tan\beta$ , at a 100 TeV collider.

In addition to these two analyses, we also present a third, aimed at discovering pair produced higgsinos that decay to binos at a 100 TeV collider. Higgsinos and binos are new fermion states that arise in the Minimal Supersymmetric Standard Model (MSSM). This heavily-studied model is the minimal phenomenologically viable incorporation of supersymmetry - a symmetry that connects fermions and bosons - into the Standard Model. In the scenario we consider, the bino is the lightest supersymmetric partner, which makes it a good candidate for dark matter. Using razor variables and boosted decision trees, we are able to exclude higgsinos up to 1.8 TeV for binos up to 1.3 TeV.

## CONTENTS

---

ABSTRACT	<b>9</b>
LIST OF FIGURES	<b>11</b>
LIST OF TABLES	<b>13</b>
LIST OF ACRONYMS	<b>15</b>
<b>1 INTRODUCTION</b>	<b>17</b>
1.1 Setting the stage . . . . .	17
1.2 Structure of the dissertation . . . . .	18
<b>2 THE STANDARD MODEL AND BEYOND</b>	<b>21</b>
2.1 The Standard Model . . . . .	21
2.2 Two-Higgs Doublet Models . . . . .	26
2.3 The Minimal Supersymmetric Standard Model . . . . .	30
<b>3 COLLIDER PHENOMENOLOGY AND MACHINE LEARNING</b>	<b>37</b>
3.1 Detector design for hadron colliders . . . . .	37
3.2 Anatomy of a collider analysis . . . . .	39
3.3 Statistical significance in particle physics . . . . .	41
3.4 Machine learning in particle physics . . . . .	43
<b>4 LIGHT CHARGED HIGGSES AT THE LHC</b>	<b>47</b>
4.1 Couplings and branching ratios . . . . .	48
4.2 Literature review . . . . .	50
4.3 Collider analysis . . . . .	51
4.4 Implications for a Type II 2HDM . . . . .	56
4.5 Conclusion . . . . .	59
<b>5 EXOTIC HIGGS DECAYS AT 14 AND 100 TEV</b>	<b>61</b>
5.1 Exotic Higgs decays: The Big Picture . . . . .	61
5.2 Classifying exotic decays . . . . .	62
5.3 Literature review . . . . .	63
5.4 Crafting features for our classifier . . . . .	64
5.5 Preliminary results . . . . .	66
5.6 Conclusions and outlook . . . . .	66
<b>6 A RAZOR SEARCH FOR DARK MATTER AT 100 TEV</b>	<b>69</b>
6.1 Introduction . . . . .	69
6.2 Model and experimental constraints . . . . .	71
6.3 Analysis Details . . . . .	75
6.4 Conclusion . . . . .	80
<b>7 CONCLUSION</b>	<b>83</b>
<b>BIBLIOGRAPHY</b>	<b>85</b>

## LIST OF FIGURES

---

1.1	Schematic diagram of the Large Hadron Collider, which lies on the border between Switzerland and France. (CERN) . . . . .	17
2.1	A representation of the innards of a proton, showing the dynamic structure. Source: [11] . . . . .	25
2.2	Feynman diagram for the one-loop fermionic correction to the SM Higgs mass . . . . .	31
2.3	Feynman diagram for the one-loop scalar correction to the SM Higgs mass . . . . .	31
2.4	2-loop RG evolution of inverse gauge couplings in the SM (dashed lines) and the MSSM (solid lines). Source: [10]. . . . .	31
3.1	Transverse slice of the CMS detector, showing the paths of various particles. Source: [19] . . . . .	39
3.2	Illustration of a non-linear decision boundary in two-dimensional feature space. . . . .	44
4.1	Contours of the branching ratio of the top quark to the charged Higgs, in the $m_{H^\pm} - t_\beta$ plane. . . . .	48
4.2	Contours of the branching ratio for the decay ( $H^\pm \rightarrow AW$ ) in the Type II 2HDM in $m_{H^\pm} - t_\beta$ plane. . . . .	49
4.3	The branching ratios of $H^\pm \rightarrow AW$ (red), $\tau\nu$ (green) and $cs$ (blue) as functions of $t_\beta$ for $m_{H^\pm} = 160$ GeV. . . . .	49
4.4	Weakened CMS limits on the branching ratio of the top quark to the charged Higgs. . . . .	50
4.5	Weakening of the CMS exclusion limits in the $m_{H^\pm} - t_\beta$ . . . . .	50
4.6	Normalized distributions of $\cos \theta^*$ (top) and the transverse momentum of the $tj$ system $p_T(tj)$ (bottom), for case A with $m_{H^\pm} = 160$ GeV. . . . .	53
4.7	Exclusion and discovery limits on $\sigma \times \text{BR}(t \rightarrow H^+ b)$ . . . . .	55
4.8	Contours of branching ratios for the benchmark point BP1. . . . .	57
4.9	Contours of branching ratios $\text{BR}(H^\pm \rightarrow hW^\pm)$ for the benchmark point BP2. . . . .	57
4.10	The exclusion (yellow and cyan regions combined, bounded by dashed lines) and discovery (cyan region only bound by solid lines) reach achievable in the $t_\beta$ versus $s_{\beta-\alpha}$ plane for the benchmark points 1 and 2, with an integrated luminosity of $300 \text{ fb}^{-1}$ at the 14 TeV LHC. . . . .	58

4.11	Exclusion (yellow regions bounded by solid lines as well as the cyan regions) and discovery (cyan regions bounded by the dashed lines) imposed by the $tj$ -channel (blue) and $tt$ -channel (red) in the $m_{H^\pm} - t_\beta$ parameter space for 300 $\text{fb}^{-1}$ luminosity with $m_A = 70 \text{ GeV}$ . The same limits apply for $m_h = 70 \text{ GeV}$ and $s_{\beta-\alpha} = 0$ if $A$ is decoupled. The black hatched region indicates the region excluded by the CMS search based on $H^\pm \rightarrow \tau\nu$ [33]. . . . .	58
5.1	branching ratios for exotic decays in Type II 2HDMs, as a function of $t_\beta$ , with $c_{\beta-\alpha} = 0$ . Source: [4] . . . . .	62
5.2	Feynman diagrams for charged Higgs production in association with a heavy quark.) . . . . .	65
5.3	Exclusion and discovery limits for the channel $A \rightarrow HZ \rightarrow \tau\tau ll$ , for the 14 TeV LHC with 100 $\text{fb}^{-1}$ (solid red line) and 300 $\text{fb}^{-1}$ (dashed red line) and a 100 TeV collider with 1000 $\text{fb}^{-1}$ (solid blue line) and 3000 $\text{fb}^{-1}$ (dashed blue line). . . . .	66
5.4	Exclusion and discovery limits for the channel $H \rightarrow AZ \rightarrow \tau\tau ll$ for the 14 TeV LHC with 100 $\text{fb}^{-1}$ (solid red line) and 300 $\text{fb}^{-1}$ (dashed red line) and a 100 TeV collider with 1000 $\text{fb}^{-1}$ (solid blue line) and 3000 $\text{fb}^{-1}$ (dashed blue line). . . . .	67
5.5	Exclusion and discovery reaches in the $m_{H^\pm} - m_H$ plane for the exotic decay $H^\pm \rightarrow HW^\pm$ , at a 100 TeV collider with an integrated luminosity of 3 $\text{ab}^{-1}$ . Here we assume $m_{12}^2 = m_H^2 s_\beta c_\beta$ . . . . .	67
6.1	DM detection, three ways . . . . .	69
6.2	Feynman diagram for bino-stau coannihilation. . . . .	70
6.3	Feynman diagrams for the signal and background processes (Generated using [98].) . . . . .	72
6.4	Higgsino pair production cross section as a function of $\mu$ , for $M_1 = 25 \text{ GeV}$ . . . . .	73
6.5	Higgsino decay branching ratios of $\mu$ , for $M_1 = 25 \text{ GeV}$ . . . . .	73
6.6	Normalized distributions of the razor kinematical variables $M_R$ (top) and $M_T^R$ (bottom) for a 1 TeV higgsino NLSP and 25 GeV bino LSP . . . . .	76
6.7	Distribution of the decision function of the gradient boosted decision tree classifier algorithm for the signal ( $ \mu  = 1 \text{ TeV}$ , $M_1 = 25 \text{ GeV}$ ) and backgrounds. . . . .	78
6.8	Discovery (red) and exclusion (blue) contours for the traditional cut-and-count analysis (solid) and boosted decision tree analysis (dashed), for an integrated luminosity of 3000 $\text{fb}^{-1}$ . . . . .	79

## LIST OF TABLES

---

2.1	The fields of the Standard Model, grouped by their charges under the relevant gauge groups. . . . .	<b>21</b>
2.2	The fermion sector of the Standard Model, grouped by generation. . . . .	<b>22</b>
2.3	Fermion coupling patterns for 2HDMs with flavor conservation. . . . .	<b>28</b>
2.4	The factors $\xi$ that determine the Yukawa couplings of Higgs bosons in Type II 2HDMs. . . . .	<b>30</b>
2.5	Chiral supermultiplets of the MSSM. . . . .	<b>35</b>
2.6	Gauge supermultiplets of the MSSM. . . . .	<b>35</b>
3.1	The two competing hypotheses for our simple number counting example. Source: [27]. . . . .	<b>41</b>
4.1	Representative cut flow table for the benchmark point with $m_{H^\pm} = 160$ GeV and $m_A = 70$ GeV at the 14 TeV LHC. (Single top production) . . . . .	<b>54</b>
4.2	Representative cut flow table for the same benchmark point as table 4.1 and the decay mode $A \rightarrow \tau\tau$ . (Top pair production) . . . . .	<b>55</b>
4.3	Benchmark points used for illustrating the discovery and exclusion limits in the context of the Type II 2HDM. Also shown are the typical favored regions of $s_{\beta-\alpha}$ for each case (see [50]). . . . . .	<b>57</b>
5.1	Summary of all the possible exotic decay modes and dominant final states for non-SM Higgs bosons . . . . .	<b>63</b>
5.2	Summary of benchmark planes for exploring exotic Higgs decays in 2HDMs that survive theoretical and experimental constraints. Source: [4]. . . . .	<b>63</b>
6.1	Comparison of cross-sections for $(\tilde{\chi}_{2,3}^0 \tilde{\chi}_2^\pm)$ and $(\tilde{\chi}_2^0 \tilde{\chi}_3^0)$ , for $ \mu  \approx 1$ TeV, at a 100 TeV $pp$ collider. The pair-production cross sections are taken from [96]. The branching ratio to intermediate dibosons is evaluated in the limit where the Goldstone equivalence theorem applies so that $\text{BR}(\tilde{\chi}_{2,3}^0 \rightarrow \tilde{\chi}_0^1 h) \approx \text{BR}(\tilde{\chi}_{2,3}^0 \rightarrow \tilde{\chi}_0^1 Z) \approx 50\%$ . The branching ratios of $W$ , $Z$ , and $h$ are taken to be the same as the SM ones listed in the PDG review [62]. . . . .	<b>72</b>
6.2	Representative cut flow table for the benchmark point $ \mu  = 1$ TeV, $M_1 = 25$ GeV, for a traditional cut-and-count analysis. All cross sections are given in femtobarns, and the units for the missing energy, invariant mass, and razor variable cuts are GeV. The significance, $S/\sqrt{B}$ , is calculated for an integrated luminosity of $3 \text{ ab}^{-1}$ . . . . .	<b>77</b>

6.3	Representative cut flow table for the same benchmark point and integrated luminosity as in <a href="#">table 6.2</a> , but using a boosted decision tree (BDT) analysis instead. The preselection is equivalent to the trigger and identification cuts listed in <a href="#">table 6.2</a> . As before, all the cross sections are in femtobarns.	<a href="#">78</a>
6.4	Discovery reaches and expected exclusion limits (in TeV) for the parameters ( $ \mu , M_1$ ) for the rectangular cuts and boosted decision tree analyses. . . . .	<a href="#">80</a>

## LIST OF ACRONYMS

---

2HDM	Two-Higgs Doublet Model
ATLAS	A Large Toroidal LHC Apparatus
BDT	Boosted Decision Tree
BR	Branching Ratio
BSM	Beyond the Standard Model
CERN	<i>Conseil Européen pour la Recherche Nucléaire</i> (European Organization for Nuclear Research)
CMS	Compact Muon Solenoid
CP	Charge Parity
FCNC	Flavor Changing Neutral Current
LHC	Large Hadron Collider
LSP	Lightest Supersymmetric Particle
NLSP	Next-to-Lightest Supersymmetric Particle
NMSSM	Next-to-Minimal Supersymmetric Standard Model
ML	Machine Learning
MSSM	Minimal Supersymmetric Standard Model
SUSY	Supersymmetry
SM	Standard Model
QCD	Quantum Chromodynamics
UV	Ultraviolet
VEV	Vacuum Expectation Value



# 1

## INTRODUCTION

---

### 1.1 Setting the stage

The Standard Model (SM) of particle physics, which describes the fundamental constituents of matter and their interactions, represents an unambiguous triumph of the scientific method. Its predictions have been verified to extraordinary precision. Its last missing piece, the Higgs boson, was discovered in 2012 [1, 2], nearly fifty years after it was predicted. This resulted in a Nobel prize for François Englert and Peter Higgs, and in much jubilation among the particle physics community.

However, many questions still remain unanswered or unsatisfactorily answered by the Standard Model. For example, the SM does not explain why neutrinos have masses, and does not contain a viable dark matter candidate. On a more abstract level, the square of the mass of the Higgs boson seems unnaturally finely tuned. This phenomenon is termed the *hierarchy problem*, and we will revisit it in [section 2.3](#). In fact, it is widely believed that the Standard Model is only a low-energy effective approximation to an underlying theory that is valid at higher energy scales.

To answer these questions, we must go beyond the Standard Model with new theories. These new theories often predict new fundamental particles and forces, which we can study using particle colliders, like the Large Hadron Collider (LHC), a schematic of which is shown in [figure 1.1](#).

At these colliders, we accelerate particles to nearly the speed of light and collide them against each other, creating new particles that can be detected by extremely sophisticated detectors. One of the main challenges

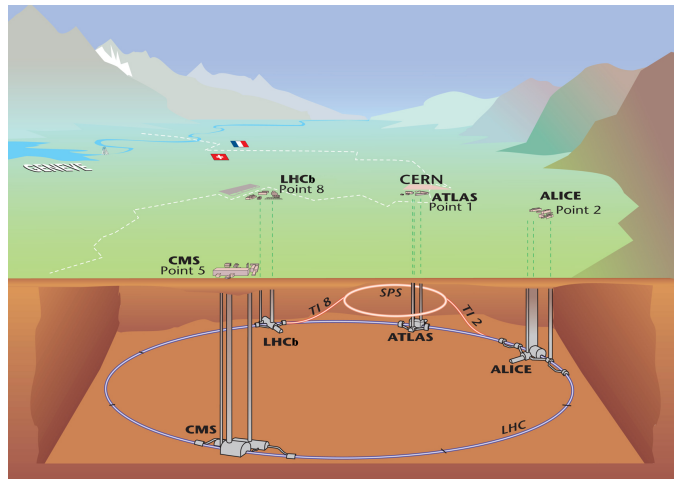


**Figure 1.1:** Schematic diagram of the Large Hadron Collider, which lies on the border between Switzerland and France. ([CERN](#))

at particle colliders is that there are hundreds of millions of collisions every second, but only a small fraction of these will contain signatures of new physics. In addition, there are a multitude of viable theories beyond the Standard Model, each possessing multiple free parameters. However, performing a full experimental analysis for even a single point of the parameter space of a theory can be very time consuming.

For this reason, existing theories must be constrained (or excluded entirely) by holding them up to the light of experimental evidence. Furthermore, we need to have a rough idea of what the most effective collider search strategies are before going ahead with a complete experimental analysis. This is where phenomenology steps in.

Phenomenology bridges the gap between theory and experiment - connecting the predictions of the former with the measurements of the latter. In this dissertation, we present three phenomenological analyses for finding physics beyond the Standard Model at current and future colliders. The rest of the dissertation is structured as follows.

## 1.2 Structure of the dissertation

*Chapter 2.* This chapter briefly reviews the theoretical background behind the collider analyses presented in this dissertation. We go over the particle content and gauge structure of the Standard Model, followed by a discussion of electroweak symmetry breaking. We briefly touch upon CKM mixing, asymptotic freedom, and quantum chromodynamics as well. This is followed by a description of the motivations, mass spectrum, and interactions of Two Higgs Doublet Models (2HDMs) and the Minimal Supersymmetric Standard Model (MSSM).

*Chapter 3.* This chapter describes how to connect theoretical predictions and experimental observables. The design of a generic multipurpose detector for a hadron collider is discussed, followed by discussions of some of the kinematic variables that are relevant to our analyses. The concepts of hypothesis testing and statistical significance are briefly reviewed, and particle physics concerns are recast in the language of machine learning.

*Chapter 4.* In this chapter, we describe a search for a new type of Higgs boson, known as the *charged* Higgs boson ( $H^\pm$ ), that arises naturally in the spectrum of 2HDMs. Finding one of these would be an unmistakable sign of new physics beyond the Standard Model. The mass of this particle,  $m_{H^\pm}$  is a free parameter in the theory. Searches for this particle can be divided into two broad categories - the first involving charged Higgs bosons lighter than the top quark, and the other dealing with charged Higgses heavier than the top quark. We examine the first scenario, with charged Higgses coming from the decay of top quarks that are either produced singly or in pairs.

While experimental results from CMS and ATLAS have placed a lower limit of 160 GeV for the mass of the charged Higgs boson in the

context of the MSSM, these limits have been placed assuming that the charged Higgs decays solely via conventional channels to final states with SM particles. However, theories that predict charged Higgs typically predict other BSM particles as well. These can potentially be lighter than the charged Higgs, thus opening up new, ‘exotic’ decay channels for it. For regions of parameter space with low values of the parameter  $\tan \beta$ , the rate of these exotic decays is much larger than the rate of the conventional decays to SM particles, thus significantly weakening the limits set by the LHC. For a complete picture, we must take into account not only the conventional decay channels, but the exotic ones as well.

In this chapter, we investigate the exotic decay of a charged Higgs to a lighter, neutral Higgs boson - either the pseudoscalar  $A$  or the CP-even scalar  $H$ , and a  $W$  boson. We first perform a *model-independent* analysis. That is, *assuming* that  $H^\pm$  decays exclusively to  $AW^\pm/HW^\pm$ , and that  $A/H$  decays to a pair of tau leptons 8.6% of the time, we set out to find the minimum rate of the signal process required for this analysis to discover it with a significance of  $5\sigma$ , or exclude it with a significance of  $1.96\sigma$ . This rate corresponds to the strength of the signal - the weaker the signal that can be probed by the analysis, the more powerful the analysis is. The model-independent limit on the signal strength can be translated into a limit on the branching ratio of the top quark to the charged Higgs,  $\text{BR}(t \rightarrow H^\pm b)$ . We determined that the single top and the top pair production channels could potentially set exclusion limits of 0.2% and 0.3% respectively on this branching ratio. For the analysis to discover the signal process, the branching ratio would have to be about three times higher than the aforementioned upper limits.

These results can be translated into contours in the  $m_{H^\pm} - \tan \beta$  plane in the parameter space of a Type-II 2HDM that delineate regions that can be either discovered or excluded with this analysis. We also found that this analysis would be able to discover points with the charged Higgs mass  $m_{H^\pm}$  between 155 and 165 GeV for  $\tan \beta > 17$ , and the entire viable mass range for  $\tan \beta < 6$ . We also found that almost the entire relevant region of the  $m_{H^\pm} - \tan \beta$  plane can be excluded with this analysis, with the exception of the regions with very small mass differences between the charged Higgs and the top quark. In summary, we found that the exotic decay channel  $H^\pm \rightarrow AW^\pm/HW^\pm$  probes a region of parameter space complementary to the region probed by conventional decay channels (such as  $H^\pm \rightarrow \tau\nu$ ), and is thus an important search channel to include in the search for charged Higgs bosons. The results in this chapter have been published in [3].

*Chapter 5.* While the project that [chapter 4](#) is based on dealt with the implications of additional, exotic decay channels opening up for charged Higgs bosons arising from extended scalar sectors at the LHC, the project that this chapter is based on is much more ambitious in scope, aiming for nothing less than a complete prospectus of exotic Higgs decay channels in 2HDMs with large mass hierarchies. The authors of [4] have presented

a collection of promising 2HDM benchmark planes for investigation at the LHC that take into account theoretical and experimental constraints and highlight the complementarity between the different search channels. The end goal of this project is to perform detailed collider analyses to determine exclusion and discovery bounds for both the original benchmark planes at the 14 TeV LHC, as well as extended versions of them at a 100 TeV collider that reflect the higher obtainable mass reach. In this chapter, we present preliminary results for two of the benchmark planes, corresponding to the mass hierarchies  $m_H < m_A = m_{H^\pm}$  and  $m_A < m_H = m_{H^\pm}$ . The exotic decay channels considered are  $A \rightarrow HZ$  and  $H^\pm \rightarrow HW^\pm$ . Using boosted decision tree (BDT) classifiers, we are able to exclude charged Higgses with masses up to 2 TeV, for neutral Higgses  $H$  with masses up to 500 GeV, in the benchmark plane IIB suggested in [4] through the decay mode  $H^\pm \rightarrow AW^\pm$  at a 100 TeV collider. In addition, we are able to exclude neutral Higgses ( $A/H$ ) decaying via the channels  $(A/H) \rightarrow (H/A)Z$  for parent masses up to about 3 TeV for a wide range of values of  $\tan\beta$ , keeping the daughter Higgs mass fixed at 200 GeV. This work is being done in collaboration with Felix Kling, Huayang Song, Honglei Li, and Shufang Su.

*Chapter 6.* A 100 TeV proton-proton collider will be an extremely effective way to probe the electroweak sector of the Minimal Supersymmetric Standard Model (MSSM). In this chapter, we describe a search strategy for discovering pair-produced higgsino-like neutralinos ( $\tilde{\chi}_{2,3}^0$ ) that decay to the lightest neutralino ( $\tilde{\chi}_1^0$ ) (which we assume to be an almost pure bino). The lightest neutralino is a strong candidate for particle dark matter. We investigate the particular case in which the higgsinos decay via intermediate  $Z$  and SM Higgs bosons  $h$ , that in turn decay to a pair of leptons and a pair of  $b$ -quarks respectively:

$$pp \rightarrow \tilde{\chi}_2^0 \tilde{\chi}_3^0 \rightarrow (Z \tilde{\chi}_1^0)(h \tilde{\chi}_1^0) \rightarrow llbb + \tilde{\chi}_1^0 \tilde{\chi}_1^0.$$

We performed two analyses simultaneously - the first using rectangular selection cuts on physically motivated kinematic observables known as razor variables, and the second using the same high-level observables, along with a few lower-level observables as input features for a boosted decision tree classifier. The results show that the machine learning technique performs substantially better than the regular rectangular selection cuts. With the machine learning analysis, we can discover higgsinos up to a mass of 1.3 TeV, and exclude them up to a mass of 1.8 TeV. Correspondingly, we can discover binos up to 900 GeV, and exclude them up to 1.3 TeV.

Finally, we conclude in [chapter 7](#), where we provide a summary of our findings and discuss prospects for future work.

# 2

## THE STANDARD MODEL AND BEYOND

---

In this chapter, we will provide some of the theoretical background that our research builds upon. We will first provide a lightning-quick review of the particle content and gauge structure of the Standard Model, followed by an introduction to Two-Higgs Doublet Models and the Minimal Supersymmetric Standard Model. For excellent treatments of the Standard Model, please see [5–8]. For a detailed review of Two-Higgs Doublet Models, see [9], and for a pedagogical introduction to supersymmetry and the MSSM, see [10]. Our discussion is adapted from these works.

### 2.1 The Standard Model

The fundamental constituents of matter are fermions. The interactions between these fermions are mediated by particles known as *gauge bosons*, which arise from the gauge structure of the Standard Model:

$$SU(3) \times SU(2) \times U(1)_Y$$

This means that each fermion transforms in a unique way under transformations corresponding to these gauge groups. In addition to the fermions and gauge bosons, the standard model contains a scalar  $SU(2)$  doublet  $H$ , known as the Higgs field. In [table 2.1](#), we collect the fundamental fields of the SM and their transformation properties under different gauge groups. The labels  $u, d, e$  and  $v$  are collective labels for three generations of fermions, shown in [table 2.2](#). The fields  $g$ ,  $W_\mu$ , and  $B_\mu$  are vector bosons that correspond to the  $SU(3)$ ,  $SU(2)$  and  $U(1)$  gauge group respectively.

The ground state that we inhabit spontaneously breaks the larger symmetry  $SU(2) \times U(1)_Y$  to the symmetry  $U(1)_{\text{EM}}$ . The subscript  $Y$

Type	Field	Spin	$SU(3)$	$SU(2)$	$U(1)_Y$
Scalar	$H$	0	<b>1</b>	<b>2</b>	$\frac{1}{2}$
Fermions	$Q = \begin{pmatrix} u_L \\ d_L \end{pmatrix}$	$\frac{1}{2}$	<b>3</b>	<b>2</b>	$\frac{1}{6}$
	$u_R$		<b>3</b>	<b>1</b>	$\frac{2}{3}$
	$d_R$		<b>3</b>	<b>1</b>	$-\frac{1}{3}$
	$L = \begin{pmatrix} e_L \\ v_L \end{pmatrix}$		<b>1</b>	<b>2</b>	$-\frac{1}{2}$
	$e_R$		<b>1</b>	<b>1</b>	-1
Vector bosons	$g$	1	<b>8</b>	<b>1</b>	0
	$W_\mu$		<b>1</b>	<b>3</b>	0
	$B_\mu$		<b>1</b>	<b>1</b>	0

**Table 2.1:** The fields of the Standard Model, grouped by their charges under the relevant gauge groups.

Generation	Quarks		e: Leptons	v: Neutrinos
	u: Up	d: Down		
I	$u$ : up	$d$ : down	$e$ : electron	$\nu_e$ : electron neutrino
II	$c$ : charm	$s$ : strange	$\mu$ : muon	$\nu_\mu$ : muon neutrino
III	$t$ : top	$b$ : bottom	$\tau$ : tau	$\nu_\tau$ : tau neutrino

Table 2.2: The fermion sector of the Standard Model, grouped by generation.

denotes the hypercharge of the field, while the subscript EM denotes electromagnetism. In this process (which we will revisit in more detail in section 2.1), the three gauge fields  $W_\mu$ , corresponding to the  $SU(2)$  gauge symmetry, combine with the  $B_\mu$  field corresponding to the  $U(1)_Y$  symmetry to form the massive gauge bosons  $W^\pm$  and  $Z$ , and a massless photon,  $A_\mu$  (often denoted by  $\gamma$  instead). The  $W$  and  $Z$  bosons mediate the weak interactions that responsible to phenomena such as radioactive decay, while the photon mediates electromagnetic interactions. The gauge field  $g$  corresponding to the  $SU(3)$  gauge symmetry is known as the *gluon*, and mediates the strong force between nucleons.

### Electroweak symmetry breaking

In 1957, Schwinger proposed the unification of the weak and electromagnetic interactions, citing their vectorial nature. In 1961, Glashow proposed a model for weak interactions governed by symmetry under the product group  $SU(2) \times U(1)$ . The trouble was, experiments had shown that the weak interactions had a short range, implying that the vector bosons that mediated them must be massive. On the other hand, gauge symmetry prohibits mass terms for these intermediate vector bosons. Glashow's theory included these mass terms, but they were put in by hand, and spoiled the renormalizability of the theory. A possible way out was to break the gauge symmetry *spontaneously* rather than explicitly. Spontaneous symmetry breaking refers to the phenomenon where the ground state of a system does not respect the symmetry of the full Lagrangian. However, Goldstone's theorem states that for every spontaneously broken symmetry, there exists a set of massless spin-0 bosons corresponding to the generators of the symmetry group - since such particles have never been observed, this was obviously an undesirable feature of the theory.

Thus we seem to have to choose between two undesirable outcomes: a set of massless gauge bosons, or a set of massless scalars, both of which are inconsistent with what we actually see in nature. Remarkably, each of these problems would turn out to be the solution for the other, through the marvelous *Higgs mechanism*. This mechanism was first put forth by Philip W. Anderson in the context of condensed matter systems. In 1964, three groups – Peter Higgs, the duo of Francois Englert and Robert Brout, and the trio of Gerald Guralnik, C. R. Hagen, and Tom Kibble –

independently and almost simultaneously proposed that this mechanism could explain how the the weak interaction mediators can acquire mass. There is likely a strong case for naming the mechanism after all of these physicists, but for the sake of expediency, we will simply refer to it as the Higgs mechanism.

The Higgs mechanism describes the spontaneous breaking of electroweak symmetry, that is, the breakdown of the product group  $SU(2) \times U(1)_Y \rightarrow U(1)_{EM}$ . This is achieved by adding to the theory a complex scalar  $SU(2)$  doublet, the Higgs field  $H$ :

$$H = \begin{pmatrix} H^+ \\ H^0 \end{pmatrix}.$$

The terms of the Lagrangian that involve this field can be written as follows:

$$\mathcal{L}_{\text{Higgs}} = \frac{1}{2} |D_\mu H|^2 - V(H) \quad (2.1)$$

$$\text{where } V(H) = \left( H^\dagger H - \frac{v^2}{2} \right)^2 \quad (2.2)$$

The gauge covariant derivative for the Standard Model takes the form (neglecting the term corresponding to the unbroken  $SU(3)$  symmetry)

$$D_\mu = \partial_\mu + ig W_\mu^a T^a + ig' Y B_\mu,$$

where  $W_\mu^a$  and  $B_\mu$  are the gauge fields corresponding to the  $SU(2)$  and  $U(1)_Y$  symmetries respectively,  $g$  and  $g'$  are coupling constants, and  $T^a$  and  $Y$  are the generators of the  $SU(2)$  and  $U(1)$  groups. The potential  $V(H)$  reaches its minimum when  $H^\dagger H = v^2/2$ . We pick a non-zero vacuum expectation value (VEV) for  $H$  that breaks the neutral sector symmetry (corresponding to  $H^0$ ) but not the charged symmetry (corresponding to  $H^+$ ), since we wish to keep photons massless. This VEV is given by:

$$H = \begin{pmatrix} 0 \\ \frac{v}{\sqrt{2}} \end{pmatrix}.$$

Plugging this into the kinetic term of the Lagrangian, and isolating the terms quadratic in the gauge fields, we get

$$\frac{g^2 v^2}{4} W_\mu^- W_\mu^+ + \frac{1}{2} \frac{v^2}{4} (g^2 + g'^2) (\cos \theta_w W_\mu^3 - \sin \theta_w B_\mu)^2$$

where  $W_\mu^\pm = (W_\mu^1 \pm i W_\mu^2)/\sqrt{2}$  and  $\theta_w = \tan^{-1}(g'/g)$  is the *Weinberg angle*, which parameterizes the mixing between the photon  $A_\mu$  and the  $Z$  boson  $Z_\mu$ .

$$\begin{pmatrix} Z_\mu \\ A_\mu \end{pmatrix} = \begin{pmatrix} \cos \theta_w & -\sin \theta_w \\ \sin \theta_w & \cos \theta_w \end{pmatrix} \begin{pmatrix} W_\mu^3 \\ B_\mu \end{pmatrix} \quad (2.3)$$

The product  $W_\mu^+ W_\mu^-$  can be interpreted as a mass term for a charged vector boson,  $W_\mu^\pm$ . Collecting the terms quadratic in  $W_\mu^\pm$  and  $Z_\mu$ , we get

$$\mathcal{L}_{\text{mass terms}} = \frac{e^2 v^2}{4 \sin^2 \theta_w} W_\mu W^\mu + \frac{e^2 v^2}{8 \sin^2 \theta_w \cos^2 \theta_w} Z_\mu Z^\mu.$$

Thus, after accounting for symmetry factors, we get the masses of the  $W$  and  $Z$  bosons as:

$$m_W = \frac{ev}{2 \sin \theta_w}, \quad m_Z = \frac{ev}{\sin 2\theta_w}.$$

We see that there is no mass term for  $A_\mu$ . Thus the  $W$  and  $Z$  bosons gain mass, limiting their range, while the photon remains massless, corresponding to what is experimentally observed. Remarkably, we have done this without violating gauge invariance. Colloquially, we say that the  $W$  and  $Z$  bosons have ‘eaten’ the Goldstone boson degrees of freedom to obtain mass.

Peter Higgs was the first to postulate the existence of a physical scalar particle that could be produced by perturbing the vacuum. To see how this plays out, let us parameterize the Higgs doublet field as

$$H = \frac{1}{\sqrt{2}} \exp \left( i \xi^a(x) \frac{\tau^a}{v} \right) \begin{pmatrix} 0 \\ v + h(x) \end{pmatrix}.$$

where  $\tau^a$  are the Pauli matrices,  $\xi^a$  and  $h$  are scalar fields with VEVs given by  $\langle \xi \rangle = \langle h \rangle = 0$ , and  $v$  is the vacuum expectation value of the Higgs doublet, experimentally measured to be about 246 GeV. The field  $h$  is known as the *Higgs boson*. The simplest gauge choice to examine this scenario is the unitary gauge, where  $\xi(x) = 0$ . In this gauge, the potential  $V(H)$  from (2.2) becomes:

$$V(H) = -\frac{1}{2} m_h^2 h^2 - \lambda v h^3 - \frac{1}{4} \lambda h^4$$

The Higgs boson is the only fundamental scalar in the Standard Model, and was discovered in 2012, nearly 50 years after it was first predicted. The coefficient of the term quadratic in  $h$  is its mass,  $m_h$  - a free parameter that had to be determined experimentally. The second and third terms in the above expression represent the trilinear and quartic self-coupling of the Higgs boson.

### Quark mass and gauge eigenstates

While the quarks listed in table 2.2 are *gauge eigenstates*, with well defined transformations under the gauge groups, the physical states that we observe at a collider will in fact be *mass eigenstates*. The two are related by the *Cabibbo-Kobayashi-Maskawa (CKM)* matrix:

*The Cabibbo-Kobayashi-Maskawa quark mixing matrix*

$$V_{\text{CKM}} = \begin{pmatrix} V_{ud} & V_{us} & V_{ub} \\ V_{cd} & V_{cs} & V_{cb} \\ V_{td} & V_{ts} & V_{tb} \end{pmatrix} \quad (2.4)$$

The elements of the matrix denote the level of mixing between the gauge eigenstates. Experimentally, this matrix has been determined to be nearly diagonal.

### Asymptotic freedom and QCD

In the 50s and 60s, experiments were devised to unravel the structure of the proton. They found two seemingly incompatible results. On the one hand, colliding protons resulted in the production of a large number of pions collinear with the beam axis, implying that the protons could not absorb a large momentum transfer. However, deep inelastic scattering experiments later showed that it was possible for an energetic electron to undergo hard electromagnetic scattering off a proton. These disparate phenomena were reconciled by the introduction of the *parton model* by Bjorken and Feynman. In this model, hadrons such as the proton were comprised of a collection of loosely bound pieces, known as partons (for an artistic representation, see figure 2.1). To an energetic incoming electron, these partons would appear approximately free, allowing it to scatter with a large momentum transfer off of one of them. The struck parton will then exchange momentum softly via the strong interaction among the other partons, which results in the production of a *jet* of hadrons, collinear with the direction of the original struck parton. The deeper reason for this behavior is that these partons are charged under a non-Abelian gauge group,  $SU(3)$ . The phenomenon of the weakening of the interaction strength at large momentum transfers is known as *asymptotic freedom*, and it is a property of non-Abelian gauge theories.

The  $\beta$ -function of a gauge theory describes the evolution of the renormalized coupling constant with energy. For non-Abelian gauge theories, it takes the following form (up to leading order):

$$\beta(g_R) = \mu \frac{d}{d\mu} g_R = -\frac{g_R^3}{(4\pi)^2} \left[ \frac{11}{3} C_A - \frac{4}{3} n_f T_F \right] \quad (2.5)$$

where  $\mu$  is the renormalization scale,  $C_A$  is the quadratic Casimir operator for the adjoint representation, and  $T_F$  is the *index* of the fundamental representation. In the case of the strong interaction, the relevant gauge group is  $SU(3)$ . Thus  $C_A = 3$  and  $T_F = \frac{1}{2}$ . If  $n_f$ , the number of quark flavors is less than 17<sup>1</sup>, the  $\beta$  function has a *negative* sign, which means that the coupling *decreases* at higher energies. This is the underlying basis of asymptotic freedom. The theory of the strong interaction is known as *quantum chromodynamics*, or QCD for short. The analogue of electric charge for this theory is a quantity referred to as *color* (hence the name of the theory). At a hadron collider, it is of crucial importance to understand the physics of gluons and jets.

The Standard Model of particle physics has been remarkably successful, and over the decades has yielded some of the most precise measurements in all of physics. However, as mentioned in chapter 1, there still remain unresolved issues with it. In the next two sections we will discuss some of these issues in more depth, and introduce extensions to the SM that potentially resolve them.

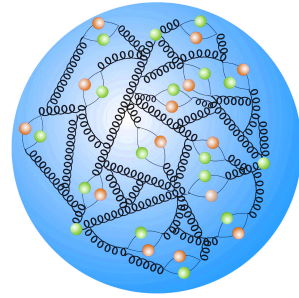


**Figure 2.1:** A representation of the innards of a proton, showing the dynamic structure.  
Source: [1]

*Leading order  $\beta$ -function for non-Abelian gauge theories*

<sup>1</sup>Which it is, since the number of quark flavors is six, as can be seen in table 2.2.

## 2.2 Two-Higgs Doublet Models

Intuitively, it is not too hard to imagine, based on the complex structure of the fermion and gauge sectors of the Standard Model, that its scalar sector might well contain members other than a single  $SU(2)$  doublet. An extended scalar sector frequently arises in BSM theories that potentially alleviate some of the unresolved issues facing the Standard Model. One of these issues is the *strong CP problem*, which can be summarized as follows. Lagrangians for Yang-Mills theories can have a renormalizable term that is gauge-invariant but violates CP, of the form

$$\mathcal{L}_\theta = \theta \epsilon^{\mu\nu\alpha\beta} F_{\mu\nu}^a F_{\alpha\beta}^a,$$

where  $\theta$  is some angle,  $F_{\mu\nu}^a$  are the field strength tensors, and  $\epsilon^{\mu\nu\alpha\beta}$  is an antisymmetric tensor. This term is a total derivative, since it can be written as  $2\theta\partial_\mu(\epsilon^{\mu\nu\alpha\beta} A_\nu^a F_{\alpha\beta}^a)$ . Thus, it should not contribute to perturbative effects. However, this term can potentially contribute to non-perturbative effects. Additionally, this term can be modified by chiral rotations of the form  $\psi \rightarrow \exp(i\gamma_5\theta_F)\psi$ . Since physical observables should be independent of the choice of the basis, i.e.  $\theta_F$ , we should absorb it into  $\theta$  by defining a basis-independent phase:  $\bar{\theta} = \theta - \theta_F$ . For  $SU(2)$  and  $U(1)$  gauge symmetries, this phase can be set to zero by performing appropriate chiral rotations of the fermion fields. However, no such choice exists for the term corresponding to the  $SU(3)$  group, and thus the CP-violating term in the QCD Lagrangian could in principle be non-zero. A non-zero value of  $\bar{\theta}$  would be manifested as non-perturbative effects. For example, the neutron would then have a non-zero electric dipole moment. However, experiments have shown that  $\bar{\theta}$  must be vanishingly small, with a stringent upper bound:  $\bar{\theta} < 10^{-10}$ . A value this small seems suspiciously *fine-tuned* in the absence of an underlying symmetry to enforce it.

Adding an additional scalar doublet allows us to impose such a symmetry - a global  $U(1)$  symmetry known as *Peccei-Quinn* symmetry. If this symmetry is spontaneously broken, a Goldstone boson arises, which can then be chirally rotated such that  $\bar{\theta}$  becomes effectively zero for the ground state. Extended scalar sectors also arise in theories that can explain the observed imbalance between matter and antimatter in the universe. The CP violation in the weak sector of the Standard Model cannot account for this imbalance, but 2HDMs, with their complex scalar sector and possible new sources of CP violation, can. However, the strongest motivation for 2HDMs is their connection to supersymmetric models that have the potential to resolve the hierarchy problem, discussed in the next section. The scalar sector of the Minimal Supersymmetric Standard Model has a structure similar to that of a 2HDM - it requires exactly two scalar doublets to give mass to both up and down type fermions, and for the cancellation of anomalies. With these motivations for 2HDMs in mind, let us examine the structure of the scalar potential of a generic Two-Higgs Doublet Model.

### The 2HDM scalar potential

The most general renormalizable scalar potential for two scalar doublets  $\Phi_1$  and  $\Phi_2$  with hypercharge +1 is given by

$$\begin{aligned} V(\Phi_1, \Phi_2) = & m_{11}^2 |\Phi_1|^2 + m_{22}^2 |\Phi_2|^2 - m_{12}^2 (\Phi_1^\dagger \Phi_2 + \text{h.c.}) \\ & + \frac{\lambda_1}{2} |\Phi_1|^4 + \frac{\lambda_2}{2} |\Phi_2|^4 + \lambda_3 |\Phi_1|^2 |\Phi_2|^2 + \lambda_4 |\Phi_1^\dagger \Phi_2|^2 \\ & + \left[ \frac{\lambda_5}{2} (\Phi_1^\dagger \Phi_2)^2 + \lambda_6 |\Phi_1|^2 (\Phi_1^\dagger \Phi_2) + \lambda_7 |\Phi_2|^2 (\Phi_1^\dagger \Phi_2) + \text{h.c.} \right] \end{aligned} \quad (2.6)$$

*Scalar potential for a Two-Higgs Doublet Model*

where h.c. stands for the hermitian conjugate of the terms immediately preceding it. The parameters  $m_{11,22}^2$  and  $\lambda_{1,2,3,4}$  are real while the parameters  $m_{12}^2$  and  $\lambda_{5,6,7}$  can be complex. Naively, it would seem that this potential has 14 degrees of freedom - six from the real parameters, and eight from the complex parameters. However, it should be noted that we have the freedom to perform basis transformations, that is, we can write the potential in terms of new doublets  $\Phi'_a = \sum_{b=1}^2 U_{ab} \Phi_b$ , where  $U_{ab}$  is a  $2 \times 2$  unitary matrix. The condition of unitarity implies that  $U$  has three degrees of freedom, which can absorb three out of the 14 degrees of freedom listed earlier. Thus, only 11 out of the original 14 degrees of freedom are physical.

In principle, we could proceed with these 11 parameters, however, there are a couple of reasons to attempt to reduce this number. The first is that a large number of free parameters makes a theory less falsifiable, thus reducing its predictive power. The second is that in order to distinguish between pseudoscalars and scalars, CP must be conserved in the Higgs sector. Finally, the potential in (2.6) allows for tree-level flavor-changing neutral currents (FCNC), which are experimentally measured to be highly suppressed. These can be eliminated by introducing discrete or continuous symmetries. Imposing a discrete symmetry such as  $Z_2$ <sup>2</sup> removes the terms that are odd in  $\Phi_i$ . This effectively sets  $\lambda_6 = \lambda_7 = 0$ . In principle, this should set  $m_{12} = 0$  as well, but we retain this term since it breaks the  $Z_2$  symmetry softly, relaxing the experimental bounds on the mass spectrum. After imposing these constraints, all the remaining parameters  $\lambda_{1,2,3,4,5}$ ,  $m_{11,12,22}^2$  are real. From here on, we will only consider 2HDMs with these constraints.

There are four such models, classified based on the coupling patterns of the fermions to the two Higgs doublets. In Type I 2HDMs, all the quarks couple to only one of the Higgs doublets, chosen by convention to be  $\Phi_2$ . In Type II 2HDMs, the up-type right-handed quarks ( $u, c, t$ ) couple to  $\Phi_2$ , and the down-type right-handed quarks ( $d, s, b$ ) couple to  $\Phi_1$ . In both of these models, the right-handed leptons couple to the same doublet as the down-type quarks. The lepton-specific model is similar to the Type I model, except in this case, the right-handed leptons couple to  $\Phi_1$ . Similarly, the ‘flipped’ model is similar to the Type II 2HDM, except

<sup>2</sup>That is, the Lagrangian is invariant under the reflection of one of the doublets:

$$\Phi_i \rightarrow -\Phi_i$$

Model	$u_R^i$	$d_R^i$	$e_R^i$
Type I	$\Phi_2$	$\Phi_2$	$\Phi_2$
Type II	$\Phi_2$	$\Phi_1$	$\Phi_1$
Lepton-specific	$\Phi_2$	$\Phi_2$	$\Phi_1$
Flipped	$\Phi_2$	$\Phi_1$	$\Phi_2$

**Table 2.3:** Fermion coupling patterns for 2HDMs with flavor conservation.

that the leptons couple to  $\Phi_2$ . The coupling patterns for these models are collected in [table 2.3](#).

The scalar potential  $V(\Phi_1, \Phi_2)$  is minimized for non-zero vacuum expectation values of  $\Phi_i$ :

$$\langle \Phi_i \rangle_0 = \begin{pmatrix} 0 \\ \frac{v_i}{\sqrt{2}} \end{pmatrix}. \quad (2.7)$$

where  $v_i$  are the vacuum expectation values of the doublets  $\Phi_i$ . These doublets can then be written as follows:

$$\Phi_i = \begin{pmatrix} \phi_i^+ \\ \frac{1}{\sqrt{2}}(v_i + \rho_i + i\eta_i) \end{pmatrix} \quad (2.8)$$

where  $\phi_i^+$  are complex charged scalars, and  $\rho_i$  and  $\eta_i$  represent the real and complex degrees of freedom of the neutral components of the doublets. The two doublets, each with two complex components, embody eight degrees of freedom in total. The process of electroweak symmetry breaking causes three of these degrees of freedom to be ‘eaten’ by the  $W$  and  $Z$  bosons, and the remaining five are manifested as physical scalar fields. These consist of a pair of CP-even neutral scalars  $h$  and  $H$ , a CP-odd pseudoscalar  $A$ , and a charged scalar  $H^\pm$ .

### The 2HDM mass spectrum

In this section, we will analyze the mass spectrum of flavor-conserving 2HDMs. To do so, we construct the mass matrices by taking derivatives of the scalar potential

$$M_{ij} = \frac{\partial V(\Phi_1, \Phi_2)}{\partial \phi_i \partial \phi_j},$$

where  $\phi_i$  can be any of the fields  $\phi_i^+, \rho_i, \eta_i$  in [\(2.8\)](#). Applying this procedure to the charged scalar components  $\phi_i^\pm$ , we obtain their mass matrix  $M_{\phi^\pm}$ :

$$M_{\phi^\pm} = [m_{12}^2 - (\lambda_4 + \lambda_5)v_1v_2] \begin{pmatrix} v_2/v_1 & -1 \\ -1 & v_1/v_2 \end{pmatrix}.$$

Diagonalizing this matrix gives us the mass of the charged Higgses:

$$m_{H^\pm}^2 = (v_1^2 + v_2^2) [m_{12}^2/v_1v_2 - (\lambda_4 + \lambda_5)].$$

Similarly, the mass matrix for the pseudoscalars is given by

$$M_\eta = \frac{m_A^2}{v_1^2 + v_2^2} \begin{pmatrix} v_2^2 & -v_1v_2 \\ -v_1v_2 & v_1^2 \end{pmatrix}.$$

Diagonalizing it gives us a massless Goldstone boson  $G^0$ , corresponding to a zero eigenvalue, and a pseudoscalar Higgs boson  $A$ , with mass given by

$$m_A^2 = (v_1^2 + v_2^2) [m_{12}^2/v_1v_2 - 2\lambda_5].$$

The diagonalization process amounts to a rotation of the basis vectors by some angle. For the CP-odd and the charged scalars, this angle is the same, and is denoted as  $\beta$ . Given that the couplings of the Higgs bosons in 2HDMs depend on this angle and the angle  $\alpha$  (2.10), let us adopt the notation

$$s_\theta, c_\theta, t_\theta = \sin \theta, \cos \theta, \tan \theta$$

for brevity. In this notation, the mass eigenstates are given by

$$\begin{pmatrix} A \\ G^0 \end{pmatrix} = \begin{pmatrix} s_\beta & -c_\beta \\ c_\beta & s_\beta \end{pmatrix} \begin{pmatrix} \eta_1 \\ \eta_2 \end{pmatrix} \quad \text{and} \quad \begin{pmatrix} H^\pm \\ G^\pm \end{pmatrix} = \begin{pmatrix} s_\beta & -c_\beta \\ c_\beta & s_\beta \end{pmatrix} \begin{pmatrix} \phi_1^\pm \\ \phi_2^\pm \end{pmatrix}. \quad (2.9)$$

The angle  $\beta$  turns out to be a very important one for studying 2HDMs. It also represents the ratio of the vacuum expectation values of the neutral components of the two Higgs doublets:  $t_\beta = v_2/v_1$ . Finally, the mass matrix for the CP-even scalars is given by

$$M_\rho = - \begin{pmatrix} m_{12}^2 \frac{v_2}{v_1} + \lambda_1 v_1^2 & -m_{12}^2 + \lambda_{345} v_1 v_2 \\ -m_{12}^2 + \lambda_{345} v_1 v_2 & m_{12}^2 \frac{v_2}{v_1} + \lambda_1 v_2^2 \end{pmatrix},$$

where  $\lambda_{345} = \lambda_3 + \lambda_4 + \lambda_5$ . This matrix is diagonalized by rotation of the basis vectors by the angle  $\alpha$ :

$$\begin{pmatrix} h \\ H \end{pmatrix} = \begin{pmatrix} s_\alpha & -c_\alpha \\ -c_\alpha & -s_\alpha \end{pmatrix} \begin{pmatrix} \rho_1 \\ \rho_2 \end{pmatrix}. \quad (2.10)$$

The mass eigenstates are labeled  $h$  and  $H$ , with  $h$  traditionally taken to be the lighter of the two.

Thus we see that the physical spectrum of 2HDMs contains five mass eigenstates: the CP-even higgses  $h$  and  $H$ , the CP-odd pseudoscalar Higgs  $A$ , and a pair of charged Higgses  $H^\pm$ . Incidentally, the Standard Model Higgs is taken to be a combination of the CP-even Higgses:

$$h_{\text{SM}} = \rho_1 c_\beta + \rho_2 s_\beta = h s_{\alpha-\beta} - H c_{\alpha-\beta}. \quad (2.11)$$

### 2HDM Interactions

In this section, we discuss the 2HDM interactions that are relevant to our analyses, namely, the ones governing the exotic decays of Higgses to other, lighter Higgses, and the subsequent decays of the lighter Higgses to SM fermions. The decays to SM fermions are governed by the Yukawa terms in the Lagrangian:

$$\begin{aligned} \mathcal{L}_{\text{Yukawa}}^{\text{2HDM}} = & - \sum_{f=u,d,l} \frac{m_f}{v} \left( \xi_h^f \bar{f} f h + \xi_H^f \bar{f} f H - i \xi_A^f \bar{f} \gamma_5 f A \right) \\ & - \left\{ \frac{\sqrt{2} V_{ud}}{v} \bar{u} (m_u \xi_A^u P_L + m_d \xi_A^d P_R) d H^+ + \frac{\sqrt{2} m_l \xi_A^l}{v} \bar{\nu}_L l_R H^+ + h.c. \right\} \end{aligned} \quad \text{Yukawa interactions}$$

where  $f$  is a fermion with mass  $m_f$ , the fields  $u$  and  $d$  are up and down type quarks with masses  $m_u$  and  $m_d$  and CKM mixing  $V_{ud}$ ,  $l$  is a lepton

Coefficient	Value
$\xi_h^u$	$c_\alpha/s_\beta$
$\xi_h^d$	$-s_\alpha/c_\beta$
$\xi_h^l$	$-s_\alpha/c_\beta$
$\xi_H^u$	$s_\alpha/s_\beta$
$\xi_H^d$	$c_\alpha/s_\beta$
$\xi_H^l$	$c_\alpha/s_\beta$
$\xi_A^u$	$1/t_\beta$
$\xi_A^d$	$t_\beta$
$\xi_A^l$	$t_\beta$

**Table 2.4:** The factors  $\xi$  that determine the Yukawa couplings of Higgs bosons in Type II 2HDMs.

with mass  $m_l$ , and  $\nu_L$  is a neutrino. The factors  $\xi$  in the above expressions depend on the specific model being considered. For the Type II 2HDM, they take the values listed in [table 2.4](#).

For the exotic decays, we can obtain the coupling strengths from the kinetic terms for the fields  $\Phi_i$ , similar to what we do for the SM electroweak interactions. With a little bit of work, we can extract the following couplings (see [[12](#)] for details):

$$\begin{aligned} g_{AH^\pm W^\mp} &= \frac{g}{2}(p_{H^\pm} - p_A)^\mu \\ g_{hAZ} &= is_{\beta-\alpha}\frac{g}{2c_{\theta_w}}(p_A - p_h)^\mu \\ g_{hH^\pm W^\mp} &= -is_{\beta-\alpha}\frac{g}{2}(p_{H^\pm} - p_h)^\mu \\ g_{HAZ} &= ic_{\beta-\alpha}\frac{g}{2c_{\theta_w}}(p_A - p_H)^\mu \\ g_{HH^\pm W^\mp} &= -ic_{\beta-\alpha}\frac{g}{2}(p_{H^\pm} - p_H)^\mu. \end{aligned}$$

### The Type II 2HDM

The Type II 2HDM is of special interest to us since it has the same fermion-Higgs doublet coupling pattern as the MSSM. The MSSM will be examined in more detail in the next section, but we will note that we can recover the tree-level MSSM scalar potential from a Type II 2HDM by setting the parameters  $\lambda_i$  to the following values:

$$\lambda_{1,2} = \frac{g^2 + g'^2}{2}, \quad \lambda_3 = \frac{g^2 - g'^2}{4}, \quad \lambda_4 = -\frac{g^2}{2}, \quad \lambda_{5,6,7} = 0. \quad (2.12)$$

It should also be noted, however, that these relations do not hold beyond the tree-level for a generic non-supersymmetrized 2HDM. The analyses in chapters [4](#) and [5](#) are designed to probe the parameter space of a Type II 2HDM.

## 2.3 The Minimal Supersymmetric Standard Model

Historically, examining nature at increasing energy scales has consistently yielded new physics. For example, higher-energy experiments were able to probe the structure of the weak interactions, precisely at the energy scale that the 4-Fermi theory started to fail. Similarly, the challenges such as the strong CP problem described at the beginning of [section 2.2](#) most likely point to new physics at higher energy scales, between the currently explored weak scale and the reduced Planck scale,

$$M_P = 1/\sqrt{8\pi G} \approx 2.4 \times 10^{18} \text{ GeV}.$$

However, the SM Higgs potential is extremely sensitive to new physics at high energies. The square of the mass of the SM Higgs boson receives large quantum corrections from any new physics at high energies that couples to the scalar sector. For example, if the Higgs couples to a heavy

fermion  $f$  through a term of the form  $-\lambda_f H \bar{f} f$ , the one-loop correction to the square of the Higgs mass (figure 2.2) takes the form

$$\Delta m_H^2 = -\frac{|\lambda_f|^2}{8\pi^2} \Lambda_{UV}^2 + \dots, \quad (2.13)$$

where  $\Lambda_{UV}$  is some cutoff momentum at which the effects of the new physics are expected to manifest themselves. Similarly, the one-loop correction from a heavy scalar  $S$  through the term  $-\lambda_S |H|^2 |S|^2$  (figure 2.3) takes the form

$$\Delta m_H^2 = \frac{\lambda_S}{16\pi^2} [\Lambda_{UV}^2 + \dots]. \quad (2.14)$$

In both of these cases, the size of the correction scales quadratically with the momentum cutoff  $\Lambda_{UV}$ . Higher-order loop corrections can be shown to be similarly large as well. Thus the ‘natural’ mass of the Higgs would seem to be on the order of  $\Lambda_{UV}$ , which could even be as high as the Planck scale. In contrast, the actual mass that we measure is only about 126 GeV. Thus, there seems to be a *hierarchy* between the observed and the ‘natural’ mass of the SM Higgs, one of many orders of magnitude<sup>3</sup>.

As a consequence, any UV completion of the SM would have to come with a host of parameters to tune the counterterms enough to cancel out the quadratic divergences and result in the physical mass we observe experimentally. It is obviously undesirable to have to manually tune such a large number of parameters - it would be analogous to the geocentric Ptolemaians adding an ever-increasing number of epicycles to explain what would ultimately be more simply and accurately described by Copernicus’ heliocentric theory. This is known as the *hierarchy problem*. Looking at the forms of the one-loop corrections in (2.13) and (2.14), we can see that the contribution from the fermion  $f$  will be exactly canceled out by the contributions from two complex scalars with  $\lambda_S = |\lambda_f|^2$ . This suggests that the simplest way to ensure that all quadratic divergences from new physics at high energy scales cancel out is to require some kind of symmetry between fermions and scalars, ensuring that there is a scalar counterpart for each fermion, and vice versa.

As it turns out, there is in fact such a symmetry, known as *supersymmetry*. It is a rich mathematical structure with far-reaching consequences, a lot of which are beyond the scope of this work. The term ‘supersymmetry’ refers to the invariance of the Lagrangian under transformations of the form<sup>4</sup>

$$Q|Boson\rangle = |Fermion\rangle \quad \text{and} \quad Q|Fermion\rangle = |Boson\rangle.$$

The minimal phenomenologically viable incorporation of supersymmetry into the Standard Model is known as the *Minimal Supersymmetric Standard Model*, or the MSSM. Although the hierarchy problem has been the main driving force behind the development of supersymmetry, there are other motivations to study it as well. One of them is that it has the right particle content to unify the strong and electroweak couplings at a high energy scale, as seen in figure 2.4.

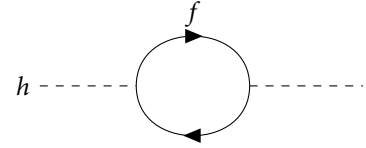


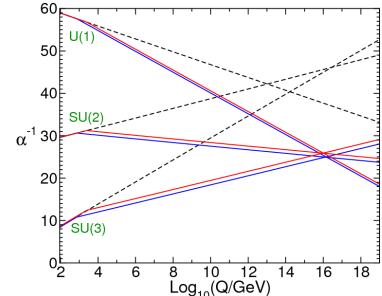
Figure 2.2: Feynman diagram for the one-loop fermionic correction to the SM Higgs mass



Figure 2.3: Feynman diagram for the one-loop scalar correction to the SM Higgs mass

<sup>3</sup>Note that even though only the mass of the SM Higgs is directly sensitive to  $\Lambda_{UV}$ , this sensitivity is propagated to all the other SM particles through their couplings to the SM Higgs.

Figure 2.4: 2-loop RG evolution of inverse gauge couplings in the SM (dashed lines) and the MSSM (solid lines). Source: [10].



The sparticle masses are varied between 0.5-1.5 TeV, and  $\alpha_3(m_Z)$  is varied between 0.117 and 0.121.

<sup>4</sup>Of course, these are not the precise forms of the transformations, as can be seen by performing some rudimentary dimensional analysis. We will encounter the more precise forms later.

The third major motivation (and the one most relevant to this dissertation) is the fact that the MSSM contains a viable dark matter candidate. The theory admits a new kind of discrete symmetry known as *R-parity*, which is an analogue of baryon and lepton number conservation. The Lagrangian of the MSSM is defined to be invariant under the action of the operator  $P_R$ , with eigenvalues  $(-1)^{3(B-L)+2s}$ , where  $B$ ,  $L$ , and  $s$  represent the baryon number, lepton number, and spin of the field that is acted upon, respectively. As a consequence of this symmetry, the lightest supersymmetric particle (LSP) cannot decay further into other particles, thus making it a good candidate for dark matter.

### *The supersymmetry algebra*

In 1967, Coleman and Mandula [13] showed that, given certain assumptions, the only possible Lie group symmetries allowed for relativistic interacting field theories in four dimensions are direct products of the Poincaré group and an internal symmetry group (i.e. a gauge symmetry) [14]. A Lie algebra is defined by the commutation relations of its generators. If we extend the notion of a Lie algebra to include *anticommutation* relations [15], this restriction no longer applies. These kinds of algebras are known as *graded Lie algebras*, or *superalgebras*. The trio of Haag, Łopuszanski, and Sohnius [16] applied a similar treatment as Coleman and Mandula to determine the most general superalgebra consistent with relativistic quantum field theory. The generators  $Q_\alpha$  of this algebra are known as fermionic operators, and must transform as Weyl spinors. The anticommutation (and commutation) relations take the form

$$\begin{aligned} \{Q_\alpha, \bar{Q}_\beta\} &= 2(\sigma^\mu)_{\alpha\dot{\beta}} P^\mu \\ \{Q_\alpha, Q_\beta\} &= \{\bar{Q}_{\dot{\alpha}}, \bar{Q}_{\dot{\beta}}\} = 0 \\ [P^\mu, Q_\alpha] &= [P^\mu, \bar{Q}_{\dot{\alpha}}] = 0 \end{aligned} \quad (2.15)$$

### *The supersymmetry algebra*

where  $P_\mu = i\partial_\mu$  is the generator of translations.

The first supersymmetric Lagrangian density in four-dimensions was formulated by Wess and Zumino [15]. The approach taken was to define infinitesimal ‘supergauge’ transformations for scalars and spinors that generated a closed algebraic structure. Soon afterwards, Salam and Strathdee [17] created a more systematic approach to constructing these transformations, by giving them a geometric interpretation.

In this picture, supersymmetric transformations can be viewed as translations in a manifold known as *superspace*, which is obtained by adding the ‘fermionic’ coordinates  $\theta^\alpha$  and  $\bar{\theta}^{\dot{\beta}}$  to the regular ‘bosonic’ spacetime coordinates  $x^\mu$ . The generators of these translations are represented by

$$Q_\alpha = \frac{\partial}{\partial\theta^\alpha} - i(\sigma^\mu\bar{\theta})_\alpha\partial_\mu \quad \text{and} \quad \bar{Q}_{\dot{\beta}} = \frac{\partial}{\partial\bar{\theta}^{\dot{\beta}}} - i(\sigma^\mu\bar{\theta})_{\dot{\beta}}\partial_\mu. \quad (2.16)$$

These transformations act on objects known as superfields, which are complex scalar fields parameterized by the coordinates  $(x^\mu, \theta, \bar{\theta})$ . Under

### *Generators of superspace translations*

an infinitesimal supersymmetry transformation, a general superfield  $S(x, \theta, \bar{\theta})$  transforms as

$$S \rightarrow S' = (1 + i\xi^\alpha Q_\alpha + i\bar{\xi}_{\dot{\alpha}} \bar{Q}^{\dot{\alpha}})S \quad (2.17)$$

where  $\xi^\alpha$  and  $\bar{\xi}_{\dot{\alpha}}$  are two-component Weyl spinor fields that parameterize the translation. The fermionic coordinates  $\theta$  and  $\bar{\theta}$  each have two components. For example,  $\theta$  can be represented as  $\theta^\alpha = (\theta^1, \theta^2)$ . Each of these two components is a *Grassmannian* variable, satisfying the anticommutation relation  $\{\theta^i, \theta^j\} = 0$ . This implies that  $(\theta^i)^2 = 0$ . This means that a Taylor expansion in powers of a fermionic coordinate must always terminate with a finite number of terms. For a general superfield  $S$ , the Taylor expansion about the fermionic coordinates  $\theta, \bar{\theta}$  takes the form

$$S(x, \theta, \bar{\theta}) = a + \theta\xi + \bar{\theta}\chi^\dagger + \theta\theta b + \bar{\theta}\bar{\theta}c + \bar{\theta}\bar{\sigma}^\mu\theta\nu_\mu + \bar{\theta}\bar{\theta}\theta\eta + \theta\theta\bar{\theta}\zeta^\dagger + \theta\theta\bar{\theta}\bar{\theta}d, \quad (2.18) \quad \text{General superfield expansion}$$

where  $a, b, c$  and  $d$  are complex-valued scalar fields,  $\xi, \chi, \eta$  and  $\zeta$  are spinor fields, and  $\nu_\mu$  is a vector field. These coefficients in the Taylor expansion will be identified with the regular (non-super) fields that we see in the SM and its supersymmetrized version, the MSSM. The matter content of the MSSM can be derived from expanding superfields of a particular type, known as *chiral* superfields, with mass dimension 1. The expansion of a generic chiral superfield  $\Phi$  takes the form:

$$\begin{aligned} \Phi(y, \theta) = & \phi(x) + \sqrt{2}\theta\psi(x) + \theta\theta F(x) \\ & + i\theta\sigma\bar{\theta}\partial_\mu\phi(x) - \frac{1}{2}\theta\sigma\bar{\theta}\theta\sigma^\nu\bar{\theta}\partial_\mu\partial_\nu\phi(x) + \sqrt{2}\theta i\theta\sigma\bar{\theta}\partial_\mu\psi(x) \end{aligned} \quad (2.19) \quad \text{Chiral superfield expansion}$$

Similarly the gauge bosons come from the expansion of dimension-0 *vector* superfields  $V$ , obtained by imposing the condition  $V = V^\dagger$ . The expansion of  $V$  takes the form:

$$V = \bar{\theta}\bar{\sigma}^\mu\theta A_\mu + \bar{\theta}\bar{\theta}\theta\lambda + \theta\theta\bar{\theta}\lambda^\dagger + \frac{1}{2}\theta\theta\bar{\theta}\bar{\theta}D. \quad (2.20) \quad \text{Vector superfield expansion}$$

We see that the expansion of the chiral superfield  $\Phi$  contains a scalar field  $\phi$ , a Weyl fermion  $\psi$ , and a field  $F$ . Thus, choosing values of  $\phi, \psi$ , and  $F$  fixes  $\Phi$ . These fields, known as the *component fields* of  $\Phi$  can be naturally placed in a collection known as a *supermultiplet*. The scalar superpartners  $\phi$  are referred to as *sfermions*. Similarly, the vector field  $A_\mu$ , the fermion field  $\lambda$ , and the field  $D$  form another natural grouping, called a *vector supermultiplet*. The fields  $A_\mu$  and  $\lambda$  are superpartners of each other, and fields such as  $\lambda$  are generically known as *gauginos*. The particle content of the MSSM, grouped into supermultiplets, is shown in tables 2.5 and 2.6. For brevity, we have not shown all three fermion generations. Also, the fields  $F$  and  $D$  are not included, since they are *auxiliary* fields, serving only to make sure that supersymmetry holds

off-shell. The gauge structure of the MSSM is the same as that of the SM - there are no new gauge interactions.

The mass terms and Yukawa terms of the MSSM Lagrangian come from the collection of terms known as the *superpotential*. In terms of the chiral superfields in [table 2.5](#), we can write the MSSM superpotential as:

### *The MSSM superpotential*

$$W_{\text{MSSM}} = \bar{u} \mathbf{y}_u Q H_u - \bar{d} \mathbf{y}_d Q H_d - \bar{e} \mathbf{y}_e L H_d + \mu H_u H_d$$

Here, we have abbreviated terms such as  $\mu(H_u)_\alpha(H_d)_\beta \epsilon^{\alpha\beta}$  to  $\mu H_u H_d$ . The matrices  $\mathbf{y}$  are  $3 \times 3$  matrices of Yukawa couplings, with indices corresponding to the three generations of fermions. Note also that we now see the necessity of having two Higgs doublets - one that couples to the up-type fermions, and the other to the down-type fermions. A term like  $\bar{u} \mathbf{y}_u Q H_d^*$  would lead to a non-conserved hypercharge.

### *Softly broken supersymmetry*

The component fields of a superfield have the same mass, as can be seen from expansions of the chiral and vector superfields in [\(2.19\)](#) and [\(2.20\)](#). This means that if supersymmetry holds, the superpartners of the SM particles should have been discovered by now. Evidently, if this symmetry exists, it is not apparent in the ground state that we inhabit - that is, it must be spontaneously broken. The exact mechanism by which it is broken is still unknown - there are a number of competing models which introduce new physics at high energy scales to spontaneously break supersymmetry. To remain model-agnostic, we can parameterize our ignorance by inserting the relevant terms into the Lagrangian by hand, with their form constrained by the requirement that the quadratic divergences in the radiative corrections to scalar masses must still vanish.

The soft supersymmetry breaking terms of the MSSM, written in terms of the component fields from [tables 2.5](#) and [2.6](#) are as follows.

### *Soft supersymmetry breaking terms*

$$\begin{aligned} \mathcal{L}_{\text{soft}}^{\text{MSSM}} = & -\frac{1}{2} (M_1 \tilde{B} \tilde{B} + M_2 \tilde{W} \tilde{W} + M_3 \tilde{g} \tilde{g} + \text{h.c.}) \\ & - \left( \tilde{\bar{u}} \mathbf{a}_u \tilde{Q} H_u - \tilde{\bar{d}} \mathbf{a}_d \tilde{Q} H_d - \tilde{\bar{e}} \mathbf{a}_e \tilde{L} H_d + \text{h.c.} \right) \\ & - \tilde{Q}^\dagger \mathbf{m}_{\tilde{Q}}^2 \tilde{Q} - \tilde{L}^\dagger \mathbf{m}_{\tilde{L}}^2 \tilde{L} - \tilde{\bar{u}}^\dagger \mathbf{m}_{\tilde{\bar{u}}}^2 \tilde{\bar{u}}^\dagger - \tilde{\bar{d}}^\dagger \mathbf{m}_{\tilde{\bar{d}}}^2 \tilde{\bar{d}}^\dagger - \tilde{\bar{e}}^\dagger \mathbf{m}_{\tilde{\bar{e}}}^2 \tilde{\bar{e}}^\dagger \\ & - m_{H_u}^2 H_u^* H_u - m_{H_d}^2 H_d^* H_d - (b H_u H_d + \text{h.c.}) \end{aligned}$$

The tildes denote superpartners of the corresponding SM fields. The parameters  $M_1, M_2, M_3$  govern the masses of the gauginos  $\tilde{B}, \tilde{W}$ , and  $\tilde{g}$ , respectively.

### *Phenomenological approximations*

The MSSM has a number of simplifying assumptions motivated both by calculational convenience and compatibility with observed experimental data. For example, it is convenient to take the Yukawa matrices  $\mathbf{y}_u, \mathbf{y}_d, \mathbf{y}_e$

**Table 2.5:** Chiral supermultiplets of the MSSM.

Superfield	Components		Group representation		
	Spin-0	Spin-½	$SU(3)$	$SU(2)$	$U(1)_Y$
Squarks		Quarks			
Q	$\begin{pmatrix} \tilde{u}_L \\ \tilde{d}_L \end{pmatrix}$	$\begin{pmatrix} u_L \\ d_L \end{pmatrix}$	<b>3</b>	<b>2</b>	$\frac{1}{2}$
$\bar{u}$	$\tilde{u}_R^*$	$u_R^\dagger$	$\bar{\mathbf{3}}$	<b>1</b>	$-\frac{2}{3}$
$\bar{d}$	$\tilde{d}_R^*$	$d_R^\dagger$	$\bar{\mathbf{3}}$	<b>1</b>	$\frac{1}{3}$
Sleptons		Leptons			
L	$\begin{pmatrix} \tilde{v}_L \\ \tilde{e}_L \end{pmatrix}$	$\begin{pmatrix} v_L \\ e_L \end{pmatrix}$	<b>1</b>	<b>2</b>	$-\frac{1}{2}$
$\bar{e}$	$\tilde{e}_R^*$	$e_R^\dagger$	$\bar{\mathbf{1}}$	<b>1</b>	1
Higgses		Higgsinos			
$H_u$	$\begin{pmatrix} H_u^+ \\ H_u^0 \end{pmatrix}$	$\begin{pmatrix} \tilde{H}_u^+ \\ \tilde{H}_u^0 \end{pmatrix}$	<b>1</b>	<b>2</b>	$\frac{1}{2}$
$H_d$	$\begin{pmatrix} H_d^0 \\ H_d^- \end{pmatrix}$	$\begin{pmatrix} \tilde{H}_d^0 \\ \tilde{H}_d^- \end{pmatrix}$	<b>1</b>	<b>2</b>	$-\frac{1}{2}$

**Table 2.6:** Gauge supermultiplets of the MSSM.

Components		Group representation		
Spin-½	Spin-1	$SU(3)$	$SU(2)$	$U(1)_Y$
Gluinos: $\tilde{g}$	Gluons: $g$	<b>8</b>	<b>1</b>	0
Winos: $\tilde{W}^0$	$W$ bosons: $W^\pm$	$\bar{\mathbf{1}}$	<b>3</b>	0
Binos: $\tilde{B}^0$	$B$ bosons: $B^0$	$\bar{\mathbf{1}}$	<b>3</b>	0

in a simplified limit, where only the heaviest generations have non-zero Yukawa couplings:

$$\mathbf{y_u} \approx \begin{pmatrix} 0 & 0 & 0 \\ 0 & 0 & 0 \\ 0 & 0 & y_t \end{pmatrix}, \quad \mathbf{y_d} \approx \begin{pmatrix} 0 & 0 & 0 \\ 0 & 0 & 0 \\ 0 & 0 & y_b \end{pmatrix}, \quad \mathbf{y_e} \approx \begin{pmatrix} 0 & 0 & 0 \\ 0 & 0 & 0 \\ 0 & 0 & y_\tau \end{pmatrix}.$$

Furthermore, to suppress excessive CP-violation and flavor-changing neutral currents in the MSSM, the following approximations are often made. First, we assume that there is minimal mixing among the sfermions:

$$\mathbf{m}_{\tilde{Q}}^2 = m_{\tilde{Q}}^2 \mathbf{1}, \quad \mathbf{m}_{\tilde{u}}^2 = m_{\tilde{u}}^2 \mathbf{1}, \quad \mathbf{m}_{\tilde{d}}^2 = m_{\tilde{d}}^2 \mathbf{1}, \quad \mathbf{m}_{\tilde{e}}^2 = m_{\tilde{e}}^2 \mathbf{1}, \quad \mathbf{m}_{\tilde{L}}^2 = m_{\tilde{L}}^2 \mathbf{1}$$

We also suppress the cubic scalar couplings of the first two families of sfermions by imposing the conditions:

$$\mathbf{a_u} = A_{u0} \mathbf{y_u}, \quad \mathbf{a_d} = A_{d0} \mathbf{y_d}, \quad \mathbf{a_e} = A_{e0} \mathbf{y_e}.$$

Finally, requiring that the soft SUSY breaking parameters are real enables us to suppress excessive amounts of CP violation:

$$\text{Im}(M_1) = \text{Im}(M_2) = \text{Im}(M_3) = \text{Im}(A_{u0}) = \text{Im}(A_{d0}) = \text{Im}(A_{e0}) = 0.$$

With the above ingredients, one can work out myriad phenomenological consequences. In [chapter 6](#), we examine the neutralino sector of the MSSM in slightly more detail, and present an analysis aimed at exploring it at a 100 TeV collider.

# 3

## COLLIDER PHENOMENOLOGY AND MACHINE LEARNING

In this chapter, we will discuss how to connect theory and experiment. We will begin by connecting scattering amplitudes and physically observed cross sections, after which we will briefly discuss detector components of the LHC. We then move on to the question of how we establish statistical significance given experimental data from detectors, and conclude with a discussion of the role of machine learning in particle physics.

To observe physics at subatomic length scales, it is necessary to produce interactions on those scales. This requires colliding particles at speeds close to the speed of light. The energy of these collisions is so high that not only do the colliding particles scatter off of each other, but new particles can be created as well. The physical observable at particle colliders is a quantity known as the scattering cross section, denoted by  $\sigma$ . It is defined by the relation  $R = \sigma \mathcal{L}$ , where  $R$  is the rate of collisions per unit time, and  $\mathcal{L}$  is the luminosity of the collider, that is, the number of particles passing through some cross-sectional area per unit time. The scattering cross-section for a generic process with incoming particles 1 and 2 colliding to produce a set of outgoing particles  $X$  is given by the integral of the scattering amplitude  $|\mathcal{M}_{12 \rightarrow X}|^2$  over the phase space of the outgoing particles<sup>1</sup>:

$$\sigma_{12} = \int d\Pi_X |\mathcal{M}_{12 \rightarrow X}|^2. \quad (3.1)$$

The dynamics of the collision event are contained in the matrix element  $\mathcal{M}$ , which will be influenced by the presence of BSM physics. The typical quantities of interest are the *differential* cross sections,  $d\sigma/dx$ , where  $x$  represents some kinematic variable. Particle colliders are broadly categorized as either lepton or hadron colliders. Each one has its advantages and disadvantages. While lepton colliders have cleaner signals due to the lack of large QCD backgrounds, hadron colliders are able to reach much larger center-of-mass energies, since leptons lose large amounts of energy via synchrotron radiation when forced along a circular path. In this work, we will focus on the phenomenology of hadron colliders.

### 3.1 Detector design for hadron colliders

Particle detectors at colliders can be thought of as sophisticated video-cameras with extremely high framerates. Conversely, the digital cameras that we use in our daily lives can be thought of as particle detectors, except ones designed to detect only one kind of particle, namely, the photon. The response of a detector to an incident particle can take on a variety of forms. In a gaseous detector such as a Geiger-Muller tube, an energetic incident particle will lead to the ionization of a large fraction of the gas molecules. This is followed by a rapid recombination of the ions,

<sup>1</sup>Here we omit the form factors that would come into play at a hadronic collider, without affecting our narrative.

which is manifested as an electrical pulse. The analogue of ionization for a solid-state detector (such as the ones used in regular digital cameras) is the creation of a large number of electron-hole pairs. The design of a particle detector depends upon the particles it is intended to detect, as well as the desired precision and accuracy. At the Large Hadron Collider at CERN, the two major detectors are ATLAS (A Toroidal LHC Apparatus) and CMS (Compact Muon Solenoid). Although they differ in construction, they probe essentially the same physics. The components common to them are the following.

*Tracking chamber.* The innermost part of the detector is the tracking chamber. It consists of layers of solid-state detectors that can accurately measure the paths of charged particles. The presence of a strong magnetic field bends the paths of these particles, enabling us to learn about their charge and mass.

*Calorimeter(s).* If a particle is energetic enough to go beyond the tracking chamber, it enters the calorimeter region. A calorimeter consists of materials dense enough to completely absorb the energy of an incident particle, stopping it in its tracks. At ATLAS and CMS, the calorimeters are actually combinations of two layers that are designed to stop different kinds of particles. The electromagnetic calorimeter is designed to measure the energy of electrons and photons, while the hadronic calorimeter is designed to stop (and you might have guessed this already) hadrons.

*Muon Detectors.* The muon, being about 200 times heavier than the electron, experiences much less energy loss through bremsstrahlung, and is able to bypass both the tracking chamber and calorimeter layers. For this reason, muon detectors form the outermost layer of a particle detector.

A transverse slice of the CMS detector is shown in [figure 3.1](#), depicting the trajectories taken by different kinds of particles through the layers of the detector. The specific design of a detector depends upon the vision of the collaboration running it. With a finite construction and operation budget, tradeoffs must inevitably be made. Although both ATLAS and CMS are state of the art machines, they have their strengths and weaknesses relative to each other based upon different sets of priorities of the collaborations that run them. For this reason, we do not provide the specifics of their construction, and instead point the reader to [\[18\]](#) for a detailed review and comparison of the two. For our purposes, the features of the collision events that we use to perform our analyses (particle momentum, missing transverse energy, etc.) can be obtained from either of these detectors.

*Trigger.* As mentioned in [chapter 1](#), there are hundreds of millions of collisions every second at the LHC. Recording and analyzing all of these events would be impractical, given that most of the collisions are *soft*,

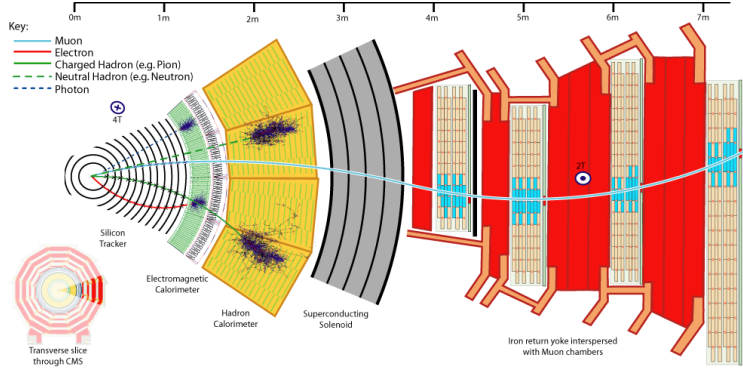


**Figure 3.1:** Transverse slice of the CMS detector, showing the paths of various particles. Source: [19]

involving only small deflections of the colliding particles. What we are really interested in are the *hard* collisions, with the final state particles having large components of momentum in the plane transverse to the beam axis. To filter out the uninteresting events, we employ a *trigger* - that is, a condition that an event must satisfy to be stored for further analysis. For example, in chapter 6, we choose to trigger on a hard lepton, that is, one with a large transverse momentum,  $p_T$ .

*Invisibles.* An important point to note is that certain particles, such as neutrinos and dark matter candidates, escape the detector entirely, leaving no tracks or energy deposits. The existence of one of these ‘invisible’ particles in a collision event can only be inferred from an observed imbalance of momenta of the final state particles in the transverse plane. Thus, for analyses involving neutrinos or dark matter, the kinematic quantity known as *missing transverse energy*, denoted by  $\cancel{E}_T$ , is of utmost importance.

### 3.2 Anatomy of a collider analysis

At its heart, the goal of a collider analysis is to compare the predictions of the SM and BSM theories with actual experimental data, and estimate the level of compatibility between them. To do this well, we need precise theoretical predictions of the differential cross sections that we can expect to see at the collider. This is done with the help of Monte Carlo methods and detector simulations, as described below.

#### Parton-level event generation

As mentioned earlier, the cross section for a scattering process is an integral of the scattering amplitude over the phase space of the final state particles. In general, these integrals do not have a closed form solution, and so we must resort to numerical integration. The simplest Monte Carlo integration method, the *acceptance-rejection* method [20],

involves randomly sampling points within the limits of integration with a uniform probability distribution, and testing whether they lie under the ‘curve’ specified by the integrand. The fraction of points that pass this test, multiplied by the volume of this ‘bounding box’ specified by the integration limits, gives the definite integral. This method is difficult to view in multiple dimensions, but not too hard to grasp in one or two dimensions - see [21] for a brief overview and implementation. However, drawing the random samples from a uniform probability distribution is not the most efficient method for performing Monte Carlo integrals - programs such MadGraph5 and MadEvent [22] do this in more sophisticated ways, determining the most important regions of phase space and concentrating the sampling within those regions. These ‘points’ are simply the particle collision events themselves, with coordinates given by the four-momenta of the final state particles.

#### *Showering and hadronization*

At hadron colliders, dealing with the matrix element  $\mathcal{M}$  alone will not suffice. We must also take into account nonperturbative QCD effects, such as the radiation of soft gluons, and the formation of complex hadronic final states. For example, even if an energetic quark is contained in the final state of a collision event generated by MadEvent, it will not be detected as an elementary particle. It will radiate gluons that themselves split to form new quarks, that subsequently form bound states. This collection of hadronic bound states is termed a *jet*, and has a momentum collinear with the momentum of the original quark. The identity of this quark can be determined (with a finite efficiency) from the properties of the jet. To handle these non-perturbative effects, we interface MadEvent with the program Pythia[23] which performs the steps of *parton showering* and *hadronization*.

#### *Detector simulation and reconstruction*

A full collider analysis carried out by experimentalists will involve detailed simulations of the detector response, using programs such as GEANT4 [24]. For our purposes, however, it is enough to parameterize the response at a higher level - for example, by specifying a fixed probability of identifying a certain particle. This is done using the Delphes 3 framework [25], which provides a way to perform a fast, modular simulation of the detector response.

#### *Hypothesis testing*

After signal and background samples have been generated using Monte Carlo methods and passed through a detector simulation, they are compared to actual experimental data. Doing this enables us to do one or more of the following:

Symbol	Statistical name	Physics name	Probability model
$H_0$	Null	Background-only	$\text{Pois}(n_{SR} v_B)$
$H_1$	Alternate	Signal+Background	$\text{Pois}(n_{SR} v_S + v_B)$

**Table 3.1:** The two competing hypotheses for our simple number counting example. Source: [27].

- Estimate some parameter, for example the mass of a particle, or a coupling strength.
- Set upper limits on the rate of occurrence of a process, and translating those limits into limits on the parameter space of BSM theories.
- Discover a new particle
- Compare theoretical and experimental differential cross sections using a goodness-of-fit test.

As it turns out, all of these can be subsumed into the larger framework of *hypothesis testing* [26]. In the following section, we will address how we answer the question “Does this experimental data imply the existence of new physics (or conversely, rule it out) ?”. This discussion is adapted from the one in [27].

### 3.3 Statistical significance in particle physics

A hypothesis is a claim about what the experimental data will look like. It is associated with a *probability model*, which is just a function that describes the probability of obtaining a certain dataset, given some parameters. Let us consider hypothesis testing in the context of a simple counting experiment. In this experiment, we examine a subset of a dataset  $\mathcal{D}$  that resides in a region of the ‘data space’ labeled the *signal region* (SR), and contains  $n_{SR}$  events. Our competing hypotheses are the ‘background-only’ and ‘signal plus background’ hypotheses, summarized in [table 3.1](#). The probability models associated with these hypotheses are Poisson models<sup>2</sup>. The model for the ‘background-only’ hypothesis is  $\text{Pois}(n_{SR}|v_B)$ , that is, the probability of obtaining  $n_{SR}$  events in the signal region when  $v_B$  events are expected from the background process. The competing hypothesis, ‘signal plus background’, on the other hand, predicts  $v_S + v_B$  events in the signal region, with  $v_S$  events from the signal process and  $v_B$  events from the background process. The probability that the background-only hypothesis will produce at least  $n_{SR}$  events is given by

$$P_{\text{background only}} = \sum_{n=n_{SR}}^{\infty} \text{Pois}(n|v_B)$$

The lower this probability is, the less likely it is that the background-only hypothesis can account for the observed number of events in the signal region. This quantity is also known as the *p*-value - in this case, it is the *p*-value for the background-only hypothesis. The corresponding *p*-value for the signal + background hypothesis is given by:

$$P_{\text{signal + background}} = \sum_{n=n_{SR}}^{\infty} \text{Pois}(n|v_S + v_B)$$

<sup>2</sup>The exact probability distribution for counting experiments is given by the binomial frequency function. In the limit of a large number of events, this approaches the Poisson frequency function, given by

$$\text{Pois}(n|v) = v^n \frac{e^{-v}}{n!}$$

which describes the probability of observing  $n$  events given that the mean expected number of events is  $v$ .

For phenomenology, there are usually two  $p$ -value thresholds of interest. The first is the exclusion threshold - if  $p_{\text{signal} + \text{background}} < 0.05$ , we consider the signal + background hypothesis ‘excluded’. The second is the discovery criterion,  $p_{\text{background only}} < 2.87 \times 10^{-7}$ . When this condition is satisfied, we choose to reject the background-only hypothesis, and claim discovery of new physics. In practice,  $p$ -values are reported in terms of equivalent  $Z$ -values. The  $Z$  value corresponding to a  $p$ -value  $p_0$  is given by

$$Z = \Phi^{-1}(1 - p_0)$$

where  $\Phi^{-1}$  is the inverse of the cumulative distribution function of the standard normal distribution (a Gaussian distribution with mean 0 and variance 1). The equivalent  $Z$ -values for the exclusion and discovery  $p$ -value thresholds are 1.96 and 5, respectively. In particle physics parlance, the equivalent  $Z$  value is known as the *significance*, and is reported as  $Z\sigma$ . The significance is maximized by choosing signal regions with low values of  $v_B$ . This can be seen from the expressions for  $p_{\text{background only}}$ . Lower values of  $v_B$  lead to lower values of  $p_{\text{background only}}$ , minimizing the probability, denoted  $\alpha$ , that we will wrongly reject the background-only hypothesis when it is true. This is known as a Type-I error. However, in general, there can be multiple, or even an infinite number of such regions in data space. Moreover, this criterion does not let us say anything about the signal + background hypothesis. Thus, we also require that the choice of the signal region leads to a low probability (denoted  $\beta$ ) of wrongly accepting the background-only hypothesis when the signal + background hypothesis is true (a Type-II error).

In the language of hypothesis testing, then, the job of a collider phenomenologist like myself is to find regions of data space that *minimize* the probability of wrongly accepting the null hypothesis when the alternate hypothesis is true, given a *fixed* probability of wrongly rejecting the null hypothesis when the alternate hypothesis is true.

Whew, that is a mouthful! In more concise terms, we would like to minimize  $\beta$  for a given value of  $\alpha$ . The quantity  $\alpha$  is known as the *size* of the test, and the quantity  $1 - \beta$  is known as the *power* of the test. And more importantly, in practical terms, this task boils down to finding regions of the data space that are densely populated by signal events (minimizing  $\beta$ ) and sparsely populated by background events (minimizing  $\alpha$ ). After isolating a promising signal region, we calculate the maximum achievable value of  $Z$ . In general, the value of  $Z$  will be calculated differently for claiming exclusion or discovery. However, we are not performing a full collider analysis, but rather a sort of ‘feasibility study’, for which we simply use the asymptotic formula for  $Z$  obtained by taking limit in which the probability distributions are Gaussian, and the signal rates are much smaller than the background rates.

$$Z \approx \frac{n_S}{\sqrt{n_B}}$$

where  $n_S$  and  $n_B$  are the number of signal and background events observed in the signal region respectively.

Traditionally, promising signal regions are found by formulating kinematic variables that can efficiently discriminate between signal and background events. These variables are designed based on our knowledge of the kinematics of the final state particles in the signal and background events. They include variables such as invariant mass, missing transverse energy, and transverse mass. While this approach has served us well so far, the models being examined are growing increasingly complex, with large parameter spaces. Also, with the increase in collision energy comes a much larger rate of background event production. Thus, the boundary of the optimal signal region in data space can potentially be highly nonlinear. The traditional ‘cut-and-count’ strategy finds the signal region by applying a series of one or two dimensional selection cuts on the data. This approach can potentially miss higher-dimensional correlations in the data space. However, these correlations can be found efficiently through the use of *machine learning* techniques, which we discuss in [section 3.4](#).

*Reach in parameter space.* As mentioned earlier, new physics theories can have extremely large parameter spaces. Each point of a theory’s parameter space can be interpreted as a hypothesis. In our analyses, we perform hypothesis tests for a large number of points in parameter space, and ascertain which of them can be rejected - or alternatively, discovered. Doing this, we find contours of the the equivalent Z-values in the parameter space. Typically we show only the contours for  $Z = 1.96$  and  $Z = 5$ , that is, the discovery and exclusion contours. We term the area bounded by these contours the *reach* of our analysis in parameter space.

### 3.4 Machine learning in particle physics

In the language of machine learning, discriminating between signal and background events is a *classification* problem. One can consider particle collision events as residing in a space, where the coordinates of each event are represented by various *features* of the event. This ‘feature space’ is equivalent to the ‘data space’ discussed in the previous section. These features could be high-level ones such as invariant masses, or low-level ones, such as the momentum components of individual final state particles. What we do when we perform a cut-and-count analysis is to try and isolate a region of this space that is rich in signal events. Typically, the most straightforward approach is to define a sort of ‘box’ in feature space using rectangular, one-dimensional cuts. However, there is no guarantee that signal events are confined to such a box — correlations between the features can distort the distribution of events in feature space. If we consider a two or three dimensional feature space, this distribution of the events is typically easy to visualize, and can often be

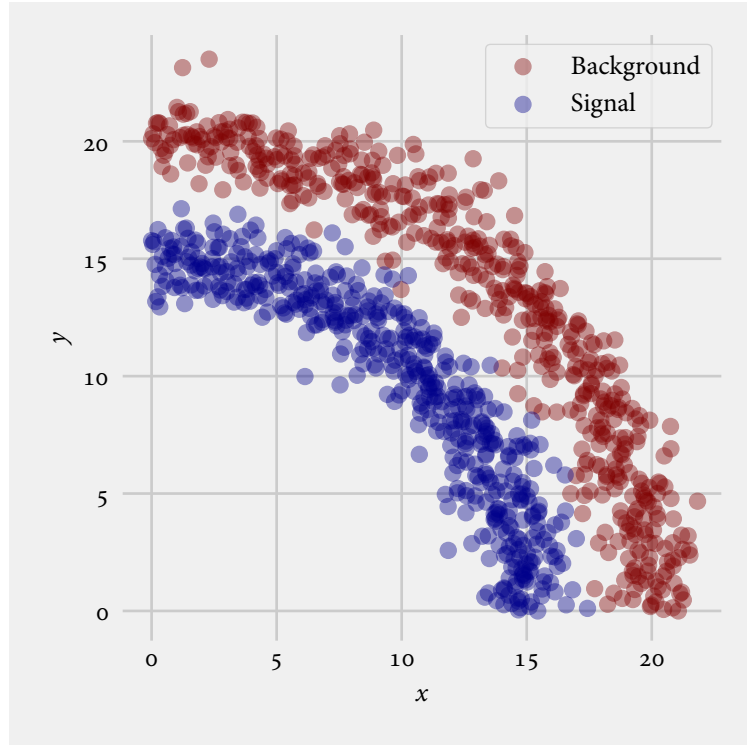


**Figure 3.2:** Illustration of a non-linear decision boundary in two-dimensional feature space.

explained through a simple kinematical relation between the features. Thus, instead of a box, we might draw a ring, or perhaps some other shape as a ‘lasso’ around the events. This kind of delineation between signal and background events is known in machine learning terms as a *decision boundary*. As we go to higher dimensional feature spaces, choosing this decision boundary by visual inspection becomes virtually impossible - instead, we resort to looking at one and two dimensional slices of the space.

However, inspecting these lower dimensional slices may fail to fully capture the potentially complicated correlations among the features, and we might end up rejecting too many signal events, or accepting too many background events. Take for example the distribution of data from a toy experiment in [figure 3.2](#). The decision boundary that separates the signal events (blue) and the background events (red) is curved. Applying rectilinear cuts in this feature space would clearly be suboptimal. Machine learning (ML) techniques (or, as they are sometimes referred to in the particle physics literature, multivariate techniques) can harness the correlations between features more efficiently than manually attempting to find the optimal decision boundary in feature space.

In the context of particle physics, a *binary classifier* is a function that takes as input various features of an event, and outputs a score for the event corresponding to whether it is more signal-like or more background-like. The form of the function itself depends on a number of parameters, which are *a priori* unknown. In *supervised learning* (which

encompasses the most commonly-used ML techniques), these parameters are set by feeding the classifier a set of *labeled training data*. After the parameters are determined through a minimization procedure, we can evaluate the performance of the classifier by using it on *test data*, which are unlabeled. While there are a number of commonly-used classifiers to choose from, for our study, we chose the Gradient Boosted Decision Tree classifier<sup>3</sup>, since it performs quite well ‘out-of-the-box’, with minimal tuning. This classifier is actually an example of an *ensemble method* — it combines the scores from a large number of weak classifiers to assign final scores to events. This combination is much more resistant to *over-training*, that is, the resulting classifier will not be too specialized to the training set and can perform well on general data sets as well. While the analysis in [chapter 4](#) does not employ ML techniques, the analyses in chapters [5](#) and [6](#) do.

<sup>3</sup>For a description of this classifier and a good review of statistical learning in general, see [[28](#)].



# 4

## LIGHT CHARGED HIGGSES AT THE LHC

In section 2.2, we introduced a well-motivated class of models that serve as a framework for analyzing extended scalar sectors, known as Two-Higgs Doublet Models (2HDMs). In these models, the mass spectrum of the scalar sector consists of two CP-even Higgses  $h$  and  $H^1$ , a CP-odd Higgs  $A$ , and a charged Higgs  $H^\pm$ .

The discovery of one or more of these new particles would be a clear indication of an extended scalar sector, which can have important implications for electroweak symmetry breaking (EWSB). A number of experimental searches have been carried out to find these particles at the Large Electron-Positron Collider (LEP), the Tevatron experiment at Fermilab, and most recently, the LHC [29–36]. These searches have been performed assuming that the new scalar states decay solely through conventional channels, that is, into SM particles. However, if they are kinematically allowed, ‘exotic’ decay channels, in which a heavy Higgs boson decays into either a pair of lighter Higgses, or a Higgs and a gauge boson, can be the dominant decay channels in certain regions of parameter space, thus reducing the reach of the conventional search channels. Some of these channels have already been studied both theoretically [37–45] and experimentally [46–48]. With the increase in center of mass collision energy of the LHC from 7 to 14 TeV, more of those exotic decay channels will become accessible at the LHC. It is therefore timely to study their reach more carefully.

In this study, we examine the prospects of detecting a light (that is, lighter than the top quark) charged Higgs boson that decays through the exotic decay channel

$$H^\pm \rightarrow (A/H)W^\pm \rightarrow (\tau\tau)W^\pm$$

and is produced via the decay of the top quark,  $t \rightarrow H^+ b$ . The collider analysis in [40] studies the same exotic decay channel, but for a charged Higgs heavier than the top quark, produced in  $H^\pm tb$  associated production. The large rate of production of top quarks at the LHC should enable us to observe a sizable number of signal events. Current search strategies for light charged Higgses at the LHC assume that they decay either leptonically to the  $\tau\nu$  final state, or hadronically to the  $cs$  final state. The null search results obtained by both the ATLAS and CMS experiments exclude a light charged Higgs below a mass of about 160 GeV for most of the two-dimensional  $m_{H^\pm} - t_\beta$  plane<sup>2</sup> in parameter space [32, 33]. However, if there exists a neutral Higgs ( $A/H$ ) light enough that the  $H^\pm \rightarrow AW^\pm/HW^\pm$  channel is kinematically open, the branching ratios into the conventional final states  $\tau\nu$  and  $cs$  are suppressed and the exclusion bounds can be significantly weakened. Due to experimental challenges at low energies, such a light neutral Higgs has not been fully excluded yet. A relatively large region of  $m_H^\pm > 150$  GeV and  $t_\beta \lesssim 20$  is

<sup>1</sup>Note that we use  $h$  and  $H$  to refer to the lighter or the heavier CP-even Higgs for models with two CP-even Higgs bosons. When there is no need to specify, we use  $H$  to refer to the CP-even Higgses.

<sup>2</sup>Here we use the abbreviated notations for trigonometric functions introduced in section 2.2

still allowed, while no limits exist for  $m_H^\pm > 160$  GeV.

The exotic decay channel of  $H^\pm \rightarrow AW/HW$ , on the other hand, offers an additional opportunity for the detection of a light charged Higgs and closes the loophole of the current light charged Higgs searches. While there are strong constraints on the mass of the light charged Higgs from flavor [49, 50] and precision [51–55] observables, they are typically model dependent and could be relaxed when there are contributions from the other sectors of the model [56]. A direct search for a light charged Higgs, on the other hand, provides model-independent limits. It is thus worthwhile to fully explore the discovery and exclusion potential for the light charged Higgs at the LHC.

The rest of the chapter is structured as follows. In [section 4.1](#), we briefly introduce the relevant couplings and branching ratios for our decay channel for the type II 2HDM and highlight scenarios that permit a large branching ratio for the process  $H^\pm \rightarrow AW/HW$ . In [section 4.2](#), we summarize the current experimental constraints on a light charged Higgs. In [section 4.3](#), we present the details of our collider analysis, and in [section 4.3](#), the model independent exclusion and discovery limits for the 14 TeV LHC with various luminosities. In [section 4.4](#), we discuss the implications of our analysis for the Type II 2HDM and translate our results into reaches in parameter space. We conclude in [section 4.5](#).

## 4.1 Couplings and branching ratios

### *Decays of the top quark*

If the charged Higgs is light enough, the top quark decays primarily to the final states  $W^\pm b$  or to  $H^\pm b$ . The first decay is controlled by the SM gauge coupling

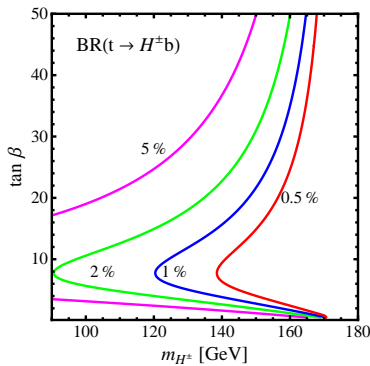
$$g_{W^\pm tb} = \frac{g}{\sqrt{2}} \gamma^\mu \frac{1 - \gamma_5}{2}, \quad (4.1)$$

where  $g$  is the SM  $SU(2)$  coupling. The second is a function of the parameter  $t_\beta$  (see [section 2.2](#) for details). More specifically, for a Type II 2HDM, it takes the form (see [table 2.4](#))

$$g_{H^\pm tb} = \frac{g}{2\sqrt{2}m_W} [(m_b t_\beta + m_t/t_\beta) \pm (m_b t_\beta - m_t/t_\beta) \gamma_5]. \quad (4.2)$$

This coupling is enhanced for both small and large values of  $t_\beta$ . In [figure 4.1](#), we present contours of the branching ratio  $\text{BR}(t \rightarrow H^\pm b)$  in the  $m_{H^\pm} - t_\beta$  plane, calculated using the Two-Higgs Doublet Model Calculator (2HDMC) [57]. We see that it can reach values of 5% and above for both large and small values of  $t_\beta$ , but reaches a minimum at  $t_\beta = \sqrt{m_t/m_b} \sim 8$ . It also decreases rapidly as the charged Higgs mass approaches the mass of the top quark.

**Figure 4.1:** Contours of the branching ratio of the top quark to the charged Higgs, in the  $m_{H^\pm} - t_\beta$  plane.



We see that the branching ratio reaches a minimum at  $t_\beta = \sqrt{m_t/m_b} \approx 8$ .

### Decays of the charged Higgs

Conventionally, a light charged Higgs is assumed to either decay into the  $\tau\nu$  or  $cs$  final states, with the corresponding couplings given by

$$g_{H^\pm\tau\nu} = \frac{g}{2\sqrt{2}m_W} m_\tau t_\beta (1 \pm \gamma_5) \text{ and}$$

$$g_{H^\pm cs} = \frac{g}{2\sqrt{2}m_W} [(m_s t_\beta + m_c/t_\beta) \pm (m_s t_\beta - m_c/t_\beta) \gamma_5].$$

If there exists an additional neutral Higgs boson  $h$  or  $A$  that is lighter than the charged Higgs, then additional decay channels into  $hW/AW$  open up. The relevant couplings are determined by the gauge structure, as well as the mixing angles  $\alpha$  and  $\beta$ , taking the forms [58]

$$g_{H^\pm h W^\mp} = \frac{gc_{\beta-\alpha}}{2} (p_h - p_{H^\pm})^\mu \quad \text{and} \quad g_{H^\pm AW^\mp} = \frac{g}{2} (p_A - p_{H^\pm})^\mu,$$

where  $p_X^\mu$  is the incoming momentum for the corresponding particle  $X$ .

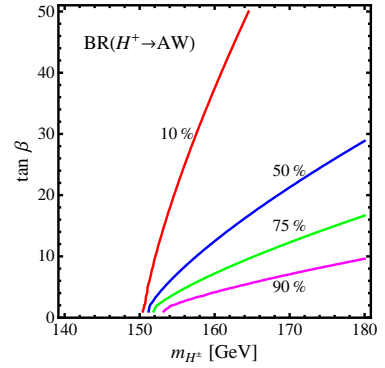
The  $H^\pm \rightarrow hW$  channel for a light charged Higgs is open only if we demand the heavy CP-even neutral Higgs  $H$  to be the SM-like Higgs. In this case  $|c_{\beta-\alpha}| \sim 1$  is preferred by experiments and the  $H^\pm h W^\mp$  coupling is unsuppressed. The  $H^\pm AW^\mp$  coupling is independent of  $c_{\beta-\alpha}$  and always unsuppressed. In this scenario, the  $H^\pm \rightarrow HW$  channel is kinematically forbidden.

In the generic 2HDM, there are no mass relations between the charged scalars, the scalar and pseudoscalar states. Therefore, both the decays  $H^\pm \rightarrow hW$  and  $H^\pm \rightarrow AW$  can be accessible or even dominant in certain regions of the parameter space. It was shown in [50] that in the Type II 2HDM with  $Z_2$  symmetry, imposing all experimental and theoretical constraints still leaves large regions in the parameter space that permit such exotic decays with unsuppressed decay branching ratios.

In figure 4.2, we show the contours of the branching ratio of the charged Higgs to the  $AW$  final state in the  $m_{H^\pm} - t_\beta$  plane, with  $h$  being the SM-like Higgs and  $H$  being heavy enough to be decoupled. This branching ratio reaches large values for  $t_\beta$  between 10 and 30 and charged Higgs masses between 155 and 170 GeV. For small charged Higgs masses close to the  $m_A + m_W$  threshold, the decay is kinematically suppressed. In figure 4.3, we show the same branching ratio, but this time as a function of  $t_\beta$ , for a fixed charged Higgs mass of 160 GeV. For small values of  $t_\beta$ , the branching ratio of the  $AW$  mode dominates that of the  $\tau\nu$  mode. In both plots, we assume the existence of a pseudoscalar  $A$  with a mass of 70 GeV. Similar results can be obtained for  $H^\pm \rightarrow hW$  with  $m_h = 70$  GeV,  $s_{\beta-\alpha} \sim 0$  and  $A$  decoupled.

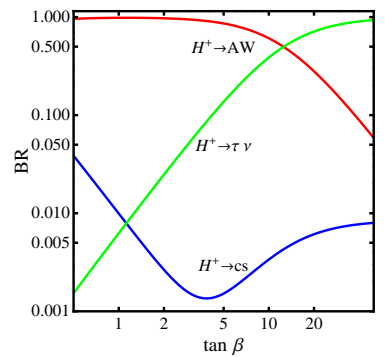
The MSSM Higgs mass spectrum is more restricted than that of a generic 2HDM. At tree level, the mass matrix depends only on  $m_A$  and  $t_\beta$ , and the mass of the charged Higgs mass is related to that of the pseudoscalar  $A$  by the constraint  $m_{H^\pm}^2 = m_A^2 + m_W^2$ . Large loop corrections are therefore needed to increase the mass splitting enough

**Figure 4.2:** Contours of the branching ratio for the decay ( $H^\pm \rightarrow AW$ ) in the Type II 2HDM in  $m_{H^\pm} - t_\beta$  plane.



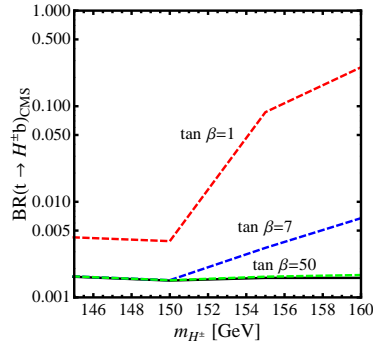
The branching ratio reaches large values for  $t_\beta$  between 10 and 30, for  $m_{H^\pm}$ .

**Figure 4.3:** The branching ratios of  $H^\pm \rightarrow AW$  (red),  $\tau\nu$  (green) and  $cs$  (blue) as functions of  $t_\beta$  for  $m_{H^\pm} = 160$  GeV.



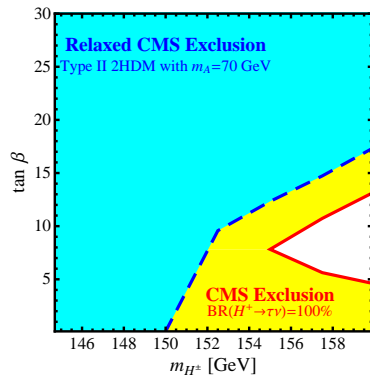
The branching ratio  $BR(H^\pm \rightarrow AW)$  dominates the branching ratios to  $\tau\nu$  and  $cs$  at low values of  $t_\beta$ .

**Figure 4.4:** Weakened CMS limits on the branching ratio of the top quark to the charged Higgs.



Here, we show the limit assuming a  $\text{BR}(H^\pm \rightarrow \tau\nu) = 100\%$  (black line) [33], as well as the weakened limits (green, blue, and red lines) in the Type II 2HDM in the presence of a light neutral Higgs for various values of  $t_\beta$ .

**Figure 4.5:** Weakening of the CMS exclusion limits in the  $m_{H^\pm} - t_\beta$  plane.



The combined yellow and cyan regions show the region excluded by CMS in the  $m_{H^\pm} - t_\beta$  plane assuming a  $\text{BR}(H^\pm \rightarrow \tau\nu) = 100\%$ . The weakened limits with a light neutral Higgs correspond to the cyan region.

to kinematically permit the decay  $H^\pm \rightarrow AW$ . In the non-decoupling region of the MSSM with  $H$  being the SM-like Higgs, the CP-even Higgs  $h$  can be light:  $m_h < m_{H^\pm} - m_W$ . The branching ratios can reach values up to 10% [59] in some regions of parameter space. In the NMSSM, where the Higgs sector is enlarged by an additional singlet, the decays  $H^\pm \rightarrow A_i W/H_i W$  can be significant in certain regions of parameter space [60, 61].

## 4.2 Literature review

Searches for a light charged Higgs boson have been performed by both ATLAS and CMS. The production mechanism considered is top pair production, with one top quark decaying to  $bH^\pm$  while the other decays to  $bW^\pm$ . These studies focus on the  $H^\pm \rightarrow \tau\nu$  decay channel, which is dominant in most regions of the parameter space in the absence of decays into lighter Higgses. Assuming that  $\text{BR}(H^\pm \rightarrow \tau\nu) = 100\%$ , the null search results from CMS [33] imply upper bounds on the top quark branching ratio  $\text{BR}(t \rightarrow H^\pm b)$  ranging from 1.2% to 0.16% for charged Higgs masses between 80 and 160 GeV. This result can be translated into bounds on the MSSM parameter space. The obtained exclusion limits for the MSSM  $m_h^{\max}$  scenario can be seen in figure 4.5 (region to the left of the red line). Only charged Higgs masses in the small region between 155 and 160 GeV around  $t_\beta = 8$  are still allowed. The results from ATLAS [32] are similar. A search with the  $H^\pm \rightarrow cs$  decay channel has been performed by ATLAS [34] using  $4.7 \text{ fb}^{-1}$  of integrated luminosity at 7 TeV and by CMS [35] using  $19.7 \text{ fb}^{-1}$  of integrated luminosity at 8 TeV. Assuming  $\text{BR}(H^\pm \rightarrow cs) = 100\%$ , the ATLAS results imply upper bounds on  $\text{BR}(t \rightarrow bH^\pm)$  between 5% to 1% for charged Higgs masses between 90 and 150 GeV, while the CMS searches imply upper bounds between 2% to 7% for charged Higgs masses between 90 and 160 GeV.

These limits get weaker once we consider realistic branching ratios smaller than 100%. In figure 4.4, we show how the CMS limits on the branching ratio  $\text{BR}(t \rightarrow H^\pm b)$  can change significantly in the presence of an additional light neutral Higgs. The black curve shows the CMS limits presented in [33] assuming a  $\text{BR}(H^\pm \rightarrow \tau\nu) = 100\%$ . The modified limits assuming the existence of a 70 GeV CP-odd neutral Higgs are shown for  $t_\beta = 1$  (red), 7 (blue) and 50 (green). We can see that for large values of  $t_\beta$ , the limits stay almost unchanged, since  $H^\pm \rightarrow \tau\nu$  is the dominant decay channel. However, for smaller values of  $t_\beta$  these limits are weakened significantly.

Similarly, figure 4.5 shows how the CMS limits in the  $m_{H^\pm} - t_\beta$  plane weaken in the presence of an additional light Higgs. The union of the yellow and cyan regions is excluded by CMS assuming  $\text{BR}(H^\pm \rightarrow \tau\nu) = 100\%$ , while only the cyan region is excluded assuming the branching ratios predicted by a Type II 2HDM in the presence of a CP-odd neutral Higgs with a mass of 70 GeV. This weakening is most prominent in the low  $t_\beta$  region - the lower limit on charged Higgs masses reduces

to about 150 GeV for  $t_\beta < 15$ . Therefore, the presence of exotic decay modes substantially weakens the current and projected future limits from searches based on the conventional  $H^\pm \rightarrow \tau\nu, cs$  decay modes.

A light charged Higgs could have a large impact on precision and flavor observables as well [62]. For example, the bounds on the rate of the decay  $b \rightarrow s\gamma$  restrict the charged Higgs to be heavier than 300 GeV for a Type II 2HDM. A detailed analysis of precision and flavor bounds on 2HDMs can be found in [49, 50]. Flavor constraints on the Higgs sector are however typically model-dependent, and could be alleviated by contributions from other new particles in a particular model [56]. Since our focus in this work is on collider phenomenology, we consider light charged Higgses that satisfy the direct bounds set by collider searches for Higgs bosons.

Our study also assumes the existence of a light neutral Higgs  $A/H$ . This type of Higgs has been constrained by the  $A/H \rightarrow \tau\tau$  searches at the LHC [30, 31], in particular, for  $m_{A/H} > 90$  GeV and relatively large values of  $t_\beta$ . No limit, however, exists for  $m_{A/H} < 90$  GeV due to the difficulties in the identification of the relatively soft taus and the overwhelming SM backgrounds for soft leptons and  $\tau$ -jets. Furthermore, LEP limits [29] based on  $VH$  associated production do not apply to the CP-odd  $A$  or the non-SM like CP-even Higgs. The LEP limits based on  $AH$  pair production also do not apply, as long as  $m_A + m_H > 208$  GeV. Therefore, in our analyses, we choose the daughter (neutral) Higgs mass to be 70 GeV<sup>3</sup>.

There have been other theoretical studies on light charged Higgses as well - the authors of [63] and [64] analyze light charged Higgses produced via single top production and decaying to the  $\tau\nu$  final state, while the authors of [65] and [66] investigate light charged Higgses that are produced via the top pair production channel and decay to the  $\mu\nu$  and  $\gamma\gamma W$  final states.

Charged Higgses heavier than the top quark have been analyzed in detail in [40], which considers the associated production channel  $H^\pm tb$  and the exotic decay channel  $H^\pm \rightarrow AW/HW^\pm$ . Given that our study considers the same final state  $bbWW(A/H)$  as the one in [40], we can use a similar search strategy to find light charged Higgses that come from the decay of pair-produced top quarks.

### 4.3 Collider analysis

In our analysis we study the exotic decay  $H^\pm \rightarrow (A/H)W$  of light charged Higgs bosons ( $m_{H^\pm} < m_t$ ) produced via top decay. We consider two production mechanisms for the parent top quarks:  $t$ -channel single top production<sup>4</sup> ( $tj$ ) and top pair production ( $t\bar{t}$ ) [67].

The light neutral Higgs boson can either be the CP-even  $H$  or the CP-odd  $A$ . In the analysis that follows, we use the decay  $H^\pm \rightarrow AW^\pm$  as an illustration. Since we do not use angular correlations of the charged

<sup>3</sup>The mass of 70 GeV is also chosen to be less than half the mass of the SM Higgs (126 GeV). This prohibits the decay channel  $h_{\text{SM}} \rightarrow AA$  and enforces consistency with the current measurements of branching ratios of the SM Higgs.

<sup>4</sup>We only consider the dominant  $t$ -channel single top mode since the  $s$ -channel mode suffers from a very small production rate and the  $tW$  mode has a final state similar to that of the top pair production case.

Higgs decay, the bounds obtained for the  $H^\pm \rightarrow AW^\pm$  channel will apply to the  $H^\pm \rightarrow HW^\pm$  channel as well.

The neutral Higgs boson  $A$  itself will decay further. In this analysis we look at the decay  $A \rightarrow \tau\tau$  for single top production and both the  $\tau\tau$  and the  $bb$  modes for top pair production. While the  $bb$  mode has the advantage of a large branching ratio, the  $\tau\tau$  case has smaller SM backgrounds and therefore leads to a cleaner signal. We study both leptonic ( $\tau_{\text{lep}}$ ) and hadronic ( $\tau_{\text{had}}$ ) decays of the tau lepton, and consider the following combinations of  $\tau$  decays:  $\tau_{\text{had}}\tau_{\text{had}}$ ,  $\tau_{\text{lep}}\tau_{\text{had}}$  and  $\tau_{\text{lep}}\tau_{\text{lep}}$ . The  $\tau_{\text{lep}}\tau_{\text{had}}$  case is particularly promising since we can utilize a same sign dilepton signal with the leptons from the decays of the  $W$  and the  $\tau$ .

We use Madgraph 5/MadEvent v1.5.11 [22] to generate our signal and background events. These events are passed to Pythia v2.1.21 [23] to simulate initial and final state radiation, showering and hadronization. The events are further passed through Delphes 3.07 [25] with the Snowmass combined LHC detector card [68] to simulate detector effects. The discovery reach and exclusion bounds have been determined using RooStats [69] and theta-auto [70].

In this section, we will present model-*independent* exclusion and discovery limits on  $\sigma \times \text{BR}$  for both single top and top pair production with the final states  $\tau\tau bWj$  and  $\tau\tau bbWW/bbbbWW$ . We consider parent charged Higgses with masses between 150 and 170 GeV and a daughter Higgs  $A$  with a mass of 70 GeV.

### *Single Top Production*

For single top production, we consider the channel

$$pp \rightarrow t j \rightarrow H^\pm b j \rightarrow AW^\pm b j \rightarrow \tau\tau Wbj.$$

The dominant SM backgrounds are  $W\tau\tau$  production, which we generate with up to two additional jets (including  $b$  jets), and top pair production with both fully leptonic and semileptonic decay chains, which we generate with up to one additional jet. We also take into account the SM backgrounds  $tj\tau\tau$  and  $tlll$  with  $l = (e, \mu, \tau)$ . Our approach is to perform a traditional ‘cut-and-count’ analysis, with the following selection cuts.

#### 1. Identification cuts:

- *Case A* ( $\tau_{\text{had}}\tau_{\text{had}}$ ): We select events with exactly one lepton ( $e$  or  $\mu$ ), two  $\tau$  tagged jets, fewer than two  $b$  tagged jets, and at least one untagged jet. We also require the  $\tau$ -tagged jets to have opposite-sign charges.
- *Case B* ( $\tau_{\text{lep}}\tau_{\text{had}}$ ): Same as case A, except that we require exactly two leptons instead of one. Additionally, we require that both of these leptons have charges of the same sign, which is opposite to the sign of the  $\tau$  tagged jet.

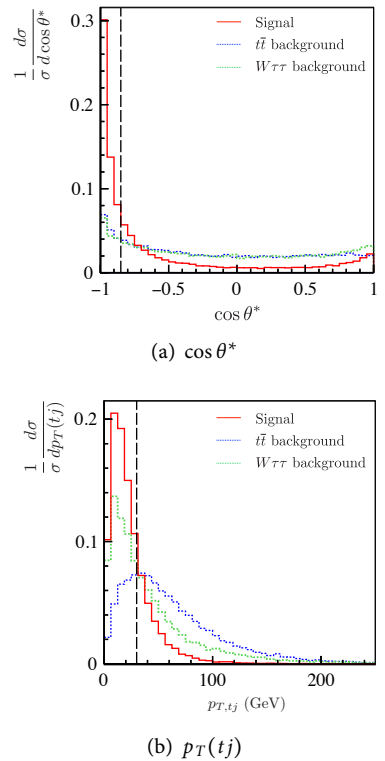
- *Case C* ( $\tau_{\text{lep}} \tau_{\text{lep}}$ ): Same as case A, except that we require exactly three leptons instead of one. No constraints are placed on the signs of the charges for this case.

The following criteria were also required for the identification of leptons, and jets:  $|\eta_{l,b,\tau}| < 2.5$ ,  $|\eta_j| < 5$ ,  $p_T(l_1, j, b) > 20$  GeV and  $p_T(l_2) > 10$  GeV.

2. *Neutrino reconstruction*: We reconstruct the momentum of the neutrino using the missing transverse momentum and the momentum of the hardest lepton as described in [71], assuming that the missing energy is solely from the decay  $W \rightarrow l\nu$ .
3. *Neutral Higgs candidate*: The  $\tau$  jets (case A), the  $\tau$  jet and the softer lepton (case B) or the two softer leptons (case C) are combined to form the neutral Higgs candidate. The reconstruction of the neutrino and the neutral Higgs candidate are relatively poor in cases B and C due to additional missing energy from the neutrino associated with the leptonic  $\tau$  decay.
4. *Charged Higgs candidate*: The momenta of the neutral Higgs candidate, the reconstructed neutrino and the hardest lepton are combined to form the charged Higgs candidate.
5. *Mass cuts*: We place upper limits on the masses of the charged and neutral Higgs candidates, optimized for each mass combination. For  $m_{H^\pm} = 160$  GeV and  $m_A = 70$  GeV, we impose the cuts  $m_{\tau\tau} < 48$  GeV, and  $m_{\tau\tau W} < 148$  GeV.
6. *Angular correlation*: The angle  $\theta^*$  between the momentum of the top quark in the  $tj$  system's rest frame and the momentum of the  $tj$  system in the lab frame acts as a unique kinematical signature of single top production [72]. The differential distribution for  $\cos \theta^*$  is shown in figure 4.6(a) for the signal (red), and the backgrounds  $t\bar{t}$  (blue) and  $W\tau\tau$  (green). The signal distribution tends to peak around  $\cos \theta^* \approx -1$  while the background distributions are flat. If the top quark could be reliably identified, the  $\cos \theta^*$  distribution for the  $t\bar{t}$  background would peak around  $\cos \theta^* = 1$ , as shown in [72]. However, in this study we approximate the top quark momentum by the momentum of the charged Higgs candidate, which results in a flat distribution of  $\cos \theta^*$  for the  $t\bar{t}$  system. In our analysis we require  $\cos \theta^* < -0.8$ .
7. *Top and recoil jet system momentum*: In single top production, we expect that the transverse momentum of the top quark and recoil jet should balance each other, as shown in figure 4.6(b) by the red curve. We require that the transverse momentum of the  $tj$  system,  $p_T(tj)$ , must be less than 30 GeV. This further suppresses the top pair production background in the presence of additional jets coming from the second top quark.

In table 4.1, we show a representative cut flow table for a signal benchmark point with  $m_{H^\pm} = 160$  GeV and  $m_A = 70$  GeV at the 14 TeV LHC. The first row shows the total cross section before cuts, calculated using

**Figure 4.6:** Normalized distributions of  $\cos \theta^*$  (top) and the transverse momentum of the  $tj$  system  $p_T(tj)$  (bottom), for case A with  $m_{H^\pm} = 160$  GeV.



The imposed cuts are indicated by the vertical dashed lines.

**Table 4.1:** Representative cut flow table for the benchmark point with  $m_{H^\pm} = 160$  GeV and  $m_A = 70$  GeV at the 14 TeV LHC. (Single top production)

Case	Cut	$\sigma_{\text{Signal}}$	$\sigma_{W(W)\tau\tau}$	$\sigma_{t\bar{t}}$	$\sigma_{tj\tau\tau/tl\bar{l}}$	$S/B$	$S/\sqrt{B}$
	Original	100	2000	$6.3 \times 10^5$	257	-	-
A	Identification	0.29	5.36	130	1.39	0.002	0.43
	Mass cuts	0.16	0.34	2.62	0.04	0.05	1.55
	$\cos\theta^*$ and $p_{T,tj}$	0.07	0.03	0.07	0.001	0.67	3.72
B	Identification	0.25	4.45	2.46	1.33	0.03	1.51
	Mass cuts	0.11	0.31	0.20	0.05	0.19	2.48
	$\cos\theta^*$ and $p_{T,tj}$	0.06	0.04	0.02	0.002	0.91	3.99
C	Identification	0.18	3.07	6.77	6.74	0.01	0.78
	Mass cuts	0.12	0.55	0.94	0.28	0.07	1.63
	$\cos\theta^*$ and $p_{T,tj}$	0.07	0.08	0.10	0.01	0.38	2.84

All cross sections are given in femtobarns. We have chosen a nominal value for  $\sigma \times \text{BR}(pp \rightarrow tj \rightarrow H^\pm jb \rightarrow \tau\tau Wbj)$  of 100 fb to illustrate the cut efficiencies for the signal process. The significance,  $S/\sqrt{B}$  is calculated for an integrated luminosity of 300  $\text{fb}^{-1}$ .

MadGraph. The following rows show the cross sections for the signal and major backgrounds after applying the selection cuts discussed above. We have chosen a nominal value of 100 fb for  $\sigma \times \text{BR}(pp \rightarrow H^\pm jb \rightarrow \tau\tau Wbj)$  to illustrate the cut efficiencies<sup>5</sup>.

We can see that the dominant backgrounds after particle identification are  $t\bar{t}$  for cases A and C, and  $W\tau\tau$  for case B. The reach is slightly better in case B since the same sign dilepton signature can efficiently reduce the  $t\bar{t}$  background. Nevertheless, soft leptons from underlying events or  $b$ -decay can mimic the same sign dilepton signal. The obtained results are sensitive to the  $\tau$  tagging efficiency as well as the misidentification rate. In our analyses, we have used a  $\tau$  tagging efficiency of 60% and a mistagging rate of 0.4%, as suggested in [68]. A better rejection of non- $\tau$  initiated jets would increase the significance of this channel.

### Top Pair Production

We now turn to the top pair production channel,

$$pp \rightarrow tt \rightarrow H^\pm tb \rightarrow AbbWW \rightarrow \tau\tau bbWW/bbbbWW. \quad (4.3)$$

As mentioned earlier, a detailed collider study with the same final states has been performed in [40] with a focus on high charged Higgs masses. We adopt the same strategy for the light charged Higgs case and refer to [40] for the details of the analysis.

To analyze this channel, we consider the same decay modes for the neutral Higgs as we did for the single top production case:  $\tau_{\text{had}}\tau_{\text{had}}$ ,  $\tau_{\text{had}}\tau_{\text{lep}}$ ,  $\tau_{\text{lep}}\tau_{\text{lep}}$ , along with the additional mode  $A \rightarrow bb$ . We require that one of the two  $W$  bosons from the decays of the charged Higgses

<sup>5</sup>This is consistent with the branching ratio of the top quark into a charged Higgs with mass 160 GeV in a Type II 2HDM, which is typically between 0.1% and 1% (see figure 4.1). Using the single top production cross section from [67],  $\sigma_{tj} = 248$  pb, and assuming the branching ratios  $\text{BR}(H^\pm \rightarrow AW^\pm) = 100\%$  and  $\text{BR}(A \rightarrow \tau\tau) = 8.6\%$  leads to the stated  $\sigma \times \text{BR}$  of between 21 and 210 fb.

**Table 4.2:** Representative cut flow table for the same benchmark point as [table 4.1](#) and the decay mode  $A \rightarrow \tau\tau$ . (Top pair production)

Case	Cut	$\sigma_{\text{Signal}}$	$\sigma_{t\bar{t}}$	$\sigma_{t\bar{t}ll}$	$\sigma_{W(W)\tau\tau}$	$S/B$	$S/\sqrt{B}$
Original		1000	$6.3 \times 10^5$	247	2000	-	-
	Identification	4.1	23.3	0.58	0.078	0.17	14.9
A	$m_{\tau\tau}$ vs $m_{\tau\tau W}$	0.6	0.31	0.021	0.003	1.9	18.8
	Identification	3.3	0.35	0.697	0.072	3.0	55.3
B	$m_{\tau\tau}$ vs $m_{\tau\tau W}$	0.69	0.035	0.042	0.007	8.1	41.1
	Identification	3.1	2.35	5.11	0.058	0.41	19.9
C	$m_{\tau\tau}$ vs $m_{\tau\tau W}$	0.62	0.25	0.16	0.006	1.4	16.5

We have chosen a nominal value for  $\sigma \times \text{BR}(pp \rightarrow tt \rightarrow H^\pm tb \rightarrow \tau\tau bbWW)$  of 1000 fb to illustrate the cut efficiencies for the signal process. The significance,  $S/\sqrt{B}$  is calculated for an integrated luminosity of 300 fb $^{-1}$ . See [\[40\]](#) for the details of the selection cuts used.

decay leptonically, and the other hadronically, to strike a balance between reducing backgrounds and keeping a substantial production cross section.

The dominant SM background for the  $\tau\tau$  channel is top pair production with semi and fully leptonic decay chains. We also take into account  $t\bar{t}ll$  production with  $l = (e, \mu, \tau)$ , as well as  $W\tau\tau$  and  $WW\tau\tau$ . We ignored the subdominant backgrounds from single vector boson production,  $WW$ ,  $ZZ$ , single top production, as well as multijet QCD background. Those backgrounds are either small or can be sufficiently suppressed by the cuts imposed. Similar backgrounds are considered for the  $bb$  process.

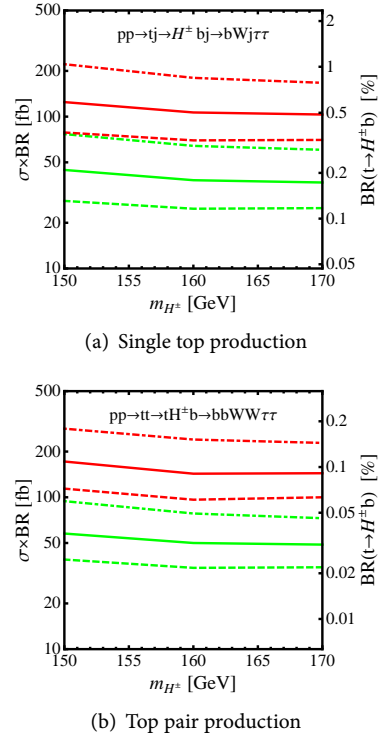
In [table 4.2](#), we show a representative cut flow table for a signal benchmark point with  $m_{H^\pm} = 160$  GeV and  $m_A = 70$  GeV and the decay  $A \rightarrow \tau\tau$  at the 14 TeV LHC, similar to [table 4.1](#). We have chosen a nominal value for  $\sigma \times \text{BR}(pp \rightarrow tt \rightarrow H^\pm tb \rightarrow \tau\tau bbWW)$  of 1000 fb to illustrate the cut efficiencies for the signal process.

After the cuts, the dominant backgrounds are  $t\bar{t}$  (for the  $\tau_{\text{had}}\tau_{\text{lep}}$  cases) as well as  $t\bar{t}ll$  (for the  $\tau_{\text{had}}\tau_{\text{lep}}$  cases). Other backgrounds including vector bosons do not contribute much. Similar to the single top case, we find that the  $\tau_{\text{lep}}\tau_{\text{had}}$  case gives the best reach.

#### Model-independent limits

[Figure 4.7](#) displays the exclusion (green) and discovery (red) limits at the 14 TeV LHC for the single top production and top pair channels, assuming  $\text{BR}(H^\pm \rightarrow AW^\pm) = 100\%$  and  $\text{BR}(A \rightarrow \tau\tau) = 8.6\%$ , and a systematic error of 10%. The dot-dashed, solid and dashed lines show the results for integrated luminosities of 100, 300, and 1000 fb $^{-1}$  respectively. The left vertical axis shows limits on  $\sigma \times \text{BR}$ , and the right vertical axis shows the corresponding limits on  $\text{BR}(t \rightarrow H^\pm b)$ . In these plots, we have combined all three cases of  $\tau$  decays. While in the single top channel,

**Figure 4.7:** Exclusion and discovery limits on  $\sigma \times \text{BR}(t \rightarrow H^\pm b)$



The upper panel represents the single top channel and the lower panel represents the top pair production channel. The vertical axis on the left represents the limit on the quantity  $\sigma \times \text{BR}$ , while the vertical axis on the right represents the corresponding limits on the branching ratio of the top quark to the charged Higgs boson.

cases A, B, and C contribute roughly the same to the overall significance, the sensitivity achieved in case B is substantially greater than in cases A and C in the top pair production channel. Due to the small number of events in both channels, the statistical error dominates over the systematic error in the background cross sections. Therefore, higher luminosities lead to better reaches. Assuming  $300 \text{ fb}^{-1}$  of integrated luminosity, the exclusion limits on  $\sigma \times \text{BR}$  are about 35 and 55 fb for the single top and top pair production processes respectively. The discovery reaches are about three times higher.

<sup>6</sup>Assuming  $bb$  and  $\tau\tau$  are the dominant decay modes of a light  $A$ ,  $\text{BR}(A \rightarrow \tau\tau) = 8.6\%$  in a Type II 2HDM or the MSSM at medium to large  $t_\beta$ . This branching ratio decreases for small  $t_\beta$  when the  $cs$ -channel is enhanced.

Assuming  $\text{BR}(H^\pm \rightarrow AW) = 100\%$  and  $\text{BR}(A \rightarrow \tau\tau) = 8.6\%^6$ , we can reinterpret the limits on  $\sigma \times \text{BR}$  as limits on the  $\text{BR}(t \rightarrow H^\pm b)$ , as indicated by the vertical axes on the right. While the limits on the cross section are better in the single top channel, the corresponding limits on  $\text{BR}(t \rightarrow H^\pm b)$  are weaker due to the smaller cross section for single top production. The lowest achievable upper limits on  $\text{BR}(t \rightarrow H^\pm b)$  are about 0.2% for the single top process and 0.03% for the top pair production process, respectively.

A study of the  $A \rightarrow bb$  decay using the top pair production channel leads to worse results due to the significantly higher SM backgrounds. For the 14 TeV LHC with  $300 \text{ fb}^{-1}$ , the exclusion limit on  $\sigma \times \text{BR}$  is about 7 pb for a charged Higgs with a mass of 160 GeV, assuming the existence of a light neutral Higgs with a mass of 70 GeV. Thus, given the typical ratio

$$\frac{\text{BR}(A/H \rightarrow bb)}{\text{BR}(A/H \rightarrow \tau\tau)} \sim \frac{3m_b^2}{m_\tau^2},$$

we conclude that the reach in the  $bb$  case is much worse than that of the  $\tau\tau$  case.

We reiterate here that the limits on  $\sigma \times \text{BR}$  are completely model independent. Whether or not discovery/exclusion is actually feasible in this channel should be answered within the context of a particular model, in which the theoretically predicted cross sections and branching ratios can be compared with the model-independent limits. We will do this in the following section for a Type II 2HDM.

#### 4.4 Implications for a Type II 2HDM

Two-Higgs Doublet Models allow us to interpret the observed Higgs signal either as the lighter CP-even Higgs ( $h_{-126}$ ) or the heavier CP-even Higgs ( $H_{-126}$ ). The authors of [50] have identified the regions of the parameter space of Type II 2HDMs that survives all the existing experimental and theoretical constraints in both of these cases, assuming  $m_{12}^2 = 0$ . In the  $h_{-126}$  case, we are restricted to either a SM-like region at  $s_{\beta-\alpha} = \pm 1$  with  $t_\beta < 4$  or an extended region with  $0.6 < s_{\beta-\alpha} < 0.9$  and  $1.5 < t_\beta < 4$  with relatively unconstrained masses. In the  $H_{-126}$  case, a SM-like region around  $s_{\beta-\alpha} = 0$  and  $t_\beta < 8$ , and an extended region with  $-0.8 < s_{\beta-\alpha} < 0.05$  and  $t_\beta$  up to 30 or higher, survive all constraints.

We can interpret the results of the previous section in two ways: the light neutral Higgs that the charged Higgs decays to could be either the

Masses (GeV)	Kinematically allowed?		Favored Region
	$H^\pm \rightarrow AW$	$H^\pm \rightarrow hW$	
{ $m_{H^\pm}, m_A, m_h, m_H$ }			
BP1: {160, 70, 126, 700}	Yes	No	$s_{\beta-\alpha} \approx \pm 1$
BP2: {160, 700, 70, 126}	No	Yes	$s_{\beta-\alpha} \approx 0$

**Table 4.3:** Benchmark points used for illustrating the discovery and exclusion limits in the context of the Type II 2HDM. Also shown are the typical favored regions of  $s_{\beta-\alpha}$  for each case (see [50]).

CP-even Higgs  $h$  or the CP-odd Higgs  $A$ . The decay mode  $H^\pm \rightarrow HW$  is not possible given that  $m_H \geq 126$  GeV. The decay  $H^\pm \rightarrow AW$  is possible in both the  $h$ -126 and  $H$ -126 cases and the partial decay width is independent of  $s_{\beta-\alpha}$ . However, the branching ratio does depend on whether the channel  $H^\pm \rightarrow hW$  is open or not. For simplicity, we choose a representative benchmark point BP1, with  $\{m_{H^\pm}, m_A, m_h, m_H\} = \{160, 70, 126, 700\}$  such that only the decay mode  $H^\pm \rightarrow AW$  is kinematically accessible. The decay width  $H^\pm \rightarrow hW$  depends on  $s_{\beta-\alpha}$  and is only sizable in the  $H$ -126 case. We illustrate this case with a second benchmark point, BP2:  $\{m_{H^\pm}, m_A, m_h, m_H\} = \{160, 700, 70, 126\}$ , assuming that the CP-odd Higgs  $A$  decouples. We list the benchmark points in table 4.4.

In figure 4.8, we show the branching fraction  $\text{BR}(H^\pm \rightarrow AW)$  for BP1, which is independent of  $s_{\beta-\alpha}$  and decreases with increasing  $t_\beta$  due to the enhancement of the  $\tau\nu$  mode. The branching ratio can reach values of 90% or larger for small  $t_\beta < 4$  and stays the dominant channel until  $t_\beta = 12$ .

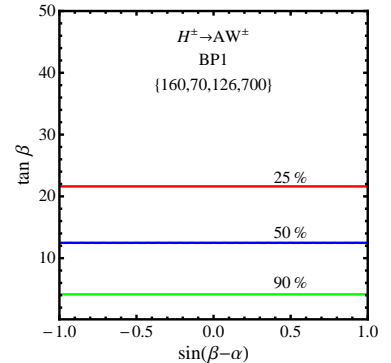
Figure 4.9 shows the branching ratio,  $\text{BR}(H^\pm \rightarrow hW)$ , for BP2. It reaches maximal values around  $s_{\beta-\alpha} = 0$  and decreases for larger  $|s_{\beta-\alpha}|$  compared to BP1 due to the suppressed  $H^\pm hW$  coupling.

In 4.10, we display the regions that can be excluded (yellow regions enclosed by the solid lines as well as the cyan regions) and discovered (cyan regions enclosed by the dashed lines) for BP1 (left panel) and BP2 (right panel) at the 14 TeV LHC with  $300 \text{ fb}^{-1}$  integrated luminosity. The red lines represent the limits from the top pair production channel, and the blue lines represent the limits from the single top production channel.

For the benchmark point BP1 with  $H^\pm \rightarrow AW^\pm$ , the exclusion reach based on top pair production covers the entire parameter space, while discovery is possible for small  $t_\beta < 6$  and large  $t_\beta > 18$ , independent of  $s_{\beta-\alpha}$ . Intermediate values of  $t_\beta$  have a reduced branching ratio  $\text{BR}(t \rightarrow H^\pm b)$  (see figure 4.1) and therefore the total  $\sigma \times \text{BR}$  is suppressed. At high values of  $t_\beta$ ,  $\text{BR}(t \rightarrow H^\pm b)$  is enhanced enough to overcome the reduced branching ratio  $\text{BR}(H^\pm \rightarrow AW)$ . The search based on single top production is only effective in the small  $t_\beta$  region, with an exclusion reach of  $t_\beta < 4$  and a discovery reach of  $t_\beta < 2$ .

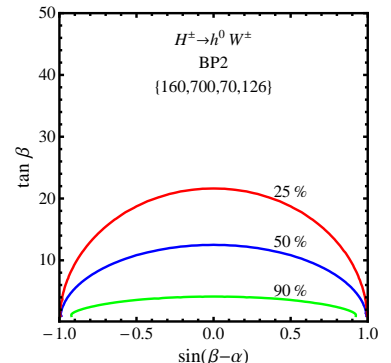
The right panel of 4.10 shows the reach for BP2. The exclusion region for top pair production covers the entire parameter space except for  $|s_{\beta-\alpha}| > 0.85$  and  $t_\beta > 4$ . Discovery is possible for large  $t_\beta > 18$  with  $|s_{\beta-\alpha}| < 0.5$  and for small  $t_\beta < 6$ . The reach from the single top

**Figure 4.8:** Contours of branching ratios for the benchmark point BP1.



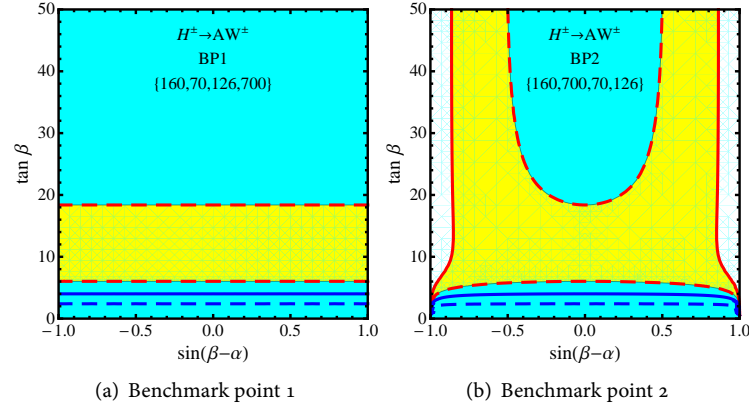
The branching ratio is independent of  $s_{\beta-\alpha}$ , and is dominated by the  $\tau\nu$  mode at high values of  $t_\beta$ . For small  $t_\beta$  less than 12, it is the dominant channel, reaching values of 90% or larger for  $t_\beta < 4$ .

**Figure 4.9:** Contours of branching ratios  $\text{BR}(H^\pm \rightarrow hW^\pm)$  for the benchmark point BP2.



This branching ratio reaches its maximum at  $s_{\beta-\alpha}=0$ , since larger values of  $|s_{\beta-\alpha}|$  lead to the suppression of the  $H^\pm hW^\pm$  coupling.

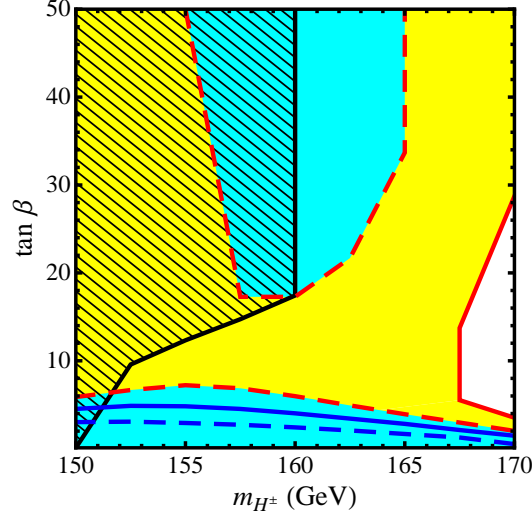
**Figure 4.10:** The exclusion (yellow and cyan regions combined, bounded by dashed lines) and discovery (cyan region only bound by solid lines) reach achievable in the  $t_\beta$  versus  $s_{\beta-\alpha}$  plane for the benchmark points 1 and 2, with an integrated luminosity of  $300 \text{ fb}^{-1}$  at the 14 TeV LHC.



The red lines represent the reach achievable by the top pair production channel, while the blue lines represent the reach achievable by the single top channel.

Erratum: The plot on the right is labeled  $H^\pm \rightarrow AW$ , when it should actually be  $H^\pm \rightarrow hW$ .

**Figure 4.11:** Exclusion (yellow regions bounded by solid lines as well as the cyan regions) and discovery (cyan regions bounded by the dashed lines) imposed by the  $tj$ -channel (blue) and  $tt$ -channel (red) in the  $m_{H^\pm} - t_\beta$  parameter space for  $300 \text{ fb}^{-1}$  luminosity with  $m_A = 70 \text{ GeV}$ . The same limits apply for  $m_h = 70 \text{ GeV}$  and  $s_{\beta-\alpha} = 0$  if  $A$  is decoupled. The black hatched region indicates the region excluded by the CMS search based on  $H^\pm \rightarrow \tau\nu$  [33].



production channel is limited to the small  $t_\beta$  region.

In figure 4.11, we show the reach in the  $m_{H^\pm} - t_\beta$  plane for  $H^\pm \rightarrow AW$  with  $m_A = 70 \text{ GeV}$  with decays of  $H^\pm$  to both  $h$  and  $H$  kinematically disallowed. These limits also apply for  $H^\pm \rightarrow hW$  with  $m_h = 70 \text{ GeV}$  and  $s_{\beta-\alpha} = 0$  with a decoupled  $A$ . We display the exclusion (yellow regions enclosed by the solid lines as well as the cyan regions) and discovery

limits (cyan regions enclosed by the dashed lines) for an integrated luminosity of  $300 \text{ fb}^{-1}$  at the 14 TeV LHC. Superimposed are the current CMS limits (black hatched region) [33] which exclude the large  $t_\beta$  region for  $m_{H^\pm} < 160 \text{ GeV}$ .

The best reach is obtained by the top pair channel (region enclosed by the red lines). Charged Higgs masses can be excluded up to 167 GeV for all values of  $t_\beta$ , and up to 170 GeV for  $t_\beta < 4$  or  $t_\beta > 29$ . Discovery is possible for both low  $t_\beta < 6$  with  $m_{H^\pm}$  between 150 and 170 GeV and high  $t_\beta > 17$  with  $m_{H^\pm}$  between 155 and 165 GeV. The reach is weakened for intermediate values of  $t_\beta$  due to the reduced branching ratio  $\text{BR}(t \rightarrow H^\pm b)$ . The single top channel (region enclosed by the blue lines) only provides sensitivity in the low  $t_\beta$  region, permitting exclusion for  $t_\beta \lesssim 4$  and discovery for  $t_\beta < 3$ .

We conclude this section with the following observations:

- Both the  $H^\pm \rightarrow AW$  channel (for the  $h$ -126 case) and the  $H^\pm \rightarrow hW$  channel (for the  $H$ -126 case) permit exclusion and discovery in large regions of the parameter space.
- While the top pair production channel covers a large region of parameter space, the single top channel permits discovery/exclusion only in the low  $t_\beta$  region.

#### 4.5 Conclusion

After the discovery of the first fundamental scalar by both the ATLAS and CMS collaboration, it is now time to carefully measure its properties to determine its nature. Current measurements still permit the possibility that the discovered signal is not the SM Higgs particle, but just one scalar particle contained in a larger Higgs sector, predicted by many extensions of the SM.

In this work we consider the prospects of discovering a charged Higgs lighter than the top quark, produced via top decay ( $t \rightarrow H^\pm b$ ). Due to the large single top and top pair production cross sections at the LHC, such a charged Higgs can be produced copiously. Assuming that the light charged Higgs predominantly decays into  $\tau\nu$ , both ATLAS and CMS exclude a light charged Higgs for most regions of the MSSM and Type II 2HDM parameter spaces. However, the branching ratio  $\text{BR}(H^\pm \rightarrow \tau\nu)$  can be significantly reduced once the exotic decay channel into a light Higgs ( $H^\pm \rightarrow AW/HW$ ), is open. This weakens the exclusion bounds from the  $\tau\nu$  search, in particular for small and intermediate  $t_\beta$ , leaving the possibility of a light charged Higgs open. This loophole, however, can be closed when we consider the exotic charged Higgs decay channel  $H^\pm \rightarrow AW/HW$ .

Our analysis examines the decay mode  $H^\pm \rightarrow AW/HW$  decay mode assuming that the lighter Higgs  $A/H$  decays into either  $\tau\tau$  or  $bb$ . While the top pair channel benefits from a large production cross section, the single top channel permits a cleaner signal due to its unique kinematic features. Assuming the existence of a light neutral Higgs with a mass of

70 GeV, the model independent exclusion limits on  $\sigma \times \text{BR}$  based on the  $\tau\tau$  channel are approximately 35 fb for the single top channel and 55 fb for the top pair channel. The discovery reaches are about three times higher. Assuming  $\text{BR}(H^\pm \rightarrow AW/HW) = 100\%$  and  $\text{BR}(A/H \rightarrow \tau\tau) = 8.6\%$ , the exclusion limits on  $\text{BR}(t \rightarrow H^+ b)$  are about 0.2% and 0.03% for single top and top pair production, respectively. A significantly worse reach is obtained in the  $bb$  channel.

We discuss the implications of the obtained exclusion and discovery bounds in the context of the Type II 2HDM, focusing on two scenarios: the decay  $H^\pm \rightarrow AW$  with a light  $A$  in the  $h$ -126 case and the decay  $H^\pm \rightarrow hW$  in the  $H$ -126 case. The top pair channel provides the best reach and permits discovery for both large  $t_\beta > 17$  around  $m_{H^\pm} = 160$  GeV and small  $t_\beta < 6$  over the entire mass range, while exclusion is possible in the entire  $t_\beta$  versus  $m_{H^\pm}$  plane except for charged Higgs masses close to the top quark mass threshold. The single top channel is sensitive in the low  $t_\beta$  region and permits discovery for  $t_\beta < 3$ . In particular, the low  $t_\beta$  region is not constrained by searches in  $\tau\nu$  channel, making  $H^\pm \rightarrow AW/hW$  a complementary channel for charged Higgs searches.

While most of the searches for additional Higgs bosons have focused on conventional decay channels, searches using exotic decay channels have started to garner additional interest [37–48]. Studying all of the possibilities for the non-SM Higgs decays will allow us to exploit the full potential of the LHC and future colliders to improve our understanding of the nature of electroweak symmetry breaking.

*Acknowledgments.* We would like to thank Baradhwaj Coleppa for his participation at the beginning of this project. We would also like to thank Peter Loch and Matthew Leone for helpful discussions. This work was supported in part by the Department of Energy under Grant DE-FG02-13ER41976.

# 5

## EXOTIC HIGGS DECAYS AT 14 AND 100 TEV

In the previous chapter, we showed how exotic decay modes can offer an complementary avenue for discovering charged Higgs bosons at the LHC. While that analysis was performed for a single BSM Higgs and a single exotic decay mode, the project that forms the basis of this chapter aims to do something much more ambitious, namely, to perform a comprehensive set of collider analyses for all the exotic decay modes for heavy Higgses in Type II 2HDMs, both at the 14 TeV LHC, as well as a future 100 TeV hadron collider. The structure of this chapter is as follows. In section 5.1, we present the general case for considering large mass splittings among heavy higgses, thus motivating the consideration of exotic Higgs decay channels. We also briefly discuss the physics potential of a future 100 TeV collider and provide a few references. In section 5.2, we summarize the most general decay modes for BSM Higgses as well as benchmark planes corresponding to a set of exotic decay modes that satisfy theoretical and experimental constraints. In section 5.3, we enumerate some of the existing studies in the literature on exotic decays. In section 5.4, we describe the exotic decay modes we have studied so far, and the strategy we used to do so. In section 5.5, we present some of the preliminary results we have obtained. Finally, we conclude in section 5.6 with a summary and discussion of future work.

### 5.1 Exotic Higgs decays: The Big Picture

As pointed out in chapter 4, most experimental analyses aimed at discovering BSM Higgses focus on conventional decay modes to Standard Model Particles. The reason for this is that most studies assume the scenario known as the *decoupling limit*, where the states  $H, A, H^\pm$  are much heavier than the state  $h$ . Decoupling implies the phenomenon of *alignment*, that is,  $h$  is the SM Higgs boson, or equivalently, the angles  $\beta$  and  $\alpha$  satisfy the condition  $\beta - \alpha = \pi/2$  [73]. The limit of decoupling with alignment is an attractive one, since it implies that the undiscovered Higgses are all much heavier than the SM Higgs, accounting for why they have not been found yet. However, in the decoupling limit, the splitting between the squared masses of heavy Higgses is constrained to be small, on the order of  $\sim O(\nu^2)$  [74]. This constraint on the size of the mass splittings implies that decays of heavy Higgses into final states that contain other heavy Higgses will be kinematically disfavored, and thus they will dominantly decay to final states with SM particles instead.

The relation between decoupling and alignment is not bidirectional, though - alignment does not necessarily imply decoupling. In the limit of alignment without decoupling, it is possible to have sizable mass splittings between the heavy Higgses. While this scenario is necessarily less generic than the decoupling limit, it is well worth considering, especially given that large mass splittings are consistent with a strongly first or-

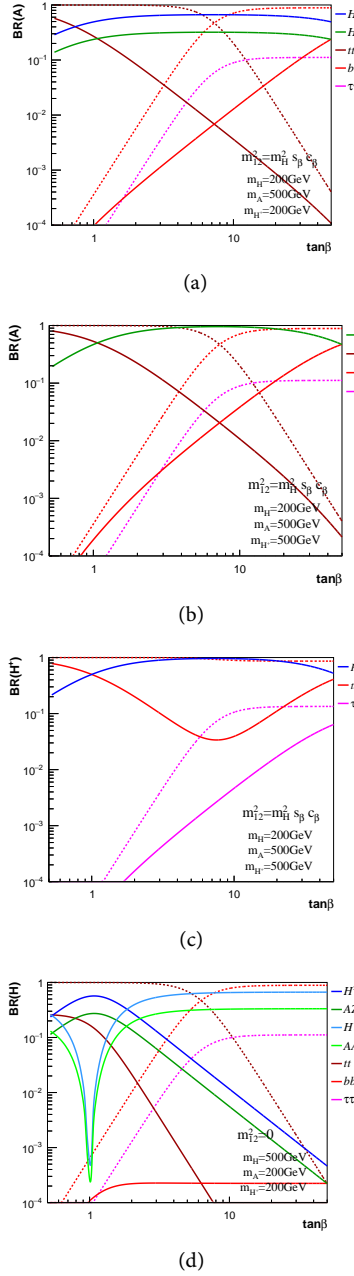


**Figure 5.1:** branching ratios for exotic decays in Type II 2HDMs, as a function of  $t_\beta$ , with  $c_{\beta-\alpha} = 0$ . Source: [4].

der electroweak phase transition [42]. This type of phase transition is necessary for the mechanism of electroweak baryogenesis, which can explain the observed level of baryon asymmetry in the universe. It is also possible to generate such mass splittings away from the alignment limit. While this scenario is experimentally disfavored [75], it has not yet been excluded, and so we study it for completeness.

The presence of large mass splittings opens up the possibility that the heavy Higgses could decay into final states containing other heavy Higgses, that is, they could decay via exotic decay channels. As mentioned when we studied the exotic decay mode  $H^\pm \rightarrow AW$  in chapter 4, in certain regions of parameter space, once the exotic decay modes are allowed, they will dominate the conventional decay modes. This is illustrated in figure 5.1 for a few scenarios. Panels (a) and (b) show the branching ratios for the decays of  $A$ , with  $m_{12}^2 = m_H^2 s_\beta c_\beta$ . Panels (c) and (d) show similar plots, this time for the branching ratios of  $H^\pm$ , with  $m_{12}^2$  equal to  $m_H^2 s_\beta c_\beta$  and 0 respectively. The dashed lines indicate the branching ratios to SM particles in the absence of the exotic decay modes. These channels have begun to garner additional interest in recent years, with the publication of a number of original analyses on the topic [3, 38–42, 76–82].

A 100 TeV collider would open up an immense number of physics opportunities not afforded to a 14 TeV collider [83]. Such a collider would be a natural next step after the LHC, and is being actively discussed in the particle physics community. The two major proposals being considered are the FCC-hh machine by CERN [84], and the SppC by IHEP in China [85]. Executing a project of this size requires an immense amount of planning, over many years. Thus, now is an opportune time to begin to fully explore the physics potential of a 100 TeV collider. There have been a number of studies conducted already, and more are coming out in the literature on a regular basis. We will not attempt to enumerate them all, and instead point the interested reader to the references sections of the review papers [73, 83, 86, 87].

## 5.2 Classifying exotic decays

Taking all the possible combinations of parent and daughter Higgses yields the complete list of exotic decay modes in 2HDMs, shown along with the dominant SM final states in table 5.1.

Given the large number of degrees of freedom in generic 2HDMs, it is important for us to whittle down the number of possible scenarios to a more manageable number by imposing some constraints. The authors of [4] have systematically categorized the scenarios (with differing mass orderings and splittings, values of the parameter  $m_{12}$ , and degrees of deviation from alignment) that are still viable after imposing all the relevant theoretical and experimental constraints. Based on this categorization, they have presented a set of benchmark planes to guide searches

**Table 5.1:** Summary of all the possible exotic decay modes and dominant final states for non-SM Higgs bosons

Parent Higgs	Decay type	Channels in 2HDM	Main Final States
Neutral Higgs $H, A$	$HH$	$H \rightarrow AA, hh$	$(bb/\tau\tau/WW/ZZ/\gamma\gamma)(bb/\tau\tau/WW/ZZ/\gamma\gamma)$
	$HZ$	$H \rightarrow AZ, A \rightarrow HZ, hZ$	$(ll/qq/vv)(bb/\tau\tau/WW/ZZ/\gamma\gamma)$
	$H^+ H^-$	$H \rightarrow H^+ H^-$	$(tb/\tau\nu/cs)(tb/\tau\nu/cs)$
	$H^\pm W^\mp$	$H/A \rightarrow H^\pm W^\mp$	$(lv/qq')(tb/\tau\nu/cs)$
Charged Higgs	$HW^\pm$	$H^\pm \rightarrow hW^\pm/HW^\pm/AW^\pm$	$(lv/qq')(bb/\tau\tau/WW/ZZ/\gamma\gamma)$

Here, we do not take experimental and theoretical constraints into account. In the second column, H refers to any of the neutral Higgs bosons  $h, H$ , and A. Source: [73].

Name	Plane	Decays	$m_{12}^2$
IA	$m_A > m_H = m_{H^\pm}$	$A \rightarrow H^\pm W^\mp$	$m_H^2 s_\beta c_\beta$
		$A \rightarrow HZ$	o
IB	$m_A < m_H = m_{H^\pm}$	$H \rightarrow AZ/AA$	o
		$H^\pm \rightarrow AW^\pm$	
IIA	$m_H > m_A = m_{H^\pm}$	$H \rightarrow AZ/AA$	o
		$H \rightarrow H^+ H^- / H^\pm W^\pm$	
IIB	$m_H < m_A = m_{H^\pm}$	$A \rightarrow HZ$	$m_H^2 s_\beta c_\beta$
		$H^\pm \rightarrow HW^\pm$	o
III	$m_A = m_H = m_{H^\pm}$ vs $c_{\beta-\alpha}$	$A \rightarrow hZ, H^\pm \rightarrow hW^\pm$	$m_H^2 s_\beta c_\beta$
		$H \rightarrow hh$	o

**Table 5.2:** Summary of benchmark planes for exploring exotic Higgs decays in 2HDMs that survive theoretical and experimental constraints. Source: [4].

for new scalars at the LHC via exotic decay modes. These planes are summarized in [table 5.2](#).

Even after this constraining, there remain a plethora of possible final states, as evidenced by the last column of [table 5.1](#). In this work, we aim to answer the questions: which among these final states are the most promising to find new physics, and what are the best strategies to do so at a collider? In the next section, we summarize some of the existing studies on exotic Higgs decays.

### 5.3 Literature review

There are a number of theoretical studies in the literature that examine exotic Higgs decays. We summarize some of the more recent ones. In [39], the exotic decay of a heavy neutral Higgs,  $A/H \rightarrow HZ/AZ$  is studied. The same authors subsequently study the exotic decay of a heavy charged Higgs:  $H^\pm \rightarrow (A/H)W^\pm$ . The prospects of finding a charged Higgs boson lighter than the top quark are examined in [3] (which forms the basis of [chapter 4](#)). The study in [41] examines the exotic decay of a neutral heavy Higgs:  $A/H \rightarrow W^\pm H^\mp$ . Constraints are derived in the  $m_{H^\pm} - t_\beta$  plane for the decay chain  $H \rightarrow H^\pm W^\pm \rightarrow W^+ W^- A$  in [80], while the authors of [79] examine heavy charged Higgses produced in association with a  $W$  boson and decaying into a lighter neutral Higgs.

In [78] the signals for a fermiophobic charged Higgs arising in a 2HDM with right handed neutrinos are examined. Finally, the whitepaper [38] investigates the prospects of discovering a heavy neutral Higgs through the decay  $A/H \rightarrow ZZ/Zh$ , with the  $Z$  decaying leptonically, and the  $h$  decaying to either the  $bb$  or  $\tau\tau$  final states. All of these studies are performed for the 14 TeV LHC.

#### 5.4 Crafting features for our classifier

Preliminary analyses have been carried out for two of the benchmark planes described in [table 5.2](#): benchmark plane IB, with  $m_A < m_H = m_{H^\pm}$ , and benchmark plane IIB,  $m_H < m_A = m_{H^\pm}$ , both assuming  $m_{12}^2 = m_H^2 s_\beta c_\beta$ . For benchmark plane IB, we examine the production and decay chains for the neutral Higgs  $H$ :

$$bb/gg \rightarrow H \rightarrow AZ \rightarrow \tau\tau ll.$$

For benchmark plane IIB, we consider the following production and decay chains for the neutral Higgs  $A$ :

$$bb/gg \rightarrow A \rightarrow HZ \rightarrow \tau\tau ll.$$

In addition, we examine the following production and decay chain for a heavy charged Higgs  $H^\pm$  in benchmark plane IIB:

$$pp \rightarrow tbH^\pm \rightarrow (Wb)b(HW) \rightarrow (Wb)b((\tau\tau)W),$$

where one of the  $W$  bosons decays leptonically, and the other hadronically. This production and decay chain has been previously considered in [39]. Events were generated using MadGraph 5 [22], interfaced with Pythia 6 [23] for showering and hadronization and Delphes [25] for a fast, parameterized detector simulation. Recognizing the power of statistical learning techniques to efficiently find non-linear decision boundaries in feature space, we use boosted decision tree classifiers to discriminate between signal and background events. For each channel, we provide the classifier with a mixture of low-level and high-level features. Low-level features include readily available information such as the momenta of the final state particles, whereas high-level features are functions of the low-level features designed to exploit kinematic relations unique to each decay topology. In practice, using high and low level features in conjunction with each other yields better results than using either of them alone.

#### *Exotic decays of neutral Higgses*

For the exotic decay modes  $(A/H) \rightarrow (H/A)Z$  with the final state  $\tau\tau ll$ , the following strategy was taken to prepare feature arrays for the boosted decision tree classifier. We consider two possibilities for the decay of the  $Z$  boson:  $Z \rightarrow bb$  (case A), and  $Z \rightarrow l^+l^-$  (case B). The procedure is described below.

1. *Trigger.* We selected events that passed one of the following trigger criteria:
  - a) At least one lepton with  $p_T > 30$  GeV.
  - b) Two leptons, with the hardest lepton having  $p_T > 20$  GeV and the second hardest lepton having  $p_T > 10$  GeV.
  - c) A minimum missing transverse energy of 100 GeV.
2. *Identification.* We required events have at least two  $b$ -tagged jets (case A), or at least one pair of oppositely charged  $\tau$ -tagged jets (case B). For both cases, we require exactly two leptons (electrons or muons) with the same flavor and opposite sign.
3. *Calculate and collect features.* For events that pass the trigger and identification criteria above, we construct the following set of features:
  - a) *Z candidate.* We combine the momenta of the two same flavor, opposite sign leptons to form the  $Z$  candidate, and calculate its invariant mass,  $m_{ll}$ .
  - b) *Lighter neutral Higgs candidate.* We combine the momenta of the two leading  $b$ -tagged jets (case A) or the two  $\tau$ -tagged jets (case B) to form the lighter neutral Higgs candidate, and calculate its invariant mass, denoted either  $m_{bb}$  or  $m_{\tau\tau}$ .
  - c) *Heavier (parent) neutral Higgs candidate.* We combine the momenta of the  $Z$  candidate and the  $A/H$  candidate to form the charged Higgs candidate  $H^\pm$ , and calculate its invariant mass, denoted  $m_{llbb}$  (case A) or  $m_{ll\tau\tau}$  (case B).
  - d) *Other features:* We also collect the following set of features: the transverse momenta of the leptons, and  $b$ -tagged jets (case A), or the  $\tau$ -tagged jets (case B). Finally, we collect the missing transverse energy and hadronic transverse energy of the event.

#### *Exotic decays of the charged Higgs*

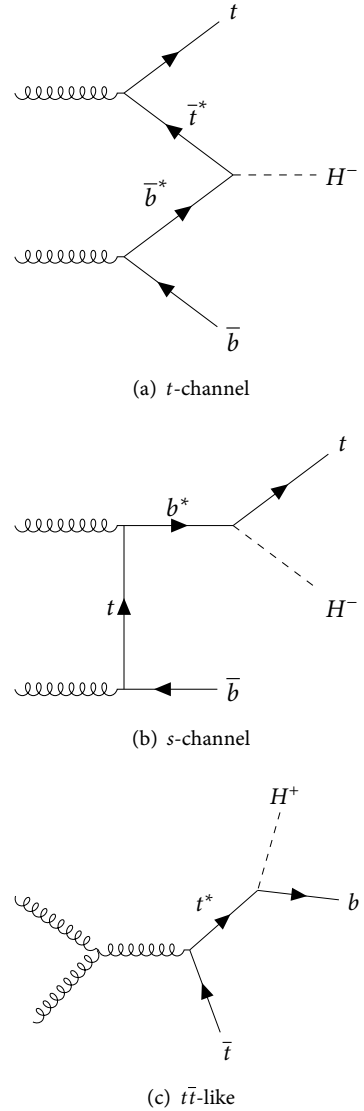
The search channel involving the charged Higgs, has the production and decay chain:

$$pp \rightarrow tbH^+ \rightarrow (Wb)b(HW) \rightarrow l\nu bb\tau_h\tau_l jj.$$

Here, one of the  $W$ 's and one of the  $\tau$ s decays hadronically, and the other decays leptonically. We employed the following strategy to construct input features for our classifier.

1. *Identification.* We required events have exactly one or two  $b$ -tagged jets, at least two untagged jets, exactly one  $\tau$ -tagged jet, and exactly two leptons (electrons or muons) with the same charge which is opposite to that of the  $\tau$ -tagged jet.
2. *Calculate and collect features.* As a test of the software setup, we analysed this channel with only the following low-level features: the transverse momenta of the leptons, the leading  $b$ -tagged jet, and the untagged jets, and the missing and hadronic transverse

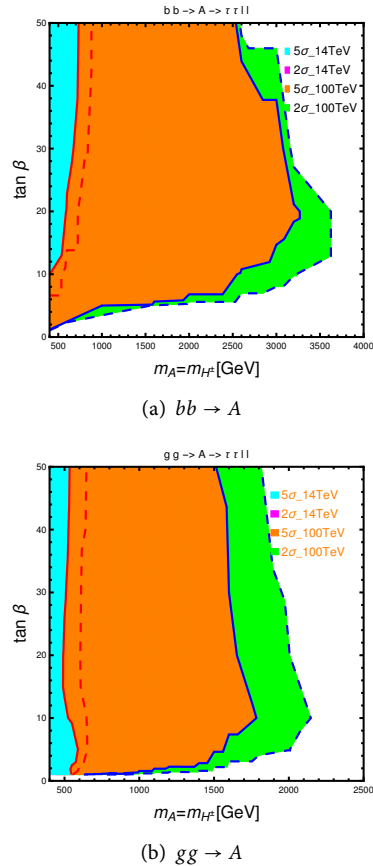
**Figure 5.2:** Feynman diagrams for charged Higgs production in association with a heavy quark.)



energies of the event. In the future, we aim to reconstruct the lighter Higgs  $H$  and the charged Higgs  $H^\pm$ , building upon the strategy in [39], and using the calculated invariant masses as input features for the classifier.

### 5.5 Preliminary results

**Figure 5.3:** Exclusion and discovery limits for the channel  $A \rightarrow HZ \rightarrow \tau\tau ll$ , for the 14 TeV LHC with  $100 \text{ fb}^{-1}$  (solid red line) and  $300 \text{ fb}^{-1}$  (dashed red line) and a 100 TeV collider with  $1000 \text{ fb}^{-1}$  (solid blue line) and  $3000 \text{ fb}^{-1}$  (dashed blue line).



Here we assume  $m_{12}^2 = m_H^2 s_\beta c_\beta$ . The top panel represents the  $bb \rightarrow A$  production channel, while the lower one represents the  $gg \rightarrow A$  production channel.

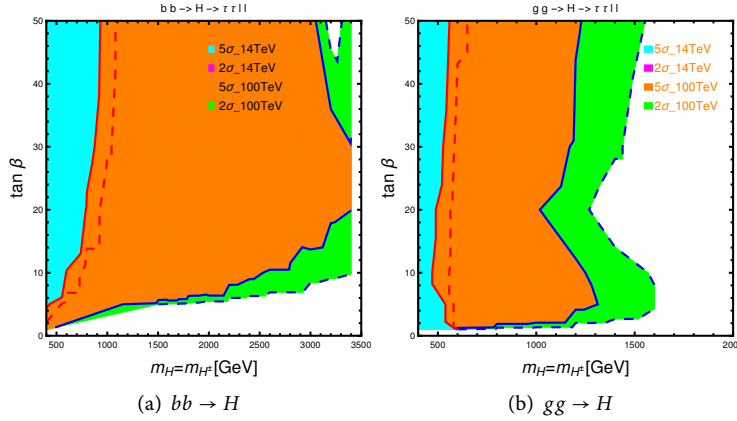
In this section, we will present some of the preliminary results of this project. In figure 5.3, we see the reach obtainable in the  $A \rightarrow HZ \rightarrow \tau\tau ll$  channels in the  $m_A = m_{H^\pm} - t_\beta$  plane, with  $m_A - m_H = 200 \text{ GeV}$ . The results are shown separately for the  $A$  produced via  $bb \rightarrow A$  (top panel), and  $gg \rightarrow A$  (bottom panel). The  $bb$  production channel has a significantly higher reach, being able to exclude points with  $m_A = m_{H^\pm}$  up to  $3.5 \text{ TeV}$  for  $t_\beta$  between  $15$  and  $20$ , for a  $100 \text{ TeV}$  collider (combined green, brown, and cyan regions). The corresponding reach for the  $gg$  production channel is only up to about  $2 \text{ TeV}$ . In figure 5.4, we see the reach obtainable in the  $H \rightarrow AZ \rightarrow \tau\tau ll$  channels, with  $m_H - m_A = 200 \text{ GeV}$ . Similar to the results for  $A \rightarrow HZ$ , the results for the  $bb$  production channel (left panel) are significantly better than those for the  $gg$  production channel (right panel). The  $bb$  production channel will be able to exclude points in the  $m_H = m_{H^\pm} - t_\beta$  plane up to  $3.5 \text{ TeV}$  for a wide range of values of  $t_\beta$  between  $10$  and  $50$ . The reach for the  $gg$  production channel is seen to be low for intermediate values of  $t_\beta$  of about  $20$ . This plane simply represents the region along the diagonal of benchmark plane IIB - this region was chosen since it survives all the theoretical and experimental constraints. Varying  $\tan \beta$  does not vary the kinematics of the final state particles, just the total  $\sigma \times \text{BR}$ .

For the charged Higgs channel  $H^\pm \rightarrow HW$  described in the previous section, the reach for a  $100 \text{ TeV}$  collider is shown in figure 5.5, in the  $m_{H^\pm} = m_A$  vs  $m_H$  plane. We see that with the simple set of input features described in section 5.4, we are able to exclude charged Higgses with masses up to  $2 \text{ TeV}$  for neutral Higgses  $H$  with masses up to  $500 \text{ GeV}$ . We expect that the addition of high-level features such as invariant masses will substantially improve the results. In all cases, the significance is calculated using the formula  $S/\sqrt{B}$ . For the  $14 \text{ TeV}$  LHC, we consider an integrated luminosity of  $300 \text{ fb}^{-1}$ , and for a  $100 \text{ TeV}$  collider, we consider an integrated luminosity of  $3000 \text{ fb}^{-1}$ .

### 5.6 Conclusions and outlook

In this chapter, we have provided some preliminary results from an ongoing project aimed at evaluating the prospects of discovering new heavy scalars from 2HDMs at the  $14 \text{ TeV}$  LHC and a  $100 \text{ TeV}$  collider, in the physically well-motivated but underexamined scenario where they can have large mass splittings. The approach we take is to examine the resulting ‘exotic’ decay modes of these heavy scalars, since they can dominate over the conventional decay modes in certain regions of parameter space once kinematically allowed. We began by examining

**Figure 5.4:** Exclusion and discovery limits for the channel  $H \rightarrow AZ \rightarrow \tau\tau ll$  for the 14 TeV LHC with  $100 \text{ fb}^{-1}$  (solid red line) and  $300 \text{ fb}^{-1}$  (dashed red line) and a 100 TeV collider with  $1000 \text{ fb}^{-1}$  (solid blue line) and  $3000 \text{ fb}^{-1}$  (dashed blue line).



Here we assume  $m_{12}^2 = m_H^2 s_\beta c_\beta$ . The left panel represents the  $bb \rightarrow H$  production channel, while the right represents the  $gg \rightarrow H$  production channel.

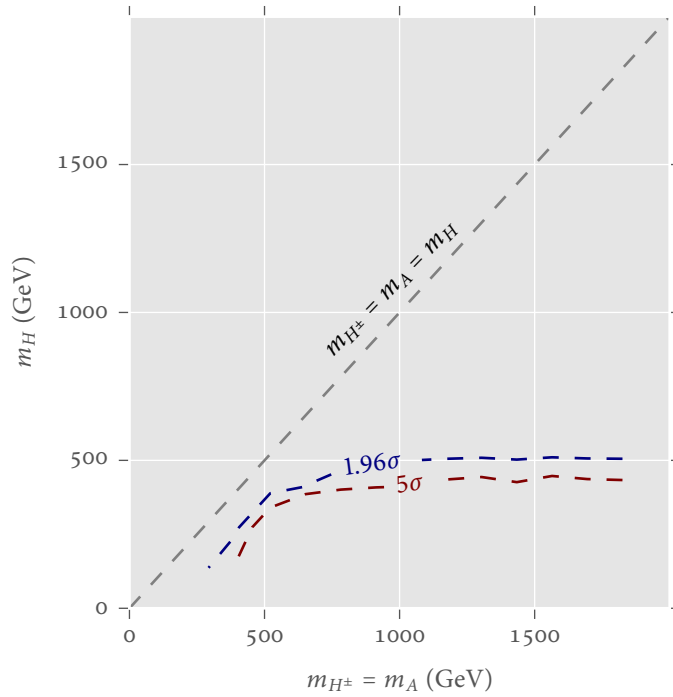


**Figure 5.5:** Exclusion and discovery reaches in the  $m_{H^\pm} - m_H$  plane for the exotic decay  $H^\pm \rightarrow HW^\pm$ , at a 100 TeV collider with an integrated luminosity of  $3 \text{ ab}^{-1}$ . Here we assume  $m_{12}^2 = m_H^2 s_\beta c_\beta$ .

two of the benchmark planes suggested in [4]. The first, benchmark plane IB, with  $m_A < m_H = m_{H^\pm}$  was probed using the exotic decay  $H \rightarrow AZ$ , with the subsequent decays  $A \rightarrow \tau\tau, Z \rightarrow ll$ . The second plane, labeled IIB, with  $m_H < m_A = m_{H^\pm}$ , was investigated using the exotic decay modes  $A \rightarrow HZ$  and  $H^\pm \rightarrow HW^\pm$ . For the first mode, we consider the final state  $\tau\tau ll$ , similar to the  $H \rightarrow AZ$  case, while for the second, we consider the more complicated final state  $bbWW\tau\tau$ , where one  $\tau$  and one  $W$  decay hadronically, and the other  $\tau$  and  $W$  decay leptonically. We used boosted decision tree classifiers to separate signal and background events, using a mixture of low-level features and physically inspired high-level features that are unique to each of the channels. For the benchmark plane IB, we found that we are able to exclude points with  $m_A = m_H^\pm$  up to 3.5 TeV at optimal points in the  $m_A = m_{H^\pm}$  plane, with a fixed  $m_A - m_H = 200$  GeV, for a 100 TeV collider. For benchmark plane IIB, we found that the reach is higher - we can discover points with  $m_H = m_{H^\pm}$  up to 3.5 TeV, again for the same mass difference between the parent and daughter Higgs. Preliminary results for the charged Higgs channel  $H^\pm \rightarrow HW^\pm \rightarrow \tau\tau W^\pm$  show an exclusion reach in benchmark plane IIB up to charged Higgs masses of about 2 TeV, for  $m_H$  up to 500 GeV. This region is complementary to the region explored by the channel  $A \rightarrow HZ$  (section 5.4) in the benchmark plane IIB. These preliminary results look promising, and we aim to complete our investigation of all the benchmark planes in the near future. An extended scalar sector arises frequently in theories beyond the Standard Model, and would have important implications for the electroweak phase transition, electroweak baryogenesis, as well as the hierarchy problem. Thus, understanding its structure is vital, and exotic decays provide a complementary avenue to do so.

## 6.1 Introduction

In 1933, the Swiss astronomer Fritz Zwicky turned his telescope to the night sky to measure the velocities of galaxies in a particular galaxy cluster known as the Coma cluster. He discovered that the visible matter in this cluster could not account for the speeds at which the galaxies were moving. He postulated that there must be some matter that does not emit light, but has mass and interacts only gravitationally with known matter. He termed this ‘dunkle materie’, or *dark matter*. The evidence for dark matter has only continued to grow since then, and we now know that there is far more of it in the universe than there is regular, or *baryonic* matter. The nature of dark matter is one of the most compelling mysteries in physics today.

Over the years, there have been many dark matter candidates, but the most widely accepted view today is that dark matter is comprised of a completely new kind of particle that interacts only weakly with the particles of the Standard Model and moves at non-relativistic speeds.

One of the most tantalizing clues as to the nature of dark matter is the so-called ‘WIMP miracle’ - the remarkable coincidence that the observed dark matter density in the universe can arise naturally from a particle with mass and couplings comparable to the weak scale. This raises the hope that such particles might feasibly be detected at colliders or direct detection experiments.

There are three main methods of detecting WIMP dark matter. The first, *direct detection*, involves constructing a well shielded, giant vat of a relatively inert substance, and waiting for dark matter particles to interact with that substance. The second, termed *indirect detection*, involves searching for signs of dark matter particles annihilating each other in the cosmos. The third method, *collider detection*, involves producing dark matter through high energy particle collisions and searching for their associated signatures. The three methods are depicted in figure 6.1, where  $\chi$  and SM represent dark matter and SM particles respectively, and the arrows represent the flow of time. The first two methods place relatively stringent constraints on the nature of dark matter, but have their own limitations. The smallest interaction cross-section between dark matter and regular matter that direct detection can measure is limited from below by the background of neutrinos from the sun. Indirect detection, on the other hand suffers from large astrophysical uncertainties [88]. Collider detection, therefore, is competitive with, and can possibly even surpass the other two methods.

WIMPs arise naturally in many extensions of the SM. Of these extensions, one of the most studied is the Minimal Supersymmetric Standard Model (MSSM), introduced in section 2.3. In the MSSM, the lightest su-

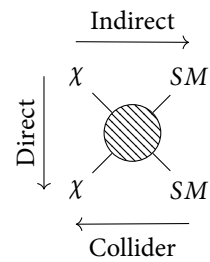


Figure 6.1: DM detection, three ways

persymmetric partner (LSP) is predicted to be absolutely stable, making it a good candidate for dark matter. The identity of the LSP is determined by the mass hierarchy of the superpartners, which in turn depends on how supersymmetry is broken. However, taking into account experimental constraints and phenomenological considerations, the lightest neutralino emerges as the most attractive candidate for the LSP [89].

Though a natural MSSM spectrum has the potential to tame the hierarchy problem, it is under siege from recent data from the LHC. A compelling alternative scenario comes in the form of split supersymmetry (split SUSY) [90–92]. In this scenario, the lightest superpartners are the fermionic ones (gauginos and higgsinos), with masses on the order of 1–10 TeV, while the scalar superpartners can be much heavier, on the order of 100 – 1000 TeV. In exchange for accepting some level of fine-tuning, we obtain numerous benefits, including the suppression of flavor-changing neutral currents and greater compatibility with data from CP-violation experiments [90].

The most interesting regions of the split SUSY parameter space lies beyond the reach of the LHC. Consider, for example the case in which the dark matter candidate is a nearly-pure bino. Even though the simplicity of its gauge singlet structure makes it an attractive DM candidate, It is well known that heavy bino LSPs heavier than about 200 GeV result in an overabundance of dark matter in the universe, in conflict with experimental observations. However, if the bino is nearly mass-degenerate with another supersymmetric particle, such as the gluino, stau, or a squark, it can coannihilate with it (see figure 6.2 for a Feynman diagram depicting the coannihilation with a stau), thereby reducing the dark matter abundance to acceptable levels [93]. Coannihilation with a gluino would raise the acceptable bino mass to  $\sim 7$  TeV, and coannihilation with a stop or squark raises the acceptable bino mass to  $\sim 2$  TeV. Bringing one of these particles down to the low-energy spectrum should not affect the branching ratio of the higgsinos too much. Gluino coannihilators would not change the branching ratios of the neutral higgsinos, since higgsinos are uncharged under  $SU(3)$ <sup>1</sup>. Higgsino-fermion-sfermion couplings are Yukawa-like, and are proportional to the mass of the fermion in the interaction vertex. Thus, this coupling will be relatively small (with the possible exception of the higgsino-top-stop case). In this study, we will simply assume that a scalar can be brought down into the low-energy spectrum to be nearly mass-degenerate with the bino, thus satisfying the relic density requirement. Such heavy binos are out of the reach of the 14 TeV LHC, but well within the reach of a 100 TeV collider.

This study aims to add to the corpus an assessment of the prospects of finding pair-produced neutral higgsinos that decay to binos via intermediate  $Z$  and  $h$  bosons, at a future 100 TeV collider, using razor variables. These variables [94] were originally designed for searches involving two heavy, mass-degenerate pair-produced particles, each of which decays into a visible and invisible set of particles. This topology matches that of our search channel, making this set of variables a natural

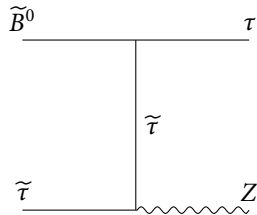


Figure 6.2: Feynman diagram for bino-stau coannihilation.

<sup>1</sup>But doing so would reduce the importance of electroweak search channels in comparison, as gluinos would then be abundantly produced.

choice for our analysis.

Finding higgsinos has traditionally been more challenging than finding winos, due to their lower production rate - it is thus important to devise innovative strategies to do so. In addition, the higgsino mass parameter  $\mu$  that governs the mass of the higgsino plays an important role in electroweak symmetry breaking [95]. This combination of NLSP (next-to-lightest supersymmetric partner) and LSP has been studied earlier in [96] with intermediate vector dibosons and multilepton final states. In this study, however, we attempt to exploit the relatively high branching ratio of the SM Higgs boson to  $b$  quarks (as suggested in [97]), and choose the decay modes  $Z \rightarrow ll$  and  $h \rightarrow bb$  for the intermediate  $Z$  and  $h$  bosons in our search channel.

At a 100 TeV collider, the backgrounds are going to be even larger than at the LHC. We will need to harness all the possible tools we can to deal with them. An ancillary goal of this study is to investigate the potential for machine learning (ML) techniques to augment our analysis. With the advent of more powerful computers and simultaneous advances in the field of statistical learning in recent years, the usage of ML is rising in experimental particle physics. In fact, the discovery of the SM Higgs boson in 2012 was done with the help of neural networks [1] and boosted decision trees [2].

The rest of this chapter is structured as follows. In section 6.2, we describe our model and search channel in more detail, and list the existing experimental constraints on it. In section 6.3, we describe our analysis strategies and results obtained for both the traditional cut-and-count analysis and the analysis performed with boosted decision trees. Finally, we conclude with the implications in section 6.4.

## 6.2 Model and experimental constraints

In this section, we will elaborate a little more on the structure of the neutralino sector in the MSSM, motivate our chosen search channel, and review some of the relevant experimental literature and limits.

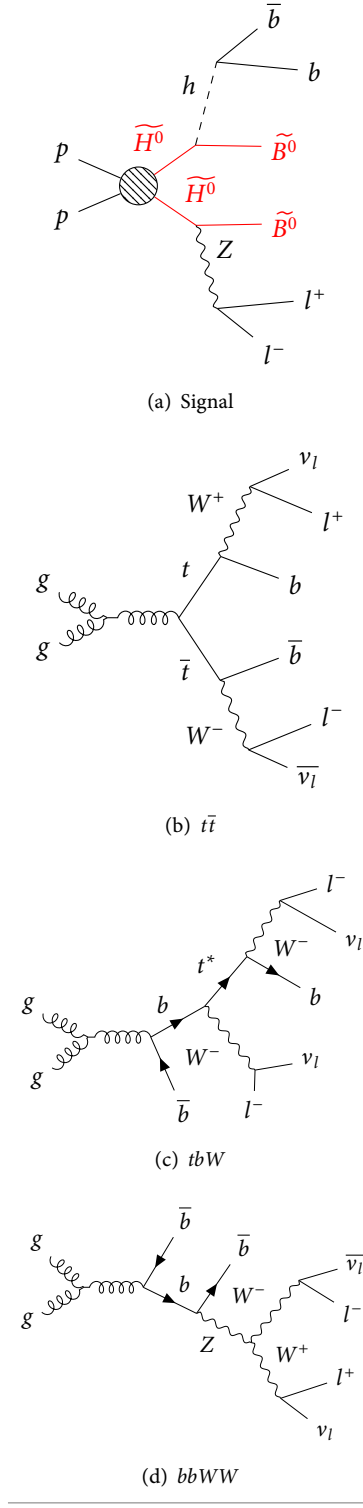
### *The neutralino sector*

The neutralino sector of the MSSM consists of four mass eigenstates  $(\tilde{\chi}_1^0, \tilde{\chi}_2^0, \tilde{\chi}_3^0, \tilde{\chi}_4^0)$  that are mixtures of the gauge eigenstates  $(\tilde{B}^0, \tilde{W}^0, \tilde{H}_u^0, \tilde{H}_d^0)$  - the bino, the wino, and the two neutral higgsinos, originally encountered in section 2.3. In the basis of these gauge eigenstates, the mass matrix of the neutralino can be written as

$$\mathbf{M}_{\tilde{N}} = \begin{pmatrix} M_1 & 0 & -c_\beta s_W m_Z & s_\beta s_W m_Z \\ 0 & M_2 & c_\beta c_W m_Z & s_\beta c_W m_Z \\ -c_\beta s_W m_Z & c_\beta c_W m_Z & 0 & -\mu \\ s_\beta s_W m_Z & -s_\beta c_W m_Z & -\mu & 0 \end{pmatrix}, \quad \text{Neutralino mass matrix}$$

where  $s_\beta = \sin \beta$ ,  $c_\beta = \cos \beta$ ,  $s_W = \sin \theta_W$ , and  $c_W = \cos \theta_W$ . The angle  $\beta$  is basically the same one encountered in section 2.2. It is a central

**Figure 6.3:** Feynman diagrams for the signal and background processes (Generated using [98].)



parameter of the theory, parameterizing the mixing between the two Higgs doublets,  $H_u$  and  $H_d$ . It is defined as  $\tan \beta = v_u/v_d$ , where  $v_u$  and  $v_d$  are the vacuum expectation values of  $H_u^0$  and  $H_d^0$ . The parameters  $M_1$ ,  $M_2$ , and  $\mu$  are the coefficients of bino, wino, and higgsino mass terms in the soft supersymmetry breaking Lagrangian.

This matrix can be diagonalized with the unitary matrix  $\mathbf{N}$  to obtain

$$\mathbf{N}^* \mathbf{M}_{\widetilde{\chi}} \mathbf{N}^{-1} = \begin{pmatrix} m_{\widetilde{\chi}_1^0} & 0 & 0 & 0 \\ 0 & m_{\widetilde{\chi}_2^0} & 0 & 0 \\ 0 & 0 & m_{\widetilde{\chi}_3^0} & 0 \\ 0 & 0 & 0 & m_{\widetilde{\chi}_4^0} \end{pmatrix},$$

where  $m_{\widetilde{\chi}_i^0}$  are the masses of the neutralino mass eigenstates.

In the limit of  $m_Z \ll |\mu \pm M_1|, |\mu \pm M_2|$ , the mass eigenstates are, to good approximation, a nearly pure bino,  $\widetilde{B}^0$ , with mass  $M_1$ , a nearly pure wino,  $\widetilde{W}^0$ , with mass  $M_2$ , and nearly pure higgsinos  $\widetilde{H}_{1,2}^0 = (\widetilde{H}_u^0 \pm \widetilde{H}_d^0)/\sqrt{2}$ , with mass  $|\mu|$ . This limit is well-motivated, since we are considering heavy electroweakinos that are out of the reach of the LHC - the minimum mass of the higgsinos considered is 500 GeV, and the wino is decoupled to 5 TeV.

The optimal search strategy for finding electroweakinos is highly dependent on the mass difference between them. Phenomenological collider studies on finding electroweakinos separated by about 0.1 - 50 GeV at a 100 TeV collider can be found in [88, 99–101], while well-separated spectra have been studied in [95, 96].

So far, the well-separated spectra have been studied using multi-lepton channels, of the form

$$pp \rightarrow \widetilde{\chi}_{\text{NLSP}} \widetilde{\chi}_{\text{NLSP}} \rightarrow VV + \widetilde{\chi}_{\text{LSP}} \widetilde{\chi}_{\text{LSP}} \rightarrow 2l/3l + \cancel{E}_T + \widetilde{\chi}_{\text{LSP}} \widetilde{\chi}_{\text{LSP}}$$

where  $\widetilde{\chi}_{\text{NLSP}}$  is the next-to-lightest neutralino or chargino, and  $\widetilde{\chi}_{\text{LSP}}$  is the lightest neutralino. These searches work well since the large mass difference between the electroweakinos can lead to energetic leptons that can be easily identified. Among the multi-lepton searches, the trilepton searches (with  $W$  and  $Z$  as the intermediate dibosons) have the best reach, due to the high production cross-section of chargino-neutralino

Stage	$\widetilde{\chi}_{2,3}^0 \widetilde{\chi}_2^\pm$	$\widetilde{\chi}_2^0 \widetilde{\chi}_3^0$
Pair production cross section	60 fb	16 fb
Intermediate diboson contribution ( $WZ$ )	30 fb	( $Zh$ ) 8 fb
Applying $BR(W \rightarrow l\nu)$ , $BR(Z \rightarrow ll) \& BR(h \rightarrow bb)$	0.42 fb	0.32 fb

**Table 6.1:** Comparison of cross-sections for  $(\widetilde{\chi}_{2,3}^0 \widetilde{\chi}_2^\pm)$  and  $(\widetilde{\chi}_2^0 \widetilde{\chi}_3^0)$ , for  $|\mu| \approx 1$  TeV, at a 100 TeV  $pp$  collider. The pair-production cross sections are taken from [96]. The branching ratio to intermediate dibosons is evaluated in the limit where the Goldstone equivalence theorem applies so that  $BR(\widetilde{\chi}_{2,3}^0 \rightarrow \widetilde{\chi}_0^1 h) \approx BR(\widetilde{\chi}_{2,3}^0 \rightarrow \widetilde{\chi}_0^1 Z) \approx 50\%$ . The branching ratios of  $W$ ,  $Z$ , and  $h$  are taken to be the same as the SM ones listed in the PDG review [62].

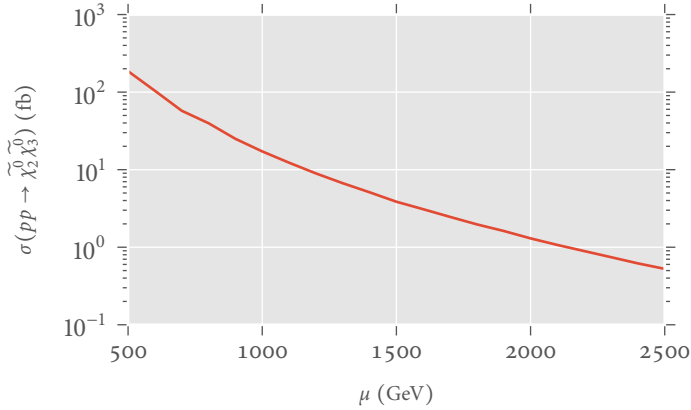


**Figure 6.4:** Higgsino pair production cross section as a function of  $\mu$ , for  $M_1 = 25$  GeV.

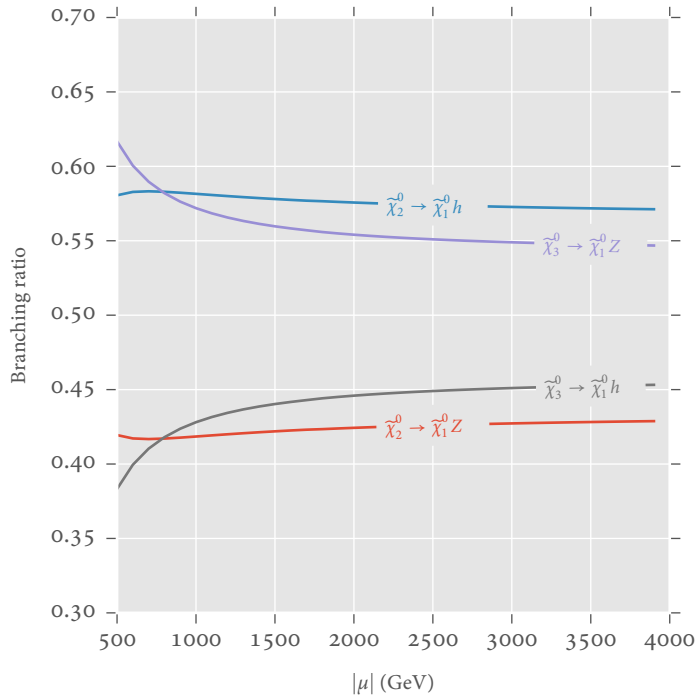


**Figure 6.5:** Higgsino decay branching ratios of  $\mu$ , for  $M_1 = 25$  GeV.

pairs combined with the large reduction in  $t\bar{t}$  and QCD backgrounds obtained by requiring three leptons. Multilepton searches with  $Zh$  and  $ZZ$  as the intermediate dibosons are unlikely to be as powerful, due to the lower pair-production cross-section of neutral higgsinos, combined with the low branching ratio of  $Z$  to leptons. However, if we move beyond multilepton searches, the channel with  $Zh$  as the intermediate dibosons emerges as a possible competitor to the  $WZ$  channel. If the  $Z$  decays leptonically and  $h$  decays to a pair of  $bs$ , then after applying the relevant branching ratios, the signal cross sections become comparable (for details, see table 6.1).

In this study, we will focus on a well-separated electroweakino spectrum, with  $M_2 \gg |\mu|, M_1$ , and study the process:

*Our signal process*

$$pp \rightarrow \tilde{\chi}_2^0 \tilde{\chi}_3^0 \rightarrow (Z \tilde{\chi}_1^0)(h \tilde{\chi}_1^0) \rightarrow ((l^+ l^-) \widetilde{B}^0)((b \bar{b}) \widetilde{B}^0),$$

which is manifested at colliders as a final state with two  $b$ -jets, two same flavor, opposite sign leptons, and missing transverse energy. Note that  $\tilde{\chi}_{2,3}^0$  represents neutral higgsino-like NLSPs, and  $\tilde{\chi}_1^0$  represents bino-like LSPs. The main backgrounds for this process are:  $t\bar{t}$ ,  $t b W$  with the  $b$  and  $W$  not coming from a  $t$ , and  $b b W W$  with no intermediate  $s$ -channel top quarks. See figure 6.3 for representative Feynman diagrams for the signal and background processes. The typical pair-production cross section for the higgsino-like NLSPs is on the order of less than 10 fb for  $|\mu| > 1$  TeV, as can be seen in figure 6.4.

*Couplings and branching ratios*

The mixing of the neutralino gauge eigenstates gives rise to complicated expressions for the couplings involving the mass eigenstates. For consistency, we use SUSY-HIT [102] to calculate the branching ratios  $BR(\tilde{\chi}_{2,3}^0 \rightarrow h \tilde{\chi}_1^0)$ ,  $BR(\tilde{\chi}_{2,3}^0 \rightarrow Z \tilde{\chi}_1^0)$ , and  $BR(h \rightarrow b b)$ . The branching ratios for higgsinos decaying into  $h/Z + \tilde{\chi}_1^0$  is shown in figure 6.5. For all our benchmark points, we decouple the neutral wino, setting  $M_2 = 5$  TeV.

*Review of experimental searches and limits*

While the majority of the existing searches for supersymmetry focus on gluino pair production, there are a number of analyses involving electroweakino pair production as well, which we will attempt to briefly review here. Searches involving multiple leptons and missing energy ( $2l/3l + \cancel{E}_T$ ) in the final state are described in [103–105], assuming a wino-like NLSP and a bino-like LSP. The best reach is obtained in the  $2/3l$  channel, with NLSP masses up to 1 TeV excluded for LSP masses up to 500 GeV. The trilepton channel is a close second-best, with NLSP masses up to 1 TeV excluded for a massless LSP. Both of these results have been calculated with  $13.3 \text{ fb}^{-1}$  of 13 TeV LHC data by ATLAS.

Topologies with one or two hadronically-decaying tau leptons and missing energy in the final state have been studied in [106, 107], with the greatest reach obtained by ATLAS in [106], using 13 TeV data - they are able to exclude wino-like NLSPs up to a mass of 700 GeV for a massless bino-like LSP.

Photon signatures with the final states  $\gamma\gamma/\gamma b/\gamma j/\gamma l/\gamma jj + \cancel{E}_T$  been used to probe gauge mediated supersymmetry breaking models in [108–112]. Winos are excluded below 710 GeV for nearly bino-like LSPs that are nearly mass-degenerate with them in [112]. The study [110] excludes winos up to a mass of 590 GeV in the final state  $\gamma\gamma + \cancel{E}_T$ . The final state  $\gamma l + \cancel{E}_T$  is used to exclude winos up to 360 GeV in [109].

Searches with a combination of leptons and jets in the final states can be found in [113–115]. Winos up to 465 GeV are excluded in the  $2l + 0/2j$  final states in [113]. A compressed mass spectrum is studied in [114], with a mass difference of about 50 GeV between winos and binos. This study uses the vector boson fusion channel, with a final state of  $2l + 2j + \cancel{E}_T$ , and excludes winos up to a mass of 170 GeV. Of particular interest to us is the analysis in [115], where higgsinos can be excluded up to a mass of 380 GeV using the  $bbl + \cancel{E}_T$  final state, but cannot be discovered in any region of the relevant parameter space. As we shall see, a 100 TeV collider will enable us to greatly improve upon these limits.

### 6.3 Analysis Details

In this section, we will describe our strategies for both the traditional cut-and-count analysis, as well as the analysis carried out with boosted decision trees.

#### *Simulation*

We simulated parton-level events using MadGraph5 v2.3.2.2 and MadEvent [22], then passed those events to Pythia 6 [23] for showering and hadronization. Finally, we used Delphes 3 [25] to perform a fast, parametrized detector simulation, with the detector card devised by the FCC-hh working group<sup>2</sup>. For the backgrounds, we allowed up to one additional jet in the final state, to approximate NLO QCD effects, and performed MLM matching with the xqcut parameter set to 40 GeV. The Higgsino pair production cross sections were calculated using Prospino2 [116]. To decouple the wino, we set its mass parameter  $M_2$  to 5 TeV.

<sup>2</sup><https://github.com/HEP-FCC/FCCSW/tree/master/Sim/Sim/Delphes/Interface/data>

One of the challenges we faced while performing this analysis was dealing with the sheer number of background events to generate and analyze. At a 100 TeV collider, the background cross-sections grow very large compared to their 14 TeV counterparts. For example, the cross section for the inclusive production of top quark pairs increases from  $\sim 975$  pb (N<sup>3</sup>LO) to  $\sim 34,000$  pb (NLO) [87], that is, increasing the collision energy by about seven times increases the number of events by a factor of more than 30! Multiplying this by 3 ab<sup>-1</sup> (the expected integrated luminosity from the first 10 years of running the FCC), gives us 96 billion top pair production events. Simulating this many events would require enormous amounts of computing time as well as huge amounts of storage. To alleviate the first problem, we generated events on the University of Arizona cluster, leveraging the power of many computing nodes to perform event generation simultaneously. But this alone would not be enough.

Since we expect our signal process to have a dilepton resonance from an on-shell  $Z$  boson, we restricted the phase space for event generation for backgrounds to the region where the invariant mass of dilepton pairs lies between 80 and 100 GeV. Additionally, the bino dark matter that

escapes the detector would result in a large amount of missing transverse energy ( $\cancel{E}_T$ ), so we required a minimum  $\cancel{E}_T$  of 100 GeV at the parton level for the backgrounds as well.

At the reconstructed level, we relaxed the lepton isolation criterion in the `Delphes` detector card,  $\Delta R_{\text{min}}$  from 0.4 to 0.05. This is motivated by the fact that due to the large mass difference between the higgsino NLSP and the bino LSP in our search channel, the intermediate  $Z$  bosons will be highly boosted, and the leptons to which they decay will be highly collimated. The value of 0.05 is consistent with what is suggested in previous 100 TeV studies ([95, 96, 117]) and will allow for easier comparison between strategies.

#### Rectangular cuts

For the cut-and-count analysis, we implemented successive one-dimensional cuts on the variables listed below, using the `MadAnalysis 5` package [118].

1. *Trigger:* Events were selected if they had at least one lepton with  $p_T > 100$  GeV.
2. *Identification:*

- We required that events contain exactly two leptons of the same flavor and with opposite signs (SFOS), with  $p_T > 15$  GeV and  $|\eta| < 2.5$ .
- We required that events contain at least two  $b$ -tagged jets with  $p_T > 30$  GeV and  $|\eta| < 2.5$ .

3. *Invariant mass of  $Z$ -candidate:* We required that the invariant mass of the two leptons,  $m_{l^+l^-}$ , lie between 85 and 95 GeV.
4. *Invariant mass of  $h$ -candidate:* We combine the two  $b$ -tagged jets with the highest  $p_T$  to form a  $h$  candidate and require that its invariant mass,  $m_{bb}$ , lies between 75 and 150 GeV.

5. *Missing Transverse Energy:* We required events to have a minimum missing transverse energy of 400 GeV.
6. *Razor variables:* Consider the pair production of two massive particles  $S_1$  and  $S_2$  that decay into the particles  $(Q_1, \chi_1)$  and  $(Q_2, \chi_2)$  respectively, where  $\chi_{1,2}$  are invisible and have the same mass. The first razor variable,  $M_R$ , inherits the knowledge of the mass difference between the parent particle (the higgsino), and the invisible particle (the bino). It is given by

$$M_R = \sqrt{(E_1 + E_2)^2 - (q_1^z + q_2^z)^2},$$

where  $E_i$  are the energies of the visible particles  $Q_i$ , and  $q_i^z$  are the  $z$ -components of their momenta. The second razor variable,  $M_T^R$ , can be thought of as a longitudinally-invariant analogue of the transverse mass, and is given by:

$$M_T^R = \sqrt{\frac{1}{2} \left[ \cancel{E}_T (|\vec{q}_{1T}| + |\vec{q}_{2T}|)^2 - \vec{\cancel{E}}_T \cdot (\vec{q}_{1T} + \vec{q}_{2T}) \right]}.$$

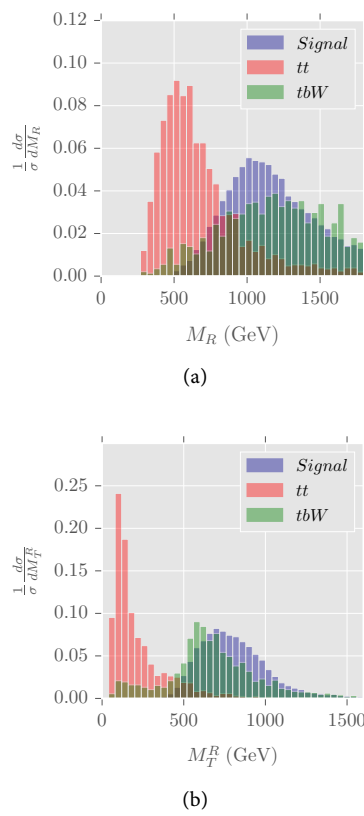


**Figure 6.6:** Normalized distributions of the razor kinematical variables  $M_R$  (top) and  $M_T^R$  (bottom) for a 1 TeV higgsino NLSP and 25 GeV bino LSP

	$\sigma_{\text{signal}}$	$\sigma_{tt}$	$\sigma_{tbW}$	$\sigma_{bbWW}$	$\sigma_{\text{total, background}}$	$S/B$	$S/\sqrt{B}$
Original	0.37	35,998	4,176	7.8	40,182	$9.1 \times 10^{-6}$	0.10
Trigger	0.31	5,321	1,058	2.5	6,382	$4.9 \times 10^{-5}$	0.21
SFOS leptons	0.25	1,774	360	0.88	2,135	$1.2 \times 10^{-4}$	0.30
2 $b$ jets	0.04	290	62	0.09	352	$1.3 \times 10^{-4}$	0.13
$\cancel{E}_T < 400$	0.03	5.3	6.8	0.007	12	0.003	0.49
$m_{ll} \in [85, 95]$	0.03	2.1	3.3	0.004	5.3	0.005	0.62
$m_{bb} \in [75, 150]$	0.02	0.59	0.30	$8.2 \times 10^{-4}$	0.90	0.02	1.3
$M_R > 800$	0.02	0.03	0.20	$3.3 \times 10^{-4}$	0.23	0.09	2.2
$M_T^R > 400$	0.02	0.008	0.18	$1.9 \times 10^{-4}$	0.19	0.10	2.4

**Table 6.2:** Representative cut flow table for the benchmark point  $|\mu| = 1 \text{ TeV}$ ,  $M_1 = 25 \text{ GeV}$ , for a traditional cut-and-count analysis. All cross sections are given in femtobarns, and the units for the missing energy, invariant mass, and razor variable cuts are GeV. The significance,  $S/\sqrt{B}$ , is calculated for an integrated luminosity of  $3 \text{ ab}^{-1}$ .

For our process, the visible particles  $Q_i$  correspond to the reconstructed SM Higgs and  $Z$  bosons, and the invisibles  $\chi_i$  correspond to the bino LSPs. We scanned across a range of values of these variables to find the cuts that yielded the greatest significance. Representative kinematic distributions of these variables for a 1 TeV higgsino and a 25 GeV bino are shown in figure 6.6, after the trigger, identification, and  $\cancel{E}_T$  cuts. We can see that the distribution of  $M_R$  is peaked around 1 TeV for the signal, which is consistent with what we would expect, since it corresponds to the mass difference between the NLSP and LSP. The distribution for the  $bbWW$  background is not shown, since it is negligible in comparison to the others. For this mass combination, requiring  $M_R > 800 \text{ GeV}$  and  $M_T^R > 400 \text{ GeV}$  yields the greatest significance.

In table 6.2, we show the cut efficiencies for a representative signal benchmark point with  $|\mu| = 1 \text{ TeV}$  and  $M_1 = 25 \text{ GeV}$ . The initial signal cross-section is calculated using Prospino2 at next-to-leading order, and is then multiplied by the branching ratios calculated using SUSY-HIT. The cross-sections of the backgrounds are averages of the cross-sections output by MadEvent after performing the MLM matching procedure. Their small size reflects the  $m_{ll}$  and  $\cancel{E}_T$  cuts we imposed at the parton level. For all the benchmark points, we require a minimum of 5 signal events left over after cuts. We can see that, after applying our cuts,  $tt$  and  $tbW$  remain as the dominant backgrounds. The values of the razor variable cuts were chosen to maximize the significance,  $S/\sqrt{B}$  (calculated for an integrated luminosity of  $3000 \text{ fb}^{-1}$ ), shown in the last column.

#### Optimizing using gradient boosted decision trees

For each signal benchmark point and background process, we pre-selected events that passed the lepton trigger, contained two SFOS leptons and two  $b$ -tagged jets, and calculated a number of features for each

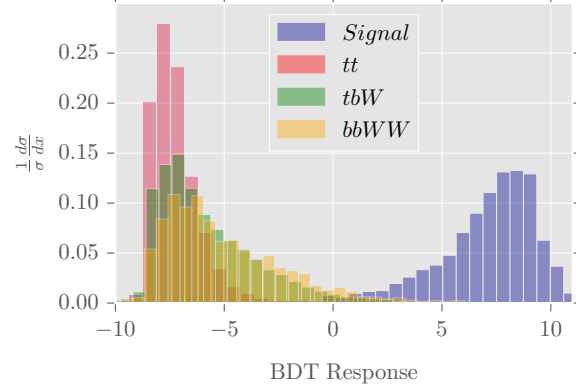


**Figure 6.7:** Distribution of the decision function of the gradient boosted decision tree classifier algorithm for the signal ( $|\mu| = 1 \text{ TeV}$ ,  $M_1 = 25 \text{ GeV}$ ) and backgrounds.

	$\sigma_{\text{signal}}$	$\sigma_{\text{tt}}$	$\sigma_{\text{tbW}}$	$\sigma_{\text{bbWW}}$	$\sigma_{\text{total,background}}$	$S/B$	$S/\sqrt{B}$
Original	0.37	35,998	4,176	7.8	40,182	9.1e-06	0.10
Preselection	0.04	290	62	0.09	352	1.3e-04	0.13
BDT response $> 5.1$	0.04	0.02	0.04	4.8e-04	0.06	0.63	8.4

**Table 6.3:** Representative cut flow table for the same benchmark point and integrated luminosity as in [table 6.2](#), but using a boosted decision tree (BDT) analysis instead. The preselection is equivalent to the trigger and identification cuts listed in [table 6.2](#). As before, all the cross sections are in femtobarns.

event. A mixture of low-level and high level features was seen to have the greatest effectiveness. The features chosen were  $m_{ll}$ ,  $m_{bb}$ ,  $M_R$ ,  $M_T^R$ ,  $\cancel{E}_T$ , the total hadronic transverse energy  $THT$ , and transverse momenta of individual final state leptons and b-quarks:  $p_T(l_1)$ ,  $p_T(l_2)$ ,  $p_T(b_1)$ , and  $p_T(b_2)$ . We then divided the events into training and test sets, with the training set comprising 75% of signal events and 30% of background events. We used the `scikit-learn` package [119] to implement our analysis. A boosted decision tree classifier was trained with 1000 weak learners and a learning rate of 0.025. After the classifier is trained, we use it to assign scores to individual events. A more negative score indicates a more background-like event, and a more positive score denotes a more signal-like event. After the scores have been assigned to the events in the test sets, we can use this score just as we would a regular kinematical variable, that is, we apply a cut that selects events with a minimum of this score. The value of the cut is chosen to maximize the significance for each signal benchmark point. The distribution of scores for the specific benchmark point with  $|\mu| = 1 \text{ TeV}$  and  $M_1 = 25 \text{ GeV}$  is shown in [figure 6.7](#). We observe that there is an appreciable separation between the signal and background distributions.

[Table 6.3](#) shows the cut efficiencies for the same representative benchmark point as in [table 6.2](#), but this time for a boosted decision tree (BDT) analysis. We observe that the statistical significance we can achieve goes up from 2.4 to 8.4, a roughly four-fold increase.

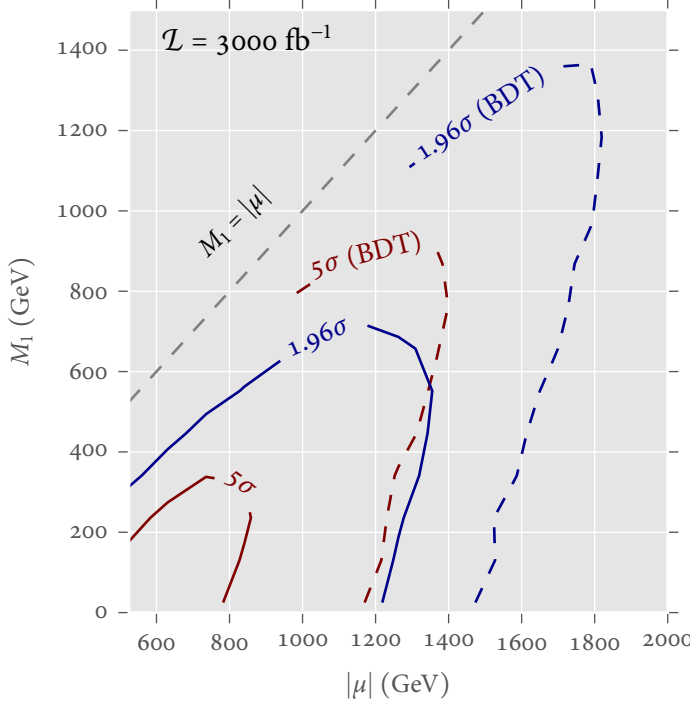


**Figure 6.8:** Discovery (red) and exclusion (blue) contours for the traditional cut-and-count analysis (solid) and boosted decision tree analysis (dashed), for an integrated luminosity of  $3000 \text{ fb}^{-1}$ .

*Note on low event counts and statistics.* For certain values of the cuts on kinematical variables or the score of the ML classifier, no events survived for one or more of the background components. To guard against overly optimistic estimates of the significance  $S/\sqrt{B}$ , we set a lower bound of 3 for the number of events after cuts for each background component. This corresponds to the 95% confidence interval for a Poisson distribution.

#### Reach in parameter space

Figure 6.8 shows the expected reach in parameter space for exclusion and discovery. The cut-and-count strategy is able to discover higgsinos up to 750 GeV and exclude them up to 1.3 TeV. The boosted decision tree analysis, improves upon this - it is able to discover higgsinos up to 1.3 TeV, and exclude them up to 1.8 TeV in favorable points in parameter space. Similarly, binos can be discovered up to 300 GeV and excluded up to 800 GeV with the rectangular cut analysis, while the BDT analysis can discover them up to about 900 GeV and exclude them up to 1.3 TeV. Table 6.4 contains a summary of these results. We do not include systematic errors in these estimates.

This improvement is substantial, but perhaps not spectacular. However, it should be kept in mind that this is probably a conservative estimate. Since we reserve 30% of the data for training purposes, and impose the condition that the minimum number of events after cuts for the backgrounds must be 3 (see note at the end of section 6.3), the true

**Table 6.4:** Discovery reaches and expected exclusion limits (in TeV) for the parameters ( $|\mu|, M_1$ ) for the rectangular cuts and boosted decision tree analyses.

Analysis type	$5\sigma$ (discovery)	$1.96\sigma$ (exclusion)
Rectangular cuts	(0.75, 0.30)	(1.3, 0.8)
BDT Analysis	(1.3, 0.90)	(1.8, 1.3)

rate of background rejection by the classifier is likely underestimated, and the expected significance from the BDT analysis will improve. This extrapolation is qualitatively supported by the high degree of separation between signal and background events seen in figure 6.7, and the fact that a larger fraction of the signal events are preserved with the BDT approach compared to the rectangular cut approach, as can be seen in tables 6.2 and 6.3.

In regions with large mass differences between the LSP and NLSP, the reach is not as good, since the intermediate SM higgs boson will be highly boosted, and thus decay into a highly collimated pair of  $b$ -jets. The extent to which this affects our results can be estimated from the fourth row in table 6.2. We see that requiring two  $b$ -tagged jets reduces our signal cross-section by roughly 87%, which is far more than the 28% reduction that might be naively expected from the  $b$ -tagging efficiency of about 85% specified in our Delphes card.

#### 6.4 Conclusion

In this study, we examined the potential for a 100 TeV collider to discover pair-produced heavy higgsinos that decay to bino LSPs via intermediate  $Z$  and  $h$  bosons, that in turn decay to a pair of leptons and  $b$  quarks respectively. More specifically, we examined a split-SUSY like scenario where the scalar superpartners and the wino are heavy and decoupled, reducing the number of available decay channels for the higgsinos.

To do this, we pursued two analysis strategies. While one was more traditional, using rectangular selection cuts on kinematical variables, the other used a boosted decision tree classifier trained with a number of low and high level features. We expected that the machine learning approach would be able to more efficiently determine the optimal decision boundary between signal and background events in feature space than the traditional rectangular cuts.

Overall, we find that the reach of our analysis strategy is a significant improvement over the current limits from the LHC. We found that the rectangular cut strategy has the potential to discover higgsino LSPs up to a mass of 750 GeV, and exclude them up to a mass of 1.3 TeV. As expected, the boosted decision tree classifier performs better, with the ability to discover higgsino NLSPs up to 1.3 TeV and exclude them up to a mass of 1.8 TeV. With this analysis, bino dark matter candidates can be discovered up to 900 GeV, and excluded up to 1.3 TeV. In the process, we highlighted the importance of generating enough Monte Carlo events to estimate the huge backgrounds at a 100 TeV collider.

Additionally, we found that the reach for both strategies is considerably reduced when the difference  $M_1 - |\mu|$  is high, since it results in a highly boosted  $h$  that decays to a collimated pair of  $b$ 's that will most likely be identified as a single jet. This is not an insurmountable difficulty - there are ways to deal with collimated jets, although they are beyond the scope of this work. This issue does, however, highlight the necessity of improving isolation performance at a 100 TeV machine, where large mass hierarchies can result in highly boosted and collimated decay products. For a review of currently used methods to determine jet substructure, see [120]. In the future, machine learning techniques might be profitably applied to this area as well - for a review of developments along this line, see [121]. The collimation of the  $b$ -jets and the fact that we take into account detector effects using Delphes result in a lower reach in the high  $|\mu|$ , low  $M_1$  region than the multilepton analysis in [96], which is able to exclude higgsinos up to a mass of 2.9 TeV for massless binos. The reach of our analysis is slightly higher in the region where the difference between  $|\mu|$  and  $M_1$  is smaller. This is consistent with our usage of the razor variable  $M_R$ , which is sensitive to the mass difference between the parent and daughter particles.

A 100 TeV proton-proton collider represents an excellent opportunity to discover physics beyond the standard model. The extremely high energies and luminosities involved will present new challenges for particle physicists, and it is likely that machine learning will play an important part in facing them.

*Acknowledgments.* We would like to thank Matthew Leone and Ken Johns for helpful discussions. An allocation of computer time from the UA Research Computing High Performance Computing (HPC) and High Throughput Computing (HTC) at the University of Arizona is also gratefully acknowledged. This work was supported in part by the Department of Energy (DoE) under Grant DE-FG02-13ER41976 / de-sc0009913.



# 7

## CONCLUSION

---

The discovery of the Higgs boson in 2012 completed the framework of the Standard Model of particle physics, which has been verified to unprecedented levels of precision. However, the journey is not yet over - the Standard Model either provides unsatisfactory answers to certain issues such as the hierarchy problem, or is silent on others, such as the nature of dark matter. Clearly, it cannot be the final word on the subject of particle physics. To address the issues that the SM does not, we must go beyond it, constructing new theories that provide satisfactory explanations of physics at high energy scales.

Many of these new theories predict scalar sectors larger than that of the SM. Two-Higgs Doublet Models (2HDMs) provide a general framework for studying these extended scalar sectors. They predict a collection of Higgs bosons, (as opposed to the single Higgs boson of the SM): two CP-even states  $h$  and  $H$ , a CP-odd state  $A$ , and a pair of charged state  $H^\pm$ . Traditional searches for these Higgses at particle colliders focus on them via their decays to SM final states. However, there are compelling scenarios in which these heavy scalars decay predominantly through exotic modes to non-SM final states. In certain regions of parameter space, these exotic modes can dominate the conventional decay modes to SM final states, and thus provide a complementary avenue for discovery.

In [chapter 4](#), we presented an analysis aimed at discovering light charged Higgses produced via top quark decay at the 14 TeV LHC. We found that the exotic decay channel  $H^\pm \rightarrow AW^\pm$  is able to probe the low  $t_\beta$  region better than the conventional decay channels.

In [chapter 5](#), we presented preliminary results from a project aimed at systematically covering a number of exotic decay scenarios through collider analyses for both the 14 TeV LHC and a future 100 TeV collider. We find that the preliminary results are promising, and cover a large swathe of 2HDM parameter space, up to scalar masses of 3.5 TeV, for a wide range of values of  $\tan\beta$ , at a 100 TeV collider.

Additionally, in [chapter 6](#), we presented an analysis aimed at discovering pair produced higgsino-like neutralinos that decay to bino-like neutralino LSPs at a 100 TeV collider. Both of these particles arise from the Minimal Supersymmetric Standard Model, described in [section 2.3](#). This heavily-studied model can be viewed a special case of a 2HDM that incorporates supersymmetry, a symmetry that connects fermions and bosons. This analysis is performed using razor variables and boosted decision trees. We find that we are able to exclude higgsinos up to 1.8 TeV for binos up to 1.3 TeV with this analysis.

In some ways, the three analyses presented in this dissertation can be viewed as a progression on two fronts. On the one hand, they involve increasingly high collider energies, going from 14 TeV to 100 TeV. On

the other, they involve an increasing use of machine learning techniques. The analysis of light charged Higgses solely uses rectangular selection cuts, the analysis involving higgsinos and binos qualitatively compares rectangular cut and machine learning strategies, and the analysis for exotic decays at 14 and 100 TeV uses machine learning exclusively. The author believes that it is likely that this trend will be reflected in particle physics in the future, as we attempt to grapple with increasingly difficult questions at the frontier of the field. Increasing collider energies will be required to probe physically well-motivated scenarios with a TeV scale mass spectrum, while machine learning techniques will be increasingly needed to tackle the extremely large backgrounds and small signal rates at future colliders.

### Open Science

The author strongly believes in the value of reproducible research and open science. In this spirit, an effort has been made to make as much of the source code involved in the creation of this dissertation freely available online.

- The source code for the dissertation manuscript itself can be found at <https://github.com/adarshp/dissertation>.
- The code for the analysis in [Chapter 6](#) can be found at <https://github.com/adarshp/Dark-Matter-at-100-TeV>
- The code for the analysis of the  $H^\pm \rightarrow HW^\pm$  decay channel in [Chapter 5](#) can be found at <https://github.com/adarshp/ExoticHiggs>.
- In addition, the code for both of these analyses utilizes a Python-based software framework, `clusterpheno`, written by the author during the course of his graduate work, for the purpose of performing large-scale event generation and analysis on the University of Arizona cluster. The source code for this framework can be found online at <https://github.com/adarshp/clusterpheno>.

## BIBLIOGRAPHY

---

- [1] Georges Aad et al., *Observation of a new particle in the search for the Standard Model Higgs boson with the ATLAS detector at the LHC*, Phys. Lett. **B716**. (2012), pp. 1–29, [[arXiv:1207.7214](#)] (cited on pages [17](#), [71](#)).
- [2] Serguei Chatrchyan et al., *Observation of a new boson at a mass of 125 GeV with the CMS experiment at the LHC*, Phys. Lett. **B716**. (2012), pp. 30–61, [[arXiv:1207.7235](#)] (cited on pages [17](#), [71](#)).
- [3] Felix Kling, Adarsh Pyarelal, and Shufang Su, *Light Charged Higgs Bosons to AW/HW via Top Decay*, JHEP **11** (2015), p. 051, [[arXiv:1504.06624](#)] (cited on pages [19](#), [62](#), [63](#)).
- [4] Felix Kling, Jose Miguel No, and Shufang Su, *Anatomy of Exotic Higgs Decays in 2HDM*, JHEP **09** (2016), p. 093, [[arXiv:1604.01406](#)] (cited on pages [19](#), [20](#), [62](#), [63](#), [68](#)).
- [5] Ta-Pei Cheng and Ling-Fong Li, *Gauge Theory of Elementary Particle Physics*, Oxford Science Publications, Clarendon Press, 1984 (cited on p. [21](#)).
- [6] Matthew D. Schwartz, *Quantum Field Theory and the Standard Model*, Cambridge University Press, 2014 (cited on p. [21](#)).
- [7] Anthony Zee, *Quantum Field Theory in a Nutshell*, Princeton University Press, 2010 (cited on p. [21](#)).
- [8] Peskin, Michael E. and Schroeder, Daniel V., *An Introduction to Quantum Field Theory*, Reading, USA: Addison-Wesley, 1995 (cited on p. [21](#)).
- [9] G. C. Branco, P. M. Ferreira, L. Lavoura, M. N. Rebelo, Marc Sher, and Joao P. Silva, *Theory and phenomenology of two-Higgs-doublet models*, Phys. Rept. **516** (2012), pp. 1–102, [[arXiv:1106.0034](#)] (cited on p. [21](#)).
- [10] Stephen P. Martin, *A Supersymmetry Primer*, (1997), [Adv. Ser. Direct. High Energy Phys.18,1(1998)], [[arXiv:hep-ph/9709356](#)] (cited on pages [21](#), [31](#)).
- [11] *The most precise picture of the proton*, 2015, URL: [http://www.desy.de/news/news\\_search/index\\_eng.html?openDirectAnchor=829](http://www.desy.de/news/news_search/index_eng.html?openDirectAnchor=829) (cited on p. [25](#)).
- [12] Felix Kling, *Exotic Higgs Decays*, PhD thesis, University of Arizona, 2016 (cited on p. [30](#)).
- [13] Sidney R. Coleman and Jeffrey E. Mandula, *All Possible Symmetries of the S Matrix*, Phys. Rev. **159** (1967), pp. 1251–1256 (cited on p. [32](#)).
- [14] Jeffrey E. Mandula, *Coleman-Mandula theorem*, Scholarpedia **10**. (2015), revision #147717, p. 7476 (cited on p. [32](#)).

- [15] Julius Wess and Bruno Zumino, *Supergauge Transformations in Four Dimensions*, Nucl. Phys. **B70** (1974), pp. 39–50 (cited on p. 32).
- [16] Rudolf Haag, Jan T. Łopuszanski, and Martin Sohnius, *All Possible Generators of Supersymmetries of the S Matrix*, Nucl. Phys. **B88**. (1975), p. 257 (cited on p. 32).
- [17] Abdus Salam and J. A. Strathdee, *Supergauge Transformations*, Nucl. Phys. **B76**. (1974), pp. 477–482 (cited on p. 32).
- [18] D. Froidevaux and P. Sphicas, *General-purpose detectors for the Large Hadron Collider*, Ann. Rev. Nucl. Part. Sci. **56** (2006), pp. 375–440 (cited on p. 38).
- [19] Marzena Lapka, 2011, URL: <https://cms-docdb.cern.ch/cgi-bin/PublicDocDB>ShowDocument?docid=4172> (cited on p. 39).
- [20] William H. Press, Saul A. Teukolsky, William T. Vetterling, and Brian P. Flannery, *Numerical Recipes: The Art of Scientific Computing*, 3rd ed., New York, NY, USA: Cambridge University Press, 2007 (cited on p. 39).
- [21] Adarsh Pyarelal, *A Reggeized Model for  $\eta(548)$  meson production in high energy proton/proton collisions*, Reed College, 2011 (cited on p. 40).
- [22] J. Alwall, R. Frederix, S. Frixione, V. Hirschi, F. Maltoni, O. Mattelaer, H.-S. Shao, T. Stelzer, P. Torrielli, and M. Zaro, *The automated computation of tree-level and next-to-leading order differential cross sections, and their matching to parton shower simulations*, JHEP **07** (2014), p. 079, [[arXiv:1405.0301](https://arxiv.org/abs/1405.0301)] (cited on pages 40, 52, 64, 75).
- [23] Torbjorn Sjostrand, Stephen Mrenna, and Peter Z. Skands, *PYTHIA 6.4 Physics and Manual*, JHEP **05** (2006), p. 026, [[arXiv:hep-ph/0603175](https://arxiv.org/abs/hep-ph/0603175)] (cited on pages 40, 52, 64, 75).
- [24] · S. Agostinelli et al., *GEANT4: A Simulation Toolkit*, Nucl. Instrum. Meth. **A506**. (2003), pp. 250–303  
· John Allison et al., *Geant4 developments and applications*, IEEE Trans. Nucl. Sci. **53** (2006), p. 270  
· J. Allison et al., *Recent developments in GEANT4*, Nucl. Instrum. Meth. **A835** (2016), pp. 186–225.
- [25] J. de Favereau, C. Delaere, P. Demin, A. Giammancio, V. Lemaître, A. Mertens, and M. Selvaggi, *DELPHES 3, A modular framework for fast simulation of a generic collider experiment*, JHEP **02** (2014), p. 057, [[arXiv:1307.6346](https://arxiv.org/abs/1307.6346)] (cited on pages 40, 52, 64, 75).
- [26] Joel Heinrich, 2002, URL: <https://www-cdf.fnal.gov/physics/statistics/recommendations/hypothesistesting.html> (cited on p. 41).

- [27] Kyle Cranmer, “Practical Statistics for the LHC”, *Proceedings, 2011 European School of High-Energy Physics (ESHEP 2011): Cheile Gradistei, Romania, September 7-20, 2011*, 2015, pp. 267–308, [[arXiv:1503.07622](https://arxiv.org/abs/1503.07622)] (cited on p. 41).
- [28] T. Hastie, R. Tibshirani, and J. Friedman, *The Elements of Statistical Learning: Data Mining, Inference, and Prediction*, Springer Series in Statistics, Springer New York, 2013 (cited on p. 45).
- [29] *LEP Higgs Working Group Home Page*, URL: <http://lephiggs.web.cern.ch/LEPHIGGS/www/Welcome.html> (cited on pages 47, 51).
- [30] Georges Aad et al., *Search for neutral Higgs bosons of the minimal supersymmetric standard model in  $pp$  collisions at  $\sqrt{s} = 8$  TeV with the ATLAS detector*, JHEP **11**. (2014), p. 056, [[arXiv:1409.6064](https://arxiv.org/abs/1409.6064)] (cited on pages 47, 51).
- [31] Vardan Khachatryan et al., *Search for neutral MSSM Higgs bosons decaying to a pair of tau leptons in  $pp$  collisions*, JHEP **10**. (2014), p. 160, [[arXiv:1408.3316](https://arxiv.org/abs/1408.3316)] (cited on pages 47, 51).
- [32] The ATLAS collaboration, *Search for charged Higgs bosons in the  $\tau+jets$  final state with  $pp$  collision data recorded at  $\sqrt{s} = 8$  TeV with the ATLAS experiment*, ATLAS-CONF-2013-090, 2013 (cited on pages 47, 50).
- [33] The CMS Collaboration, *Search for charged Higgs bosons with the  $H^+ \rightarrow \tau\nu$  decay channel in the fully hadronic final state at  $\sqrt{s} = 8$  TeV*, CMS-PAS-HIG-14-020, 2014 (cited on pages 47, 50, 58, 59).
- [34] Georges Aad et al., *Search for a light charged Higgs boson in the decay channel  $H^+ \rightarrow c\bar{s}$  in  $t\bar{t}$  events using  $pp$  collisions at  $\sqrt{s} = 7$  TeV with the ATLAS detector*, Eur. Phys. J. **C73**. (2013), p. 2465, [[arXiv:1302.3694](https://arxiv.org/abs/1302.3694)] (cited on pages 47, 50).
- [35] The CMS Collaboration, *Search for  $H^+$  to  $c\bar{s}$  decay*, CMS-PAS-HIG-13-035, 2014 (cited on pages 47, 50).
- [36] Vardan Khachatryan et al., *Search for a Higgs boson in the mass range from 145 to 1000 GeV decaying to a pair of W or Z bosons*, JHEP **10**. (2015), p. 144, [[arXiv:1504.00936](https://arxiv.org/abs/1504.00936)] (cited on p. 47).
- [37] David Curtin et al., *Exotic decays of the 125 GeV Higgs boson*, Phys. Rev. **D90**. (2014), p. 075004, [[arXiv:1312.4992](https://arxiv.org/abs/1312.4992)] (cited on pages 47, 60).
- [38] Eric Brownson, Nathaniel Craig, Ulrich Heintz, Gena Kukartsev, Meenakshi Narain, Neeti Parashar, and John Stupak, *Heavy Higgs Scalars at Future Hadron Colliders (A Snowmass Whitepaper)* (2013), [[arXiv:1308.6334](https://arxiv.org/abs/1308.6334)] (cited on pages 47, 60, 62, 64).

- [39] Baradhwaj Coleppa, Felix Kling, and Shufang Su, *Exotic Decays Of A Heavy Neutral Higgs Through HZ/AZ Channel*, JHEP **09** (2014), p. 161, [[arXiv:1404.1922](#)] (cited on pages [47](#), [60](#), [62–64](#), [66](#)).
- [40] Baradhwaj Coleppa, Felix Kling, and Shufang Su, *Charged Higgs search via AW $\pm$ /HW $\pm$  channel*, JHEP **12** (2014), p. 148, [[arXiv:1408.4119](#)] (cited on pages [47](#), [51](#), [54](#), [55](#), [60](#), [62](#)).
- [41] Tong Li and Shufang Su, *Exotic Higgs Decay via Charged Higgs*, JHEP **11**. (2015), p. 068, [[arXiv:1504.04381](#)] (cited on pages [47](#), [60](#), [62](#), [63](#)).
- [42] G. C. Dorsch, S. J. Huber, K. Mimasu, and J. M. No, *Echoes of the Electroweak Phase Transition: Discovering a second Higgs doublet through  $A_0 \rightarrow ZH_0$* , Phys. Rev. Lett. **113**. (2014), p. 211802, [[arXiv:1405.5537](#)] (cited on pages [47](#), [60](#), [62](#)).
- [43] Ning Chen, Chun Du, Yaquan Fang, and Lan-Chun Lü, *LHC Searches for The Heavy Higgs Boson via Two b Jets plus Diphoton*, Phys. Rev. **D89**. (2014), p. 115006, [[arXiv:1312.7212](#)] (cited on pages [47](#), [60](#)).
- [44] Ning Chen, Jinmian Li, Yandong Liu, and Zuowei Liu, *LHC searches for the CP-odd Higgs by the jet substructure analysis*, Phys. Rev. **D91**. (2015), p. 075002, [[arXiv:1410.4447](#)] (cited on pages [47](#), [60](#)).
- [45] Rikard Enberg, William Klemm, Stefano Moretti, Shoaib Munir, and Glenn Wouda, *Charged Higgs boson in the W $\pm$  Higgs channel at the Large Hadron Collider*, Nucl. Phys. **B893** (2015), pp. 420–442, [[arXiv:1412.5814](#)] (cited on pages [47](#), [60](#)).
- [46] Georges Aad et al., *Search for a CP-odd Higgs boson decaying to Zh in pp collisions at  $\sqrt{s} = 8$  TeV with the ATLAS detector*, Phys. Lett. **B744**. (2015), pp. 163–183, [[arXiv:1502.04478](#)] (cited on pages [47](#), [60](#)).
- [47] The CMS Collaboration, *Search for a pseudoscalar boson A decaying into a Z and an h boson in the llbb final state*, CMS-PAS-HIG-14-011, 2014 (cited on pages [47](#), [60](#)).
- [48] The CMS Collaboration, *Search for extended Higgs sectors in the H to hh and A to Zh channels in  $\sqrt{s} = 8$  TeV pp collisions with multileptons and photons final states*, CMS-PAS-HIG-13-025, 2013 (cited on pages [47](#), [60](#)).
- [49] Farvah Mahmoudi and Oscar Stal, *Flavor constraints on the two-Higgs-doublet model with general Yukawa couplings*, Phys. Rev. **D81** (2010), p. 035016, [[arXiv:0907.1791](#)] (cited on pages [48](#), [51](#)).
- [50] Baradhwaj Coleppa, Felix Kling, and Shufang Su, *Constraining Type II 2HDM in Light of LHC Higgs Searches*, JHEP **01** (2014), p. 161, [[arXiv:1305.0002](#)] (cited on pages [48](#), [49](#), [51](#), [56](#), [57](#)).

- [51] C. D. Froggatt, R. G. Moorhouse, and I. G. Knowles, *Leading radiative corrections in two scalar doublet models*, Phys. Rev. **D45**. (1992), pp. 2471–2481 (cited on p. 48).
- [52] C. D. Froggatt, R. G. Moorhouse, and I. G. Knowles, *Two scalar doublet models with softly broken symmetries*, Nucl. Phys. **B386**. (1992), pp. 63–114 (cited on p. 48).
- [53] Alex Pomarol and Roberto Vega, *Constraints on CP violation in the Higgs sector from the  $\rho$  parameter*, Nucl. Phys. **B413**. (1994), pp. 3–15, [[arXiv:hep-ph/9305272](#)] (cited on p. 48).
- [54] Abdul Wahab El Kaffas, Per Osland, and Odd Magne Ogreid, *Constraining the Two-Higgs-Doublet-Model parameter space*, Phys. Rev. **D76** (2007), p. 095001, [[arXiv:0706.2997](#)] (cited on p. 48).
- [55] Howard E. Haber and Deva O’Neil, *Basis-independent methods for the two-Higgs-doublet model III: The CP-conserving limit, custodial symmetry, and the oblique parameters S, T, U*, Phys. Rev. **D83**. (2011), p. 055017, [[arXiv:1011.6188](#)] (cited on p. 48).
- [56] Tao Han, Tong Li, Shufang Su, and Lian-Tao Wang, *Non-Decoupling MSSM Higgs Sector and Light Superpartners*, JHEP **11** (2013), p. 053, [[arXiv:1306.3229](#)] (cited on pages 48, 51).
- [57] David Eriksson, Johan Rathsman, and Oscar Stal, *2HDMC: Two-Higgs-Doublet Model Calculator Physics and Manual*, Comput. Phys. Commun. **181** (2010), pp. 189–205, [[arXiv:0902.0851](#)] (cited on p. 48).
- [58] John F. Gunion, Howard E. Haber, Gordon L. Kane, and Sally Dawson, *The Higgs Hunter’s Guide*, Front. Phys. **80**. (2000), pp. 1–404 (cited on p. 49).
- [59] J. R. Andersen et al., *Handbook of LHC Higgs Cross Sections: 3. Higgs Properties*, CERN-2013-004, FERMILAB-CONF-13-667-T, 2013, [[arXiv:1307.1347](#)] (cited on p. 50).
- [60] Neil D. Christensen, Tao Han, Zhen Liu, and Shufang Su, *Low-Mass Higgs Bosons in the NMSSM and Their LHC Implications*, JHEP **08**. (2013), p. 019, [[arXiv:1303.2113](#)] (cited on p. 50).
- [61] Manuel Drees, Monoranjan Guchait, and D. P. Roy, *Signature of charged to neutral Higgs boson decay at the LHC in SUSY models*, Phys. Lett. **B471**. (1999), pp. 39–44, [[arXiv:hep-ph/9909266](#)] (cited on p. 50).
- [62] C. Patrignani et al., *Review of Particle Physics*, Chin. Phys. **C40**. (2016), p. 100001 (cited on pages 51, 72).
- [63] Renato Guedes, Stefano Moretti, and Rui Santos, *Charged Higgs bosons in single top production at the LHC*, JHEP **10**. (2012), p. 119, [[arXiv:1207.4071](#)] (cited on p. 51).

- [64] Majid Hashemi, *Single Top Events as a Source of Light Charged Higgs in the Fully Hadronic Final State at LHC*, JHEP **05** (2013), p. 112, [[arXiv:1305.2096](#)] (cited on p. 51).
- [65] Majid Hashemi, *Observability of Light Charged Higgs Decay to Muon in Top Quark Pair Events at LHC*, Eur. Phys. J. **C72** (2012), p. 1994, [[arXiv:1109.5356](#)] (cited on p. 51).
- [66] Debottam Das, Lukas Mitzka, and Werner Porod, *Discovery of Charged Higgs through  $\gamma\gamma$  final states* (2014), [[arXiv:1408.1704](#)] (cited on p. 51).
- [67] Nikolaos Kidonakis, “Differential and total cross sections for top pair and single top production”, *Proceedings, 20th International Workshop on Deep-Inelastic Scattering and Related Subjects (DIS 2012): Bonn, Germany, March 26-30, 2012*, pp. 831–834, [[arXiv:1205.3453](#)] (cited on pages 51, 54).
- [68] Jacob Anderson et al., “Snowmass Energy Frontier Simulations”, *Proceedings, Community Summer Study 2013: Snowmass on the Mississippi (CSS2013): Minneapolis, MN, USA, July 29-August 6, 2013*, FERMILAB-TM-2566-CMS-E-PPD, 2013, [[arXiv:1309.1057](#)] (cited on pages 52, 54).
- [69] Lorenzo Moneta, Kevin Belasco, Kyle S. Cranmer, S. Kreiss, Alfio Lazzaro, Danilo Piparo, Gregory Schott, Wouter Verkerke, and Matthias Wolf, *The RooStats Project*, PoS **ACAT2010** (2010), p. 057, [[arXiv:1009.1003](#)] (cited on p. 52).
- [70] *theta-introduction to theta-auto*, URL: [http://www-ekp.physik.uni-karlsruhe.de/~ott/theta/testing/html/theta\\_auto\\_\\_intro.html](http://www-ekp.physik.uni-karlsruhe.de/~ott/theta/testing/html/theta_auto__intro.html) (cited on p. 52).
- [71] Georges Aad et al., *Measurement of the t-channel single top-quark production cross section in  $pp$  collisions at  $\sqrt{s} = 7$  TeV with the ATLAS detector*, Phys. Lett. **B717**. (2012), pp. 330–350, [[arXiv:1205.3130](#)] (cited on p. 53).
- [72] Felix Kling, Tilman Plehn, and Michihisa Takeuchi, *Tagging single Tops*, Phys. Rev. **D86** (2012), p. 094029, [[arXiv:1207.4787](#)] (cited on p. 53).
- [73] R. Contino et al., *Physics at a 100 TeV  $pp$  collider: Higgs and EW symmetry breaking studies*, CERN-TH-2016-113, 2016, [[arXiv:1606.09408](#)] (cited on pages 61–63).
- [74] John F. Gunion and Howard E. Haber, *The CP conserving two Higgs doublet model: The Approach to the decoupling limit*, Phys. Rev. **D67**. (2003), p. 075019, [[arXiv:hep-ph/0207010](#)] (cited on p. 61).
- [75] Georges Aad et al., *Constraints on new phenomena via Higgs boson couplings and invisible decays with the ATLAS detector*, JHEP **11**. (2015), p. 206, [[arXiv:1509.00672](#)] (cited on p. 62).

- [76] G. C. Dorsch, S. J. Huber, K. Mimasu, and J. M. No, *Hierarchical versus degenerate 2HDM: The LHC run 1 legacy at the onset of run 2*, Phys. Rev. **D93**. (2016), p. 115033, [[arXiv:1601.04545](https://arxiv.org/abs/1601.04545)] (cited on p. 62).
- [77] Baradhwaj Coleppa, Felix Kling, and Shufang Su, *Exotic Higgs Decay via AZ/HZ Channel: a Snowmass Whitepaper* (2013), [[arXiv:1308.6201](https://arxiv.org/abs/1308.6201)] (cited on p. 62).
- [78] Ushoshi Maitra, Biswarup Mukhopadhyaya, S. Nandi, Santosh Kumar Rai, and Ambresh Shivaji, *Searching for an elusive charged Higgs boson at the Large Hadron Collider*, Phys. Rev. **D89**. (2014), p. 055024, [[arXiv:1401.1775](https://arxiv.org/abs/1401.1775)] (cited on pages 62, 64).
- [79] L. Basso, A. Lipniacka, F. Mahmoudi, S. Moretti, P. Osland, G. M. Pruna, and M. Purmohammadi, *Probing the charged Higgs boson at the LHC in the CP-violating type-II 2HDM*, JHEP **11**. (2012), p. 011, [[arXiv:1205.6569](https://arxiv.org/abs/1205.6569)] (cited on pages 62, 63).
- [80] Radovan Dermisek, Jonathan P. Hall, Enrico Lunghi, and Seodong Shin, *A New Avenue to Charged Higgs Discovery in Multi-Higgs Models*, JHEP **04** (2014), p. 140, [[arXiv:1311.7208](https://arxiv.org/abs/1311.7208)] (cited on pages 62, 63).
- [81] B. Mohn, N. Gollub, and K. A. Assamagan, *The ATLAS discovery potential for a heavy Charged Higgs boson in a large mass splitting MSSM scenario*, ATL-PHYS-PUB-2005-017, ATL-COM-PHYS-2005-021, CERN-ATL-COM-PHYS-2005-021, 2005 (cited on p. 62).
- [82] K. A. Assamagan, *Signature of the charged Higgs decay  $H^\pm \rightarrow W^\pm h^0$  with the ATLAS detector*, Acta Phys. Polon. **B31** (2000), pp. 881–893 (cited on p. 62).
- [83] Nima Arkani-Hamed, Tao Han, Michelangelo Mangano, and Lian-Tao Wang, *Physics opportunities of a 100 TeV proton–proton collider*, Phys. Rept. **652** (2016), pp. 1–49, [[arXiv:1511.06495](https://arxiv.org/abs/1511.06495)] (cited on p. 62).
- [84] *FCC-hh Homepage*, URL: <http://tlep.web.cern.ch/content/fcc-hh> (cited on p. 62).
- [85] *The CEPC Homepage*, URL: <http://cepc.ihep.ac.cn/index.html> (cited on p. 62).
- [86] T. Golling et al., *Physics at a 100 TeV pp collider: beyond the Standard Model phenomena*, CERN-TH-2016-111, FERMILAB-PUB-16-296-T, 2016, [[arXiv:1606.00947](https://arxiv.org/abs/1606.00947)] (cited on p. 62).
- [87] M. Mangano et al., *Physics at a 100 TeV pp collider: Standard Model processes*, CERN-TH-2016-112, FERMILAB-FN-1021-T, 2016, [[arXiv:1607.01831](https://arxiv.org/abs/1607.01831)] (cited on pages 62, 75).
- [88] Matthew Low and Lian-Tao Wang, *Neutralino dark matter at 14 TeV and 100 TeV*, JHEP **08** (2014), p. 161, [[arXiv:1404.0682](https://arxiv.org/abs/1404.0682)] (cited on pages 69, 72).

- [89] Gianfranco Bertone, Dan Hooper, and Joseph Silk, *Particle dark matter: Evidence, candidates and constraints*, Phys. Rept. **405** (2005), pp. 279–390, [[arXiv:hep-ph/0404175](#)] (cited on p. [70](#)).
- [90] James D. Wells, “Implications of supersymmetry breaking with a little hierarchy between gauginos and scalars”, *11th International Conference on Supersymmetry and the Unification of Fundamental Interactions (SUSY 2003) Tucson, Arizona, June 5-10, 2003*, 2003, [[arXiv:hep-ph/0306127](#)] (cited on p. [70](#)).
- [91] N. Arkani-Hamed, S. Dimopoulos, G. F. Giudice, and A. Romanino, *Aspects of split supersymmetry*, Nucl. Phys. **B709** (2005), pp. 3–46, [[arXiv:hep-ph/0409232](#)] (cited on p. [70](#)).
- [92] G. F. Giudice and A. Romanino, *Split supersymmetry*, Nucl. Phys. **B699** (2004), [Erratum: Nucl. Phys.B706,487(2005)], pp. 65–89, [[arXiv:hep-ph/0406088](#)] (cited on p. [70](#)).
- [93] Kim Griest and David Seckel, *Three exceptions in the calculation of relic abundances*, Phys. Rev. **D43**. (1991), pp. 3191–3203 (cited on p. [70](#)).
- [94] Christopher Rogan, *Kinematical variables towards new dynamics at the LHC*, 2010, [[arXiv:1006.2727](#)] (cited on p. [70](#)).
- [95] Bobby S. Acharya, Krzysztof Bożek, Chakrit Pongkitivanichkul, and Kazuki Sakurai, *Prospects for observing charginos and neutralinos at a 100 TeV proton-proton collider*, JHEP **02** (2015), p. 181, [[arXiv:1410.1532](#)] (cited on pages [71](#), [72](#), [76](#)).
- [96] Stefania Gori, Sunghoon Jung, Lian-Tao Wang, and James D. Wells, *Prospects for Electroweakino Discovery at a 100 TeV Hadron Collider*, JHEP **12** (2014), p. 108, [[arXiv:1410.6287](#)] (cited on pages [71](#), [72](#), [76](#), [81](#)).
- [97] Tao Han, Sanjay Padhi, and Shufang Su, *Electroweakinos in the Light of the Higgs Boson*, Phys. Rev. **D88**. (2013), p. 115010, [[arXiv:1309.5966](#)] (cited on p. [71](#)).
- [98] Joshua Ellis, *TikZ-Feynman: Feynman diagrams with TikZ*, Comput. Phys. Commun. **210** (2017), pp. 103–123, [[arXiv:1601.05437](#)] (cited on p. [72](#)).
- [99] Tilman Plehn, *Lectures on LHC Physics*, Lect. Notes Phys. **844** (2012), pp. 1–193, [[arXiv:0910.4182](#)] (cited on p. [72](#)).
- [100] Asher Berlin, Tongyan Lin, Matthew Low, and Lian-Tao Wang, *Neutralinos in Vector Boson Fusion at High Energy Colliders*, Phys. Rev. **D91**. (2015), p. 115002, [[arXiv:1502.05044](#)] (cited on p. [72](#)).
- [101] Marco Cirelli, Filippo Sala, and Marco Taoso, *Wino-like Minimal Dark Matter and future colliders*, JHEP **10** (2014), [Erratum: JHEP01,041(2015)], p. 033, [[arXiv:1407.7058](#)] (cited on p. [72](#)).

- [102] A. Djouadi, M. M. Muhlleitner, and M. Spira, *Decays of supersymmetric particles: The Program SUSY-HIT (SUspect-SdecaY-Hdecay-InTerface)*, Acta Phys. Polon. **B38**. (2007), pp. 635–644, [[arXiv:hep-ph/0609292](#)] (cited on p. 74).
- [103] The ATLAS collaboration, *Search for supersymmetry with two and three leptons and missing transverse momentum in the final state at  $\sqrt{s} = 13$  TeV with the ATLAS detector*, ATLAS-CONF-2016-096, 2016 (cited on p. 74).
- [104] Vardan Khachatryan et al., *Searches for electroweak production of charginos, neutralinos, and sleptons decaying to leptons and W, Z, and Higgs bosons in pp collisions at 8 TeV*, Eur. Phys. J. **C74**. (2014), p. 3036, [[arXiv:1405.7570](#)] (cited on p. 74).
- [105] Serguei Chatrchyan et al., *Search for electroweak production of charginos and neutralinos using leptonic final states in pp collisions at  $\sqrt{s} = 7$  TeV*, JHEP **11**. (2012), p. 147, [[arXiv:1209.6620](#)] (cited on p. 74).
- [106] The ATLAS collaboration, *Search for electroweak production of supersymmetric particles in final states with tau leptons in  $\sqrt{s} = 13$  TeV pp collisions with the ATLAS detector*, ATLAS-CONF-2016-093, 2016 (cited on p. 74).
- [107] Vardan Khachatryan et al., *Search for electroweak production of charginos in final states with two  $\tau$  leptons in pp collisions at  $\sqrt{s} = 8$  TeV*, JHEP **04** (2017), p. 018, [[arXiv:1610.04870](#)] (cited on p. 74).
- [108] Serguei Chatrchyan et al., *Search for new physics in events with photons, jets, and missing transverse energy in pp collisions at  $\sqrt{s} = 7$  TeV*, JHEP **03**. (2013), p. 111, [[arXiv:1211.4784](#)] (cited on p. 74).
- [109] Vardan Khachatryan et al., *Search for supersymmetry in events with a photon, a lepton, and missing transverse momentum in pp collisions at  $\sqrt{s} = 8$  TeV*, Phys. Lett. **B757**. (2016), pp. 6–31, [[arXiv:1508.01218](#)] (cited on p. 74).
- [110] Georges Aad et al., *Search for photonic signatures of gauge-mediated supersymmetry in 8 TeV pp collisions with the ATLAS detector*, Phys. Rev. **D92**. (2015), p. 072001, [[arXiv:1507.05493](#)] (cited on p. 74).
- [111] Vardan Khachatryan et al., *Search for supersymmetry with photons in pp collisions at  $\sqrt{s}=8$  TeV*, Phys. Rev. **D92**. (2015), p. 072006, [[arXiv:1507.02898](#)] (cited on p. 74).
- [112] Vardan Khachatryan et al., *Search for supersymmetry in electroweak production with photons and large missing transverse energy in pp collisions at  $\sqrt{s} = 8$  TeV*, Phys. Lett. **B759**. (2016), pp. 479–500, [[arXiv:1602.08772](#)] (cited on p. 74).

- [113] Georges Aad et al., *Search for direct production of charginos, neutralinos and sleptons in final states with two leptons and missing transverse momentum in  $pp$  collisions at  $\sqrt{s} = 8$  TeV with the ATLAS detector*, JHEP **05**. (2014), p. 071, [[arXiv:1403.5294](#)] (cited on p. 75).
- [114] Vardan Khachatryan et al., *Search for supersymmetry in the vector-boson fusion topology in proton-proton collisions at  $\sqrt{s} = 8$  TeV*, JHEP **11**. (2015), p. 189, [[arXiv:1508.07628](#)] (cited on p. 75).
- [115] Vardan Khachatryan et al., *Searches for electroweak neutralino and chargino production in channels with Higgs, Z, and W bosons in  $pp$  collisions at 8 TeV*, Phys. Rev. **D90**. (2014), p. 092007, [[arXiv:1409.3168](#)] (cited on p. 75).
- [116] W. Beenakker, M. Klasen, M. Kramer, T. Plehn, M. Spira, and P. M. Zerwas, *The Production of charginos / neutralinos and sleptons at hadron colliders*, Phys. Rev. Lett. **83** (1999), [Erratum: Phys. Rev. Lett. **100**, 029901 (2008)], pp. 3780–3783, [[arXiv:hep-ph/9906298](#)] (cited on p. 75).
- [117] Joseph Bramante, Patrick J. Fox, Adam Martin, Bryan Ostdiek, Tilman Plehn, Torben Schell, and Michihisa Takeuchi, *Relic Neutralino Surface at a 100 TeV Collider*, Phys. Rev. **D91** (2015), p. 054015, [[arXiv:1412.4789](#)] (cited on p. 76).
- [118] · E. Conte, B. Fuks, and G. Serret, *MadAnalysis 5, A User-Friendly Framework for Collider Phenomenology*, Comput. Phys. Commun. **184** (2013), pp. 222–256, [[arXiv:1206.1599](#)]
  - E. Conte, B. Dumont, B. Fuks, and C. Wymant, *Designing and recasting LHC analyses with MadAnalysis 5*, Eur. Phys. J. **C74**. (2014), p. 3103, [[arXiv:1405.3982](#)]
  - B. Dumont, B. Fuks, S. Kraml, S. Bein, G. Chalons, E. Conte, S. Kulkarni, D. Sengupta, and C. Wymant, *Toward a public analysis database for LHC new physics searches using MADANALYSIS 5*, Eur. Phys. J. **C75**. (2015), p. 56, [[arXiv:1407.3278](#)].
- [119] Fabian Pedregosa and G Varoquaux, *Scikit-learn: Machine learning in Python*, Journal of Machine Learning Research **12** (2011), pp. 2825–2830, [[arXiv:1201.0490v2](#)] (cited on p. 78).
- [120] Jessie Shelton, “Jet Substructure”, *Proceedings, Theoretical Advanced Study Institute in Elementary Particle Physics: Searching for New Physics at Small and Large Scales (TASI 2012): Boulder, Colorado, June 4-29, 2012*, 2013, pp. 303–340, [[arXiv:1302.0260](#)] (cited on p. 81).
- [121] A. Schwartzman, M. Kagan, L. Mackey, B. Nachman, and L. De Oliveira, *Image Processing, Computer Vision, and Deep Learning: new approaches to the analysis and physics interpretation of LHC events*, J. Phys. Conf. Ser. **762**. (2016), p. 012035 (cited on p. 81).

## **Colophon**

This thesis was designed using L<sup>A</sup>T<sub>E</sub>X and the `memoir` package. The inspiration for the layout comes from the works of Edward Tufte and the `classicthesis` package by André Miede. Minion Pro is used for serif text, Scala Sans for sans-serif text, and Menlo for monospaced text.